Dissertation

for the degree of
'doctor rerum naturalium' (Dr. rer. nat.)
in 'Climate Physics'

submitted to the Faculty of Science
of the University of Potsdam

South Asian summer monsoon variability: A modelling study with the atmospheric regional climate model HIRHAM5

---

presented by
Franziska Stefanie Hanf

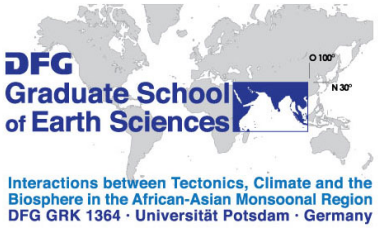

Supervisor: Prof. Dr. Klaus Dethloff

Submission: 28/09/2015

Published online at the
Institutional Repository of the University of Potsdam:
URN urn:nbn:de:kobv:517-opus4- 89331
http://nbn-resolving.de/urn:nbn:de:kobv:517-opus4- 89331

Abstract

It is well-established that periods of abundant rainfall (active spells) and scanty rainfall (break spells) are inherent to the South Asian summer monsoon. However, the understanding of the origin of long-lasting dryness (extended breaks), which affects the agriculture and therefore the food production and the economic development, the electricity generation from renewables as well as essential needs of the population across South Asia, is still in its early stages.

This study investigates moist dynamical processes that initiate and maintain breaks during the South Asian summer monsoon using the atmospheric regional climate model HIRHAM5 at a horizontal resolution of 25 km forced by the ECMWF ERA Interim reanalysis for the period 1979-2012. By calculating moisture and moist static energy budgets the various competing mechanisms leading to extended breaks are quantitatively estimated. Model evaluation against state-of-the-art observational products reveals a land-sea contrast with underestimated (overestimated) precipitation over India (the warm adjacent seas) in association with a warm temperature bias over the plains of northern India that has been found in several other regional climate models. Motivated by these deficiencies of HIRHAM5 a tuning of uncertain or non-observable parameters related to convective cloud and land surface processes is conducted in order to adapt the parameterisations to the regional climate conditions of South Asia and the increased horizontal grid resolution.

The budget diagnostics highlight that dry advection is the dominant moist dynamical process in initiating extended break conditions over South Asia. Anomalous westerlies at the northward flank of an anomalous anticyclonic circulation over India, forced as a Rossby wave response to negative rainfall anomalies over the near-equatorial Indian Ocean, transport air of low MSE from the deserts of western Asia towards central India and trigger the dryness over that region. Once initiated, the breaks are maintained due to many competing mechanisms: (i) the anomalous easterlies at the southern flank of this anticyclonic anomaly weaken the low-level cross-equatorial jet and thus the moisture transport into the monsoon region, (ii) differential radiative heating over the continental and the oceanic tropical convergence zone induces a local Hadley circulation with anomalous rising over the equatorial Indian Ocean and descent over central India, and (iii) a cyclonic response to positive rainfall anomalies over the near-equatorial Indian Ocean amplifies the anomalous easterlies over India and hence contributes to the low-level divergence over central India.

A sensitivity experiment that mimics a scenario of higher atmospheric aerosol concentrations over South Asia addresses a current issue of large uncertainty: the role aerosols play in suppressing monsoon rainfall and hence in triggering breaks. To study the indirect aerosol effects the cloud droplet number concentration was increased to imitate the aerosol's function as cloud condensation nuclei. The sensitivity experiment with altered microphysical cloud properties shows a reduction in the summer monsoon precipitation together with a weakening of the South Asian summer monsoon. Several physical mechanisms are proposed to be responsible for the suppressed monsoon rainfall: (i) according to the first indirect radiative forcing the increase in the number of cloud droplets causes an increase in the cloud reflectivity of solar radiation, leading to a climate cooling over India which

in turn reduces the evaporative fluxes and hence the hydrological cycle, (ii) a stabilisation of the troposphere induced by a differential cooling between the surface and the upper troposphere over central India inhibits the growth of deep convective rain clouds, (iii) an increase of the amount of low and mid-level clouds together with a decrease in high-level cloud amount amplify the surface cooling and hence the atmospheric stability, and (iv) dynamical changes of the monsoon manifested as a anomalous anticyclonic circulation over India reduce the moisture transport into the monsoon region. Owing to the fact that only the stratiform cloud scheme takes into account the cloud microphysics in HIRHAM5, the study suggests that the changes in the total precipitation, which are dominated by changes in the convective precipitation, mainly result from the indirect radiative forcing. Suppression of rainfall due to the direct microphysical effect is found to be negligible over India. Break statistics of the polluted cloud scenario indicate an increase in the occurrence of short breaks (3 days), while the frequency of extended breaks ($\geq$ 7 days) is clearly not affected. This disproves the hypothesis that more and smaller cloud droplets, caused by a high load of atmospheric aerosols trigger long drought conditions over central India.

However, due to the complexity of aerosol-cloud interactions, it is concluded that further sensitivity experiments including the direct aerosol forcing and impacts of aerosols on ice particles are necessary to better understand the aerosol effects on clouds and precipitation over South Asia. The results of the budget study imply the requirement of realistic three-dimensional moisture distributions over South Asia for a closer understanding of the monsoon break mechanisms. To generate reliable regional model simulations of the South Asian summer monsoon, further model tuning is needed to adapt the physical parameterisations concerning moisture processes to the tropical climate.

Contents

1 Introduction

The lives of more than 1/6 th of the world population is directly affected by the caprices of the South Asian summer monsoon rainfall (Singh et al., 2014; Turner and Annamalai, 2012). India receives around 78 % of the annual precipitation during the June-September months, the summer monsoon season of South Asia (Ding and Sikka, 2006). This main rainy season is therefore of paramount importance for the agricultural sector. As the food production accounts for most of the export of India, the development of the country's economy is crucially linked to the monsoon rainfall (Gadgil and Kumar, 2006). But, the monsoon circulation is not consistent throughout the entire summer season (Dunning et al., 2015). Episodes of heavy rainfall (active periods) and low rainfall (break periods) are inherent to the intraseasonal variability of the South Asian summer monsoon (SASM). However, prolonged breaks or long-lasting dryness can result in droughts (Prasanna and Annamalai, 2012) and hence trigger crop failures and in turn famines. Furthermore, India's electricity generation from renewable sources (wind and hydro-power), which is increasingly important in order to satisfy the rapidly rising demand for energy, is highly reliant on the prevailing meteorology (Dunning et al., 2015).

The major drought years 2002 and 2009 for the Indian summer monsoon during the last decades, which are results of the occurrence of multiple extended breaks (Bhat, 2006; Bhawar and Rahul, 2013; Manoj et al., 2012), emphasise exemplary that the understanding of the monsoon system and its intraseasonal variation is of greatest importance. Forecasting these periods of prolonged relative dryness well in advance would have an immense value and could be used to optimise agricultural practices and water resource management, and to prevent disasters associated with monsoon rainfall variability. While, during recent decades rapid developments in climate modelling and much progress in numerics and computer power have improved the ability of models in reproducing climate conditions, the numerical simulation and prediction of intraseasonal variability in the tropics by general circulation models is generally poor (Webster, 2006). This is probably caused by the coarse resolutions of global climate models (GCMs), which can not correctly capture regional forcings such as the steep and high orography of the Himalayas and the Western Ghats (Lucas-Picher et al., 2011). However, regional climate models (RCMs) provide an approach that allows more

detailed process studies and simulation of regional and even local conditions (Rummukainen, 2010). Many studies have been carried out to capture SASM features (e.g. Dobler and Ahrens, 2010; Lucas-Picher et al., 2011; Mukhopadhyay et al., 2010; Polanski et al., 2010; Rockel and Geyer, 2008; Saeed et al., 2009; Saeed et al., 2012; Sinha et al., 2012; Srinivas et al., 2012). But there are as yet no analyses of RCM applications that focus on the understanding of break monsoon spells over India in terms of the intraseasonal variability of the SASM. The potential of increased resolution of RCMs should be used to address actual research questions: What are the moist dynamical mechanisms that control prolonged monsoon breaks? Which circulation patterns lead to a transport of dry air over central India and thus initiate break periods? Act high loadings of atmospheric aerosols in association with dry air intrusions from desert regions as a trigger to enhance drought like conditions? These outstanding issues motivate the focus of the present study.

1.1 The mean South Asian summer monsoon

In the most basic sense, the picture of the SASM is something like a thermally driven giant land-sea breeze (Trenberth et al., 2006). The seasonal migration of solar heating that warms the continental regions of South and Southeast Asia faster than the adjoining seas due to the different heat capacities during boreal spring, induces a large-scale meridional surface temperature gradient. As a result, a surface heat low over northern India develops in late spring. The arising north-south gradient in pressure is then compensated by a cross-equatorial surface flow and a return flow above. However, the dynamics and thermodynamics of the SASM are more complex than explainable by this simple sea breeze mechanism (Turner and Annamalai, 2012). A second hypothesis interprets the monsoon as a manifestation of the seasonal migration of the Intertropical Convergence Zone (ITCZ) (Gadgil, 2003). The north-northwestward migration of the zone of low-level convergence, ascending motion and hence deep convection from the equatorial region during boreal spring and its interaction with the heat low lead to a positive feedback and a low pressure belt extending over northern India (Fig. 1.1). The deeper monsoon trough strengthens the low-level cross-equatorial jet (CEJ), the accompanied upper level Tibetan anticyclone and the easterly jet (EJ) as the upper tropospheric return flow. The CEJ, which approaches South Asia from across the Arabian Sea as a low-level westerly jet owing to the Earth's rotation, supplies the monsoon region with moisture (Gadgil, 2003; Turner and Annamalai, 2012).

During the summer monsoon, there are several prominent high rainfall belts in the South Asian monsoon region (Fig. 1.1). In association with orographic effects heavy rainfall occurs along the foothills of the sub-Himalayan ranges, the Western Ghats mountains on the west coast of India and near the Arakan Range and the western slopes of the Bilauktaung Range

in Myanmar. Furthermore, meso-scale convective systems embedded into the monsoon trough (Turner and Annamalai, 2012) cause high precipitation amounts over the northeast of the Indian peninsula. Over the warm water of the equatorial Indian Ocean, another rainfall zone is manifested in the seasonal precipitation patterns (Gadgil, 2003).

1.2 Monsoon variability on intraseasonal timescales

While the word 'monsoon', which is derived from the Arabic expression for season (Gadgil, 2003), refers to the seasonal nature of the monsoon system, the variation of the monsoon around its characteristic seasonal evolution (as described above) is of paramount interest (Trenberth et al., 2006). Changes at the lower boundary of the atmosphere, including the El Niño/Southern Oscillation (ENSO), the Indian Ocean temperatures expressed by the Indian Ocean dipole (IOD) index, the Himalayan glacier cover and the Eurasian snow cover induce interannual variations in rainfall which are relatively low with the standard deviation

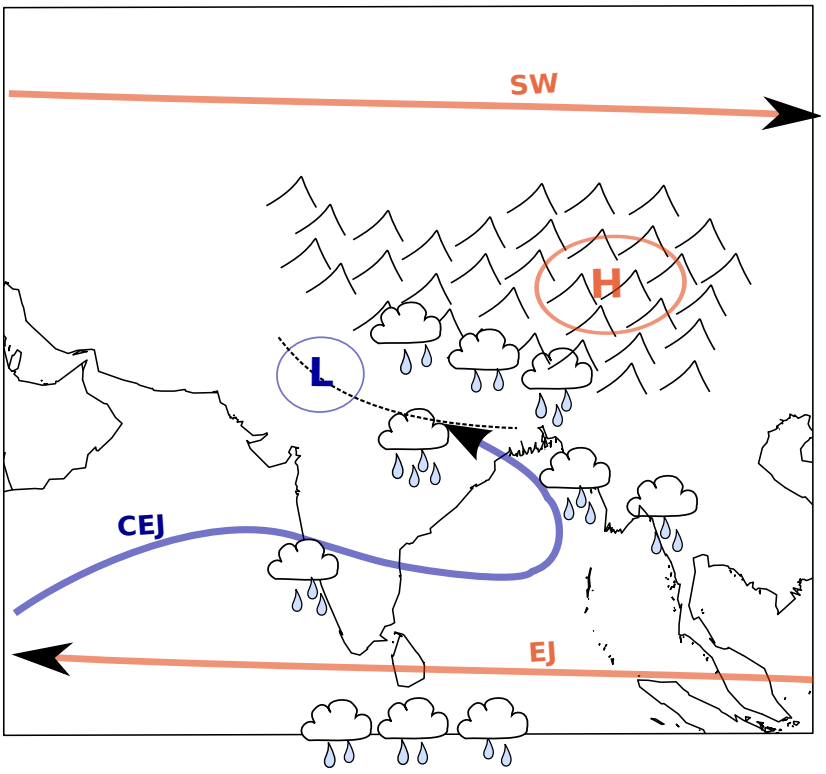

Figure 1.1: Schematic of the prevailing circulation pattern during the South Asian summer monsoon (CEJ = cross-equatorial jet; EJ = easterly jet; SW = subtropical westerlies). Intense rainfall occurs over the north-east of India, along the Western Ghats mountains, south of the foothills of the Himalayas, and near the Arakan Range and the western slopes of the Bilauktaung Range in Myanmar. Another belt of heavy rainfall is located over the warm waters of the equatorial Indian Ocean. The dotted line in the diagram represents the mean axis of the monsoon trough. 'H' and 'L' refer to the high over the Tibetan Plateau and the monsoon low, respectively. Blue (orange) marks low-level (upper level) circulation features.

being only 10 % of the summer rainfall total (Krishnamurti et al., 2010; Turner and Annamalai, 2012). In the case of the South Asian monsoon, especially the variability on intraseasonal timescales plays an important role, because irregular spatial and temporal distributions of rain may have negative effects on agriculture, hydroelectric production, industrial development and basic human needs, even if the seasonal mean monsoon rainfall is normal (Annamalai and Slingo, 2001; Turner and Annamalai, 2012). During the monsoon season, there are two favourable locations of deep convection over the Indian longitudes, one over the Indian subcontinent and another over the equatorial Indian Ocean. This bimodal structure of convection shows the manifestation of the ITCZ in two branches, the continental tropical convergence zone (TCZ) and the oceanic TCZ (Annamalai and Slingo, 2001; Sikka and Gadgil, 1980; Turner and Annamalai, 2012). The northward transition of convection from the oceanic to the continental regime induces large variability in the precipitation patterns over India, resulting in active (heavy rainfall) and break periods (low rainfall). In addition to these northward propagating events, which are identified as the 40-day (30-60 day) intraseasonal mode, another 10-20 day variability (15-day mode) exists associated with westward propagation over the monsoon domain (Annamalai and Slingo, 2001). Both of the intraseasonal modes contribute to the active/break cycle over India, but Annamalai and Slingo (2001) found that the 40-day mode plays the dominant role and explains 2/3 of the total subseasonal variability.

Having recognized the devastating impacts of monsoon breaks, many studies focused on the understanding of the dynamical and moist processes that control the transition from an active to a break phase of the SASM by using observations, reanalysis and satellite data as well as global climate model simulations (e.g. Annamalai, 2010; Annamalai and Slingo, 2001; Annamalai and Sperber, 2005; Bhat, 2006; Gadgil and Asha, 1992; Krishnamurthy and Shukla, 2007; Krishnamurti et al., 2010; Krishnan et al., 2000; Prasanna and Annamalai, 2012; Raghavan, 1973; Raman and Rao, 1981; Ramaswamy, 1962; Rao et al., 2004). Based on satellite products, Rao et al. (2004) showed that an abrupt atmospheric drying occurs in 200–600 hPa over the continental TCZ three days before the commencement of a break (30 % reduction in relative humidity). Likewise, Bhat (2006) and Krishnamurti et al. (2010) presented the advection of dry air from over the deserts of western Asia toward central India as an important feature for dry spells by analysing back-trajectories during the major droughts of the years 2002 and 2009. Bhat (2006) emphasised that a persistent and strong atmospheric inversion near 800 hPa prevents the vertical growth of deep convection. Krishnamurti et al. (2010) pointed out that the formation of a blocking high around the Arabian peninsula imports descending very dry air over central India at the 700 hPa level during breaks. By performing moisture and moist static energy (MSE) budgets on the ERA Interim reanalysis data, Prasanna and Annamalai (2012) showed that dry advection is the principal

moist process to initiate extended breaks. They suggested the origin of this dry advection as a superposition of multiple mechanisms: The northern Arabian Sea anticyclonic circulation anomaly forced by equatorial Indian Ocean negative rainfall anomalies advects air of low MSE content from north to central India, and the tropical western Pacific rainfall increase induces cyclonic circulation anomalies to its northwest, which transport air of low MSE from the north to the plains of India, Bay of Bengal and South China Sea. Furthermore, Prasanna and Annamalai (2012) noted that cloud-radiation interactions play a major role in maintaining extended breaks. The observational and satellite based studies of Kiran et al. (2009), Manoj et al. (2012) and Bhawar and Rahul (2013) raised the question, whether high concentrations of atmospheric aerosols over central India in consequence of desert air intrusions from western Asia initiate long breaks.

1.3 Impact of aerosols on monsoon climate

It is a fact, that aerosols affect the climate system through many physical mechanisms (Lohmann and Feichter, 2005). Aerosols absorb and scatter solar radiation and absorb, scatter and emit longwave radiation. These pathways of interaction are referred to as the direct aerosol effects. The increase in reflection of solar radiation to space by aerosols together with the absorption of sunlight within the atmosphere lead to a reduction in the solar radiation absorbed by the Earth surface and hence to a cooling of the surface (direct radiative forcing) (Ramanathan et al., 2001). Additionally, absorption of solar radiation by the atmosphere can heat the air and in turn provoke evaporation of cloud droplets (semi-direct effect) (Lohmann and Feichter, 2005). Aerosols also influence the climate through their important role as cloud condensation nuclei, called the indirect aerosol effects (Ramanathan et al., 2001). In this way, changes in aerosol particle concentration produce changes in the size distribution of cloud droplets and therefore alter condensation and evaporation rates, latent heat release and collision coalescence efficiency, which in turn affect the precipitation efficiency (direct microphysical effect). Furthermore, the more and smaller cloud droplets have an influence on the cloud reflectivity (first indirect radiative forcing) and the cloud lifetime (second indirect radiative forcing) (Koren et al., 2008; Ramanathan et al., 2001). This demonstrates that aerosols can induce additional radiative forcing through the indirect effects by modifying the microphysical properties of clouds.

In the past few decades, emissions of aerosols over South Asia increased due to rapid urbanisation and population growth (Bollasina et al., 2013), resulting in large atmospheric concentrations of aerosols which become visible as a thick aerosol layer, the well-known Indo-Asian haze (Ramanathan et al., 2001) also referred to as atmospheric brown clouds (Ramanathan et al., 2005). While many studies have been carried out to understand

how increased amounts of atmospheric aerosols affect the Indian monsoon climate and regional precipitation patterns, most of them focused on the direct effects in association with absorbing aerosols (e.g. Bollasina et al., 2013; Lau and Kim, 2006; Lau et al., 2006; Menon et al., 2002; Nigam and Bollasina, 2010; Ramanathan et al., 2005). There are only a few studies related to the complex aerosol-cloud interactions over the South Asian monsoon region (e.g. Bhawar and Rahul, 2013; Liu et al., 2011; Manoj et al., 2012). By performing numerical experiments with a GCM, Liu et al. (2011) found both the direct microphysical effect and the radiative effect, that enhance atmospheric stability associated with the aerosol direct and first indirect radiative forcings to significantly reduce the summer precipitation over East Asia. Furthermore, they attributed also the changes in the East Asian summer monsoon circulation induced by the aerosols radiative forcing to the effect of decreased monsoon precipitation. Liu et al. (2011) argued that their findings should also be applicable in other monsoon regions such as South Asia. Manoj et al. (2012) and Bhawar and Rahul (2013) examined the impacts of the indirect aerosol effects on the deficiency of rainfall during the 2009 SASM drought based on satellite products. Both studies found suppressed deep convective cloud growth in association with high aerosol loading and highlighted the crucial role of aerosols in promoting dry spells. However, Manoj et al. (2012) emphasised that the first indirect radiative forcing cannot be a stand-alone process completely responsible for droughts, and rather the moisture availability governed by the large-scale dynamics is one among the most decisive components for cloud development and hence precipitation formation.

1.4 Aims of the study

An improved understanding of the mechanisms that control the evolution of monsoon breaks over India is a demanding task of the present study. Although, numerous studies based on observations, reanalysis data and global model simulations have also addressed this goal, the use of RCMs, which could benefit the understanding of the monsoon intraseasonal variability by its resolution advantage is only in the infancy stage. The present study meets this need by using the atmospheric RCM HIRHAM5, which allows a more detailed investigation of climate processes. Furthermore, this is the first research that applies moisture and moist static energy budget studies on the output of a RCM during the evolution of breaks of the SASM.

The following strategy is adopted. First, this work quantitatively examines moist dynamical processes over India during the initiation and established stage of breaks by estimating moisture and moist static energy budgets following the same procedure as Prasanna and

Annamalai (2012). The focus is on the role of the dry air advection from the deserts of western Asia towards central India as a trigger for monsoon breaks, as suggested by the studies of Bhat (2006), Krishnamurti et al. (2010) and Prasanna and Annamalai (2012). Second, the study investigates the influence of aerosols on the SASM climate by acting as cloud condensation nuclei. In particular, the study addresses one further issue of large uncertainty: the role aerosols may play in suppressing monsoon rainfall and hence in initiating breaks. An examination of statistics of break days will check if breaks occur more frequently in a scenario of increased atmospheric aerosol concentrations. An evaluation of the model's performance against state-of-the-art reanalysis, gauges-based observational products and satellite data sets, that reveals deficiencies in simulating the precipitation amounts over India motivated a sensitivity study on the impacts of parameter tuning on the monsoon climate.

The remainder of this work is structured as follows. A detailed description of the HIRHAM5 regional climate model in its standard configuration setup is given in chapter 2. The data sets used in this study are presented in chapter 3. Chapter 4 outlines the methodology for identifying break days and details of the budget equations. In chapter 5 the results of the control run for the 1979-2012 period are discussed. While section 5.1 validates the model's performance in simulating SASM characteristics on different timescales, section 5.2 focuses on the intraseasonal variability of the monsoon and demonstrates the anomalous monsoon structure associated with the identified break phases, discusses the results of the moisture and moist static energy budget analyses and the elucidated moist dynamical mechanisms that trigger and maintain breaks. A parameter tuning study in order to reduce the deficiencies of the control run precipitation is documented in chapter 6. Chapter 7 shows the impacts of aerosol indirect effects on the mean SASM and its intraseasonal variability in a scenario with increased atmospheric aerosols and proposes a mechanism for the simulated changes. Finally, chapter 8 presents a summary of the results and discusses their implications for the understanding of the SASM intraseasonal variability, highlights the main conclusions and areas requiring further attention.

2 Model description and setup

2.1 The regional atmospheric climate model HIRHAM5

HIRHAM5 (Christensen et al., 2007) is the version 5 of the atmospheric RCM HIRHAM, which has been developed in collaboration between the Danish Climate Centre at the Danish Meteorological Institute (DMI) and the Potsdam Research Unit of the Alfred Wegener Institute Helmholtz Centre for Polar and Marine Research (AWI). This most recent version combines the dynamical core of the regional weather forecast model HIRLAM (HIgh Resolution Limited Area Model) (Undén et al., 2002) version 7 and the physical parameterisations of the atmospheric general circulation model ECHAM5 (European Centre HAmburg Model version 5) (Roeckner et al., 2003). More precisely, HIRHAM5 bases on the coupling between the release 7.0 of the HIRLAM model and the release 5.4.00 of the ECHAM model. In the following these two codes will be referred to as HIRLAM7 and ECHAM5.

2.1.1 Dynamical Core

HIRHAM5 is a hydrostatic model and solves seven prognostic equations for the horizontal wind components u and v, temperature T, specific humidity q, cloud liquid water content q_{l}, cloud ice content q_{i} and surface pressure p_{sfc}. Furthermore, there are two diagnostic equations for the geopotential Φ and the vertical wind velocity ω. These equations can be derived from the principal equations of the atmospheric motions (Holton, 2004) with some assumptions like the hydrostatic approximation. The resulting basic equations of HIRHAM5, the primitive equations (see in Klaus (2014), equations 2.6 - 2.12), contain subgrid-scale terms, which have to be physically parameterised (see section 2.1.2).

2.1.1.1 Numerical discretisation

In this study, the integration domain of HIRHAM5 covers the whole South Asia including the Himalayas (Fig. 2.1) with 218 $\times$ 200 grid points at a horizontal resolution of 0.25° (about 25 km) arranged in a rotated coordinate system.
For the horizontal discretisation of the primitive equations a centred finite difference scheme

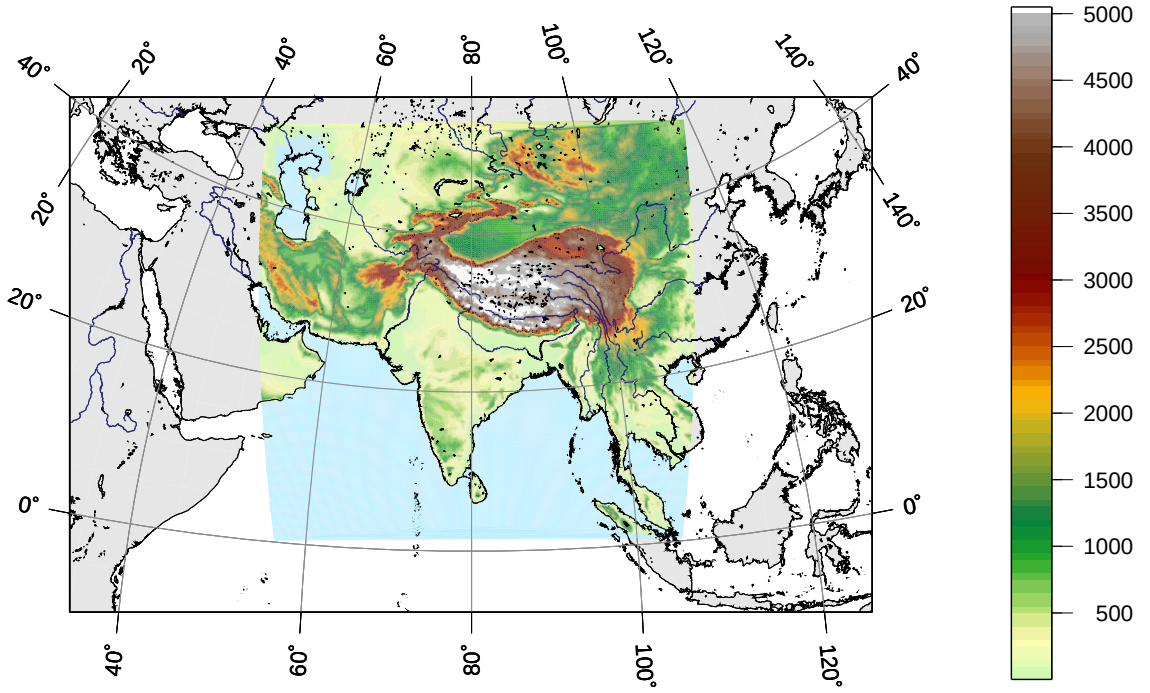

Figure 2.1: The South Asian model domain of HIRHAM5 and the model orography [m].

is applied, excluding the cloud liquid water content and cloud ice content. In order to improve advection characteristics compared to centred difference numerics (Sass et al., 2002), for these two prognostic variables an upstream advection scheme is used. Both schemes are implemented on an Arakawa C-grid. For the vertical discretisation in HIRHAM5 the atmosphere is divided into 40 non-equidistant levels with the model top at a pressure height of 10 hPa using a sigma-pressure hybrid coordinate.

The time discretisation of HIRHAM5 is of Eulerian type. However, the computations are split into an explicit part and a semi-implicit part. The semi-implicit correction allows to retain model stability for reasonably long time steps (Sass et al., 2002). For the numerical solution of the prognostic equations a semi-implicit leapfrog time scheme is used with a time step of $\Delta t = 120$ s. Consistent to the horizontal discretisation, the calculation of the tendencies of cloud liquid water content and cloud ice content is treated differently by using an explicit Euler forward method without any semi-implicit correction.

2.1.1.2 Horizontal diffusion

The application of finite difference approximations and physical parameterisations leads to accumulation of energy on the smallest scales in numerical weather prediction models (Gollvik, 1999) and climate models. To control this small-scale noise, a procedure called horizontal diffusion was introduced into the models. Furthermore, McDonald (1995) showed

model level k	1	2	3	4	5
$ampf$	16	16	8	4	2

Table 2.1: Amplification factor $ampf$ of the horizontal diffusion for the five uppermost model levels

that horizontal diffusion plays a substantial role in maintaining model stability.
HIRHAM5 takes into account the horizontal diffusion by an implementation of an implicit sixth-order diffusion scheme. As described by McDonald (1995), the horizontal diffusion equation of sixth-order, which has to be solved for each prognostic model variable ψ (except for p_{sfc}), can be formally written as

$$\frac{\partial \psi}{\partial t} = K_6 \, \nabla_{\mathrm{h}}^6 \psi \, , \tag{2.1}$$

where K_6 is the diffusion coefficient and ∇_{h} is the horizontal nabla operator. However, due to limitations in computing power a simplified sixth-order diffusion equation (Eq. (2.24) in Klaus (2014)) is solved in the model using a two-step split implicit approximation (see Klaus (2014), for details). In the standard version of HIRHAM5, K_6 is set to a value of $K_6 = 1.0 \times 10^{24}$ according to McDonald (1995). It has been found that the reflection of gravity waves at the upper model boundary have caused instabilities (Christensen et al., 1996). To avoid this unphysical effect a simple filtering has been implemented by an additional smoothing in the upper five model levels. Hence, K_6 varies for different model levels as follows

$$K_6(k) = K_6 \; ampf\,(k) \, , \tag{2.2}$$

where k is the vertical model level and $ampf$ represents the amplification factor of the horizontal diffusion. Tab. 2.1 lists the amplification factor for the five uppermost levels. While the diffusion is enhanced in the uppermost five levels, the lower levels ($k = 6, \ldots, 40$) use the standard K_6 with $ampf = 1$.

2.1.2 Physical Parameterisations

Physical processes have to be parameterised in the model equations, either because the respective process is an sub-grid scale process and can not be resolved explicitly by the model, or because a more accurate treatment would be too complex and exceeds the computer power recently available.
The sub-grid scale processes in HIRHAM5 include: cumulus convection and convective precipitation (section 2.1.2.1), stratiform clouds including cloud microphysics and stratiform precipitation (section 2.1.2.2), shortwave and longwave radiation processes (section 2.1.2.3),

surface albedo (section 2.1.2.4), land surface processes including soil hydrology (section 2.1.2.5), vertical diffusion, turbulent surface fluxes and gravity wave drag (not used in this model version). These model physics base on the comprehensive parameterisation package of ECHAM5 (Roeckner et al., 2003).

2.1.2.1 Cumulus convection

In HIRHAM5 cumulus convection is parameterised by the mass flux scheme of Tiedtke (1989) with modifications for penetrative convection according to Nordeng (1994). Cumulus clouds are assumed to be embedded in the large-scale environment by ensembles of clouds, which are defined by updraft and downdraft mass fluxes and by their thermal properties as dry static energy, moisture and cloud water content. Mass-flux schemes of varying complexity determine the mass-flux of the updrafts M_u, the entrainment of air into the updraft from surroundings E_u and detrainment of air out of the updraft D_u as functions of height (Mauritsen, 2012). The Tiedtke (1989) scheme describes the cloud ensemble by an one-dimensional bulk model, which is used separately for cumulus updrafts and cumulus downdrafts with bulk properties specified differently for the convection types penetrative convection, shallow convection and midlevel convection. The updrafts and downdrafts of the cloud ensemble are assumed to be in a steady state.
The bulk equations for the vertical distribution of mass, heat, moisture, cloud water and momentum for an ensemble of cumulus updrafts are as described in Roeckner et al. (2003)

$$\frac{\partial M_\mathrm{u}}{\partial z} = E_\mathrm{u} - D_\mathrm{u} \tag{2.3}$$

$$\frac{\partial}{\partial z}(M_\mathrm{u} s_\mathrm{u}) = E_\mathrm{u}\bar{s} - D_\mathrm{u} s_\mathrm{u} + L\bar{\rho}c_\mathrm{u} \tag{2.4}$$

$$\frac{\partial}{\partial z}(M_\mathrm{u} q_\mathrm{u}) = E_\mathrm{u}\bar{q} - D_\mathrm{u} q_\mathrm{u} - \bar{\rho}c_\mathrm{u} \tag{2.5}$$

$$\frac{\partial}{\partial z}(M_\mathrm{u} l_\mathrm{u}) = -D_\mathrm{u} l_\mathrm{u} + \bar{\rho}c_\mathrm{u} - \bar{\rho}P_\mathrm{u} \tag{2.6}$$

$$\frac{\partial}{\partial z}(M_\mathrm{u} u_\mathrm{u}) = E_\mathrm{u}\bar{u} - D_\mathrm{u} u_\mathrm{u} \tag{2.7}$$

$$\frac{\partial}{\partial z}(M_\mathrm{u} v_\mathrm{u}) = E_\mathrm{u}\bar{v} - D_\mathrm{u} v_\mathrm{u} \tag{2.8}$$

with $s = c_\mathrm{p}T + gz$ the dry static energy, ρ the air density, q the specific humidity, l the cloud water content (sum of cloud liquid water and cloud ice contents), L the latent heat of

condensation, c_{u} the net condensation in the updrafts, P_{u} the conversion of cloud water to precipitation, and u and v the horizontal wind vector components. The subscript u denotes updraft variables and the overbar represents large-scale variables. Cloud air is assumed to be saturated. In the following the subscript u will be omitted to facilitate easier reading.

The strength of convection depends firstly, on the cloud base mass flux and secondly, on the entrainment of air from the air surrounding the cloud into the cloud and the detrainment of air out of the cloud. The cloud base mass flux, which will be discussed later (see Eq. (2.19)), is determined separately for the various types of convection. The entrainment and detrainment processes are divided in turbulent and organised parts, respectively:

$$E = E^{\mathrm{t}} + E^{\mathrm{o}} \,, \qquad D = D^{\mathrm{t}} + D^{\mathrm{o}} \,. \tag{2.9}$$

Turbulent entrainment E^{t} and detrainment D^{t} are defined as the turbulent mass exchange of cloud air and environmental air through the cloud edges due to small-scale eddies and are parameterised as

$$E^{\mathrm{t}} = \varepsilon^{\mathrm{t}} \cdot M \,, \qquad D^{\mathrm{t}} = \delta^{\mathrm{t}} \cdot M \tag{2.10}$$

with ε^{t} (δ^{t}) being the fractional turbulent entrainment (detrainment) rate and M the vertical cloud ensemble mass flux. M is defined as

$$M = \sum_j \bar{\rho}\, a_j\, w_j \tag{2.11}$$

with the fractional cloud cover area of an individual member of the cloud ensemble a_j and the vertical velocity for an individual updraft w_j. In case of cumulus updrafts fixed values of turbulent entrainment (detrainment) rates are defined according to typical cloud sizes associated with the three convection types:

$$\varepsilon^{\mathrm{t}} = \delta^{\mathrm{t}} = \begin{cases} 1 \times 10^{-4}\,\mathrm{m}^{-1} & , \text{ for penetrative and mid-level convection} \\ 3 \times 10^{-4}\,\mathrm{m}^{-1} & , \text{ for shallow convection.} \end{cases} \tag{2.12}$$

Small entrainment (detrainment) rates are used for penetrative and mid-level convection, representing high reaching convective clouds with intense convection in the presence of synoptic-scale flow convergence. Large entrainment (detrainment) rates, leading to a weakening of the convective activity, are imposed to describe shallow convection associated with clouds of smaller size in the absence of large-scale flow convergence.

According to Nordeng (1994), organised entrainment is the organised inflow at the cloud base caused by large-scale convergence. Organised detrainment is assumed to be the

outflow at the cloud top when the buoyancy becomes negative. Both processes are related to the cloud activity itself. By analogy with Eq. (2.10), the organised entrainment E^{o} and detrainment D^{o} can be written as

$$E^{\mathrm{o}} = \varepsilon^{\mathrm{o}} \cdot M \,, \qquad D^{\mathrm{o}} = \delta^{\mathrm{o}} \cdot M \,, \tag{2.13}$$

whereas ε^{o} (δ^{o}) is defined as the fractional organised entrainment (detrainment) rate. The organised entrainment rate of a cloud ensemble is parameterised as

$$\varepsilon^{\mathrm{o}} = \frac{b}{2\,(w_{\mathrm{base}}^2 + \int_{\mathrm{base}(z=0)}^{z} b\,dz)} + \frac{1}{\bar{\rho}}\frac{\partial \bar{\rho}}{\partial z} \tag{2.14}$$

with the cloud ensemble buoyancy $b = \frac{g}{\bar{T}_{\mathrm{v}}}(T_{\mathrm{v}} - \bar{T}_{\mathrm{v}}) - g\,l$ and the constant vertical velocity at cloud base $w_{\mathrm{base}} = 1\,\mathrm{m\,s^{-1}}$. $T_{\mathrm{v}} = T\,(1 + (\frac{R_{\mathrm{v}}}{R_{\mathrm{d}}} - 1)q - q_{\mathrm{l}} - q_{\mathrm{i}})$ is the virtual temperature and g is the acceleration due to gravity. Based on the assumption that individual clouds do not change their fractional area before they start to detrain, the individual cloud cover change at the detrainment level z_{d} can be expressed as the total cloud cover change ($\frac{\partial a_{z_{\mathrm{d}}}}{\partial z} = \frac{\partial a}{\partial z}$). Consequently, the organised detrainment rate becomes

$$\delta^{\mathrm{o}} = -\frac{1}{a}\frac{\partial a}{\partial z}\,, \tag{2.15}$$

where a, the total cloud cover is approximated through an analytical function $a = a(z)$ in order to simulate the spectrum of individual clouds detraining at different levels z_{d}.

Cumulus downdrafts are assumed to originate from cloud air influenced by the injection of environmental air which has been cooled to its wet bulb temperature by evaporation of precipitation previously formed in the updrafts. The downdrafts are represented in the scheme as the quasi-reverse of updrafts so that a corresponding set of equations is used for the vertical distribution of the downdraft mass flux, dry static energy, moisture and momentum (cf. Eq. (2.3) - (2.8)). Due to the fact that the downdrafts are determined from the evaporating convective rain, there is no corresponding equation of downdraft cloud water content. According to Fritsch and Chapell (1980) and Foster (1958), the Level of Free Sinking (LFS) is defined as the highest model level where a mixture of equal parts of cloud air and saturated environmental air at wet bulb temperature would have negative buoyancy relative to the environmental air. The downward mass flux at the LFS $(M_{\mathrm{d}})_{\mathrm{LFS}}$ is imposed to be directly proportional to the upward mass flux at cloud base $(M_{\mathrm{u}})_{\mathrm{base}}$ as follows:

$$(M_{\mathrm{d}})_{\mathrm{LFS}} = -\,\gamma\,(M_{\mathrm{u}})_{\mathrm{base}} \tag{2.16}$$

with $\gamma = 0.3$ being a tunable parameter.

Entrainment and detrainment processes in cumulus downdrafts are highly uncertain due to the lack of relevant data (Tiedtke, 1989). Based on numerical experiments that reveal a rather insensitivity of the results to changes in the entrainment and detrainment rate parameterisation, Tiedtke (1989) argued to use a fixed value to describe the entrainment (detrainment) rate for cumulus downdrafts independent of the type of convection as follows:

$$\varepsilon = \delta = 2 \times 10^{-4}\,\mathrm{m}^{-1}\,. \tag{2.17}$$

The vertical integration of Eq. (2.3) - (2.8) requires the specification of the cloud base mass flux $(M_\mathrm{u})_\mathrm{base}$, which is determined differently for the various types of convection. A moisture convergence closure is used for shallow and mid-level convection. In case of shallow convection the moisture supply arises largely through surface evaporation, whereas for mid-level convection this is realised through the vertical advection associated with the large-scale ascent. For penetrative convection an adjustment-type closure was introduced by Nordeng (1994) linking the cloud base mass flux to convective instability instead of moisture convergence. This closure defines the convective activity in terms of the Convective Available Potential Energy ($CAPE$), that is estimated from parcel ascent associated with cloud water loading effects

$$CAPE = \int_\mathrm{base}^\mathrm{top} b\,dz = \int_\mathrm{base}^\mathrm{top} \Big(\frac{g}{\bar{T}_\mathrm{v}} \left(T_\mathrm{v} - \bar{T}_\mathrm{v}\right) - g\,l \Big)\,dz\,. \tag{2.18}$$

By assuming that convection acts to reduce $CAPE$ towards zero in a characteristic time τ, the cloud base mass flux can be written as

$$(M_\mathrm{u})_\mathrm{base} = \frac{CAPE}{\tau}\,. \tag{2.19}$$

Thus, the cloud base mass flux is inversely proportional to the tunable parameter τ that depends on the horizontal grid resolution of the model. In the convective cloud scheme the characteristic time scale is parameterised by

$$\tau\,[\mathrm{s}] = \min\left(3 \cdot 3600\,;\ \frac{2 \cdot 3600 \cdot 63}{nn}\right), \tag{2.20}$$

where nn is the spectral resolution of the ECHAM5 model. In the standard HIRHAM5 version nn is set to a value of $nn = 159$ (approximately 80 km $\times$ 80 km grid cells), resulting in $\tau \approx 47.5$ min. Nordeng (1994) argued that τ should be smaller (larger) with increasing (decreasing) horizontal resolution in order to keep the vertical mass flux at approximately the same order of magnitude as the resolved vertical velocity. In a sensitivity study (see chapter 6) τ is modified according to $nn = 319$ (approximately 40 km $\times$ 40 km grid cells).

Convective precipitation

Independent of the type of convection there is a common definition for the formation of convective precipitation. As in Roeckner et al. (1992), the mass continuity equations for precipitation (rain and snow) in convective clouds are given by

$$\text{rain:} \qquad P^{\mathrm{l}}_{\mathrm{conv}}(p) = \frac{1}{g} \int_{p=0}^{p} (\hat{P}^{\mathrm{l}}_{\mathrm{conv}} - e^{\mathrm{l}}_{\mathrm{d}} - e^{\mathrm{l}}_{\mathrm{P}} + m)\, dp \,, \tag{2.21}$$

$$\text{snow:} \qquad P^{\mathrm{i}}_{\mathrm{conv}}(p) = \frac{1}{g} \int_{p=0}^{p} (\hat{P}^{\mathrm{i}}_{\mathrm{conv}} - e^{\mathrm{i}}_{\mathrm{d}} - e^{\mathrm{i}}_{\mathrm{P}} - m)\, dp \,, \tag{2.22}$$

where $P^{\mathrm{l}}_{\mathrm{conv}}(p)$ and $P^{\mathrm{i}}_{\mathrm{conv}}(p)$ are the fluxes of rain water and snow at pressure level p, $\hat{P}^{\mathrm{l}}_{\mathrm{conv}}$ and $\hat{P}^{\mathrm{i}}_{\mathrm{conv}}$ are the conversion rates from cloud droplets and cloud ice into precipitation, $e^{\mathrm{l}}_{\mathrm{d}}$ and $e^{\mathrm{i}}_{\mathrm{d}}$ are the evaporation of cloud water and cloud ice (sublimation) that has been detrained into the environment and $e^{\mathrm{l}}_{\mathrm{P}}$ and $e^{\mathrm{i}}_{\mathrm{P}}$ are the evaporation of precipitation in the unsaturated subcloud layer and m is the melting of snow.
The conversion from cloud particles to rain (snow) is assumed to be proportional to the cloud water content l (= $q_{\mathrm{l}} + q_{\mathrm{i}}$) for all convection types as follows

$$\bar{\rho}\, \hat{P}^{\mathrm{l\,(i)}}_{\mathrm{conv}} = K(z)\, l\, M_{\mathrm{u}} \,. \tag{2.23}$$

$K(z)$ is an empirical function that depends on height z as

$$K(z) = \begin{cases} 0 \quad , & \text{if } z \le Z_{\mathrm{B}} + \Delta z \\ k_{\mathrm{conv}} \quad , & \text{if } z > Z_{\mathrm{B}} + \Delta z \,, \end{cases} \tag{2.24}$$

where Z_{B} is the height of the cloud base, Δz is defined to be 1500 m over sea and 3000 m over land and k_{conv} is a tunable parameter which depends on the model resolution. In the standard HIRHAM5 version, k_{conv} is set to a value of $k_{\mathrm{conv}} = 1 \times 10^{-4}\,\mathrm{m}^{-1}$. $K(z)$ is assumed to be zero near cloud base, to ensure that shallow cumulus clouds do not produce precipitation (see Tiedtke (1989) for details).

2.1.2.2 Stratiform clouds

The stratiform cloud scheme in HIRHAM5 consists of prognostic equations for the specific humidity q, cloud liquid water content q_{l} and cloud ice content q_{i}, bulk cloud microphysics formulated by Lohmann and Roeckner (1996) and a prognostic-statistical cloud cover scheme elaborated by Tompkins (2002). The previous diagnostic cloud cover scheme of Sundqvist et al. (1989) is still implemented and can be used alternatively. The stratiform cloud formation is linked to the cumulus convection by use of the convective cloud water detrainment $D_{\mathrm{u}} l_{\mathrm{u}}$ in

Eq. (2.6) as a source term in the stratiform cloud liquid water and cloud ice equations (see in Roeckner et al. (1992), equations 10.1 - 10.3 for details).

Since real clouds are often smaller than the model grid resolution, cloud microphysical processes depend crucially on the distribution of the three water phases within the grid cell. In the stratiform cloud scheme of HIRHAM5, the sub-grid scale cloud formation is realised by incorporating fractional cloud cover for each grid cell.

For the statistical cloud cover scheme (Tompkins, 2002) the fractional cloud cover C is given by

$$C = \int_{q_{\mathrm{sat}}}^{\infty} G(q_{\mathrm{t}})\, dq_{\mathrm{t}} \,, \tag{2.25}$$

where $G(q_{\mathrm{t}})$ is the Probability Density Function (PDF) of the total atmospheric water content $q_{\mathrm{t}} = q + q_{\mathrm{l}} + q_{\mathrm{i}}$ and q_{sat} is the saturation value. This assumes that the sub-grid scale cloud formation is caused only by fluctuations in total water content. The saturation value is temperature-dependent and changes temporally in a grid cell. For the PDF Tompkins (2002) chooses the beta distribution (see in Roeckner et al. (1992), chapters 10.2.1/10.2.2 for details).

For the diagnostic cloud cover scheme (Sundqvist et al., 1989) the fractional cloud cover is expressed as an empirical function of the relative humidity as follows:

$$C = 1 - \sqrt{1 - C_0} \qquad \text{with } C_0 = \frac{\bar{r} - r_0}{r_{\mathrm{sat}} - r_0} \tag{2.26}$$

where $\bar{r}$ is the grid-cell mean relative humidity ($r = q/q_{\mathrm{sat}}$), r_{sat} (= 1) the saturation value and r_0 represents a subgrid-scale condensation threshold. This implies that condensational growth of cloud droplets occurs only if the grid-cell mean relative humidity exceeds the critical value i.e., $\bar{r} > r_0$. Otherwise, an existing cloud is diluted by evaporation if $\bar{r} < r_0$. The condensation threshold should depend on the grid resolution and sub-grid scale variance of vertical wind velocity (Roeckner et al., 1992). In HIRHAM5 r_0 is defined as an exponential function of height with $r_{0,\mathrm{top}}$ = 0.7 and $r_{0,\mathrm{sfc}}$ = 0.9 being the upper and lower values of the condensation threshold.

Tompkins (2005) showed that Eq. (2.26) can be derived from Eq. (2.25) on the assumption of using an uniform distribution for the PDF. Therefore, the diagnostic cloud cover scheme is equivalent to a first order prognostic cloud cover scheme with fixed higher distribution moments.

Cloud microphysics

The cloud microphysical scheme in HIRHAM5 takes into account homogeneous and heterogeneous freezing and Brownian diffusion contact nucleation of cloud liquid water, formation

of cloud liquid water (cloud ice crystals) by condensation (deposition) of water vapour, evaporation (sublimation) of cloud droplets (cloud ice) and melting of cloud ice. Furthermore, the scheme includes precipitation formation by coalescence processes (autoconversion from cloud droplets to rain drops, self collision of cloud or rain droplets and growth of rain drops by accretion of cloud droplets), autoconversion from ice crystals to snow (aggregation), growth of snow crystals by accretion of supercooled cloud droplets and by accretion of cloud ice as well as evaporation of rain drops and sublimation of snow.

All cloud microphysical terms in the prognostic equations for the specific humidity, cloud liquid water content and cloud ice content (see in Roeckner et al. (2003), chapter 10.1 for details) are calculated for the cloud covered part of the grid cell (C). Any cloud liquid water or cloud ice that is transported into the clear-sky part of the grid cell ($1 - C$) (by advection, vertical diffusion, convective detrainment or sedimentation) is instantaneously removed by evaporation and/or sublimation. Thus, the microphysical terms depend directly on the fractional cloud cover C, which is determined by the chosen cloud cover scheme (Tompkins (2002) or Sundqvist et al. (1989)). Apart from convective detrainment, the most important cloud generation processes are condensation and deposition of water vapour in the presence of moisture convergence and/or cooling. Otherwise, moisture divergence and/or warming lead to cloud dissipation through evaporation or sublimation (Roeckner et al., 2003).
In cold clouds, at temperatures $T < -35\,^{\circ}\mathrm{C}$, existing supercooled cloud droplets freeze homogeneously to cloud ice within one time step. Further, depositional growth of ice crystals takes place and condensation is assumed to be zero.
In mixed-phase clouds ($-35\,^{\circ}\mathrm{C} \leq T < 0\,^{\circ}\mathrm{C}$), the Bergeron-Findeisen process has to be taken into account. Due to the fact, that the saturation water vapour pressure with respect to ice is smaller than with respect to liquid water, supercooled droplets can form by condensation only if the cloud ice concentration is relatively small (only a few ice nuclei), i.e. the cloud ice content is smaller than a threshold (Bergeron-Findeisen process). Otherwise, growth of ice crystals by deposition is favoured. In this temperature range, heterogeneous freezing of cloud liquid water and Brownian diffusion contact freezing resulting from random collisions of aerosol particles with supercooled cloud droplets take place. Both processes are dependent on the cloud droplet number concentration N_{l}. Heterogeneous freezing is indirectly related to N_{l}, while Brownian diffusion contact freezing is directly related to N_{l}. In the standard setup of HIRHAM5, the cloud droplet number concentration has a fixed value of

$$N_{\mathrm{l}} = \begin{cases} 220 \times 10^6\,\mathrm{m}^{-3}, & \text{over land} \\ 80 \times 10^6\,\mathrm{m}^{-3}, & \text{over sea} \end{cases} \tag{2.27}$$

within the atmospheric boundary layer. Above the boundary layer, N_{l} is assumed to decrease exponentially with height to $50 \times 10^6\,\mathrm{m}^{-3}$ in the upper troposphere over both land and sea.

Further, Brownian diffusion contact freezing is a function of the mean volume droplet radius R_{vl}, which is defined in terms of the cloud liquid water content q_{l} and the cloud droplet number concentration N_{l} according to

$$R_{\mathrm{vl}} = \sqrt[3]{\frac{3\,q_{\mathrm{l}}\,\rho}{4\,\pi\,N_{\mathrm{l}}\,\rho_{\mathrm{w}}}}\,, \tag{2.28}$$

where ρ is the air density and $\rho_{\mathrm{w}} = 1000\,\mathrm{kg\,m^{-3}}$ is the density of water.
In warm clouds, at temperatures $T \geq 0\,^{\circ}\mathrm{C}$, cloud droplet growth occurs only by condensation and deposition is assumed to be negligible in this case. In both, warm and mixed-phase clouds, the liquid water content of the cloud can be reduced by autoconversion from cloud droplets to rain drops, growth of rain drops by accretion of cloud droplets and the growth of snow crystals by accretion of supercooled cloud droplets. The autoconversion rate describes the temporal evolution of a droplet spectrum modified by collisions among droplets of different size and thus controls the cloud life time. The efficiency of this process is a function of N_{l} with smaller values for higher cloud droplet number concentrations.

Further, the cloud liquid water and cloud ice content within the cloud covered part of the grid cell are used to compute the shortwave and longwave cloud optical properties (see section 2.1.2.3). Thus the cloud radiative properties are related to the model physics via cloud dynamics (Rinke et al., 1997).

Stratiform precipitation

The total amount of stratiform precipitation at a certain pressure level can be calculated by integrating the relevant cloud microphysical processes from the top of the atmosphere ($p = 0$) to the pressure level of interest p. The equations for fluxes of rain and snow in stratiform clouds are given by

$$\text{rain:} \qquad P^{\mathrm{l}}_{\mathrm{strat}}(p) = \frac{1}{g}\int_{p=0}^{p} (Q_{\mathrm{aut}} + Q_{\mathrm{racl}} - Q_{\mathrm{evr}} + Q_{\mathrm{mls}})\,dp \tag{2.29}$$

$$\text{snow:} \qquad P^{\mathrm{i}}_{\mathrm{strat}}(p) = \frac{1}{g}\int_{p=0}^{p} (Q_{\mathrm{agg}} + Q_{\mathrm{sacl}} + Q_{\mathrm{saci}} - Q_{\mathrm{sbs}} - Q_{\mathrm{mls}})\,dp \tag{2.30}$$

with Q_{aut} the autoconversion rate from cloud droplets to rain drops, Q_{racl} the accretional growth of rain drops through cloud droplets, Q_{evr} the evaporation of rain, Q_{mls} the snow melt, Q_{agg} the autoconversion rate from cloud ice to snow (aggregation), Q_{sacl} the accretion rate of supercooled cloud droplets by snow, Q_{saci} the accretion rate of cloud ice by snow and Q_{sbs} the sublimation of snow (see in Roeckner et al. (2003), chapter 10.3 for details). At the surface ($p = p_{\mathrm{sfc}}$), the ice sedimentation flux $\bar{F}^{\mathrm{sed}}_{\mathrm{i}} = -\frac{1}{g}\int_{p=0}^{p_{\mathrm{sfc}}} Q_{\mathrm{sed}}\,dp$ is added to the equation of snow flux (2.30) with Q_{sed} being the sedimentation of cloud ice.

2.1.2.3 Radiation

The radiation code in HIRHAM5 uses different schemes for the parameterisation of the shortwave and longwave fluxes. The shortwave radiative transfer scheme bases on the Integrated Forecast System (IFS) model of the ECMWF formulated by Fouquart and Bonnel (1980) with 6 resolved spectral bands. The longwave radiative transfer parameterisation follows the Rapid Radiative Transfer Model (RRTM) a two-stream approximation, developed by Mlawer et al. (1997) with 16 spectral bands (see in Roeckner et al. (2003), chapters 11.3 and 11.4 for details). For computational efficiency reasons the full radiative transfer calculations are executed less frequently than the dynamics and other parameterisations (see section 2.1.1.1). The radiation time step Δt_{rad} is set to 2 hours.

The diabatic heating rate Q_{rad} in a grid cell is calculated from the difference of the total net flux F_{rad} at the lower and upper boundary of the cell, the amount of air M and the specific heat of moist air at constant pressure c_{p}. F_{rad} is the sum of the net radiative fluxes in the shortwave and longwave spectrum ($F_{\mathrm{rad}} = F_{\mathrm{SW}} + F_{\mathrm{LW}}$). Using the hydrostatic approximation ($\frac{\partial p}{\partial z} = -\rho\, g$) and the definition of density as mass per unit volume, the heating rate can be written as

$$Q_{\mathrm{rad}} = \frac{(F_{\mathrm{rad}}^{\mathrm{lower}} - F_{\mathrm{rad}}^{\mathrm{upper}})}{M\, c_{\mathrm{p}}} = -\frac{g}{c_{\mathrm{p}}} \frac{(F_{\mathrm{rad}}^{\mathrm{lower}} - F_{\mathrm{rad}}^{\mathrm{upper}})}{(p^{\mathrm{lower}} - p^{\mathrm{upper}})} \tag{2.31}$$

where p is the air pressure and g is the acceleration due to gravity. The calculation of the net radiative fluxes in the shortwave and longwave spectrum requires profiles of absorber and scatterer, i.e. active gases, aerosols, cloud liquid water and cloud ice. Furthermore, the fractional cloud cover must be known. Specific humidity, cloud liquid water and cloud ice content are prognostic variables, while the fractional cloud cover is a diagnostic variable (see section 2.1.2.2). These variables differ in space and time. However, in the model atmosphere the gases CO_2, N_2O, CO, CH_4 and O_2, and the chlorofluorocarbon species CFC11 and CFC12 are prescribed as uniformly mixed gases, whereas ozone (O_3) is given by a zonal averaged monthly climatology with values at 19 pressure level, interpolated to model levels. Aerosol distributions are prescribed following the time independent climatology of Tanre et al. (1984), which distinguishes spatial distributions of optical properties for sea, urban land, desert aerosols, and well-mixed tropospheric and stratospheric background aerosols. The Global Aerosol Data Set (GADS) of Koepke et al. (1997) is available on request and can be used instead of the climatology of Tanre et al. (1984). The aerosol climatology is only provided to the radiative transfer schemes and has no effect on the cloud microphysical processes in HIRHAM5.

Cloud optical properties

The parameterisation of cloud properties for the shortwave part of the spectrum bases on Mie calculations using idealised size distributions for both cloud droplets and spherical ice crystals (Rockel et al., 1991). The single scattering properties are expressed in terms of the effective radii of cloud droplets R_{el} and ice crystals R_{ei}, respectively, which in turn depend directly on the cloud liquid water content (q_{l}) or cloud ice content (q_{i}). Following the empirical relationship of Johnson (1993), the effective radius of cloud droplets can be obtained from the mean volume radius (R_{vl})

$$R_{\mathrm{vl}}^3 = \kappa R_{\mathrm{el}}^3 \,, \tag{2.32}$$

and by using equation (2.28) R_{el} can be written as

$$R_{\mathrm{el}} = \sqrt[3]{\frac{3\, q_{\mathrm{l}} \rho}{4\, \pi\, N_{\mathrm{l}} \rho_{\mathrm{w}} \kappa}} \,, \tag{2.33}$$

where ρ is the air density, ρ_{w} = 1000 kg m^{-3} is the density of water and N_{l} is the cloud droplet number concentration as described in section 2.1.2.2. κ is a parameter related to the shape of the size distribution. Based on field experiments, Johnson (1993) suggested a mean value of κ = 0.67 for continental and κ = 0.80 for maritime clouds. The effective radius of ice crystals is defined following Moss et al. (1996) as

$$R_{\mathrm{ei}} = a_5 \,(10^3 \rho\, q_{\mathrm{i}})^{b_5} \tag{2.34}$$

with the parameters a_5 = 83.8 and b_5 = 0.216 (Roeckner et al., 2003).

Depending on the effective radii, the cloud optical properties for the liquid and ice phase are parameterised as follows:

$$\text{mass extinction coefficient:} \qquad \tilde{\tau}_{\mathrm{l,i}} = a_0\, R_{\mathrm{el,ei}}^{a_1} \tag{2.35}$$

$$\text{single scattering albedo:} \qquad \tilde{\omega}_{\mathrm{l,i}} = \sum_{n=0}^{2} b_n \,(\log\,(R_{\mathrm{el,ei}}))^n \tag{2.36}$$

$$\text{asymmetry factor:} \qquad \tilde{\gamma}_{\mathrm{l,i}} = \sum_{n=0}^{4} c_n \,(\log\,(R_{\mathrm{el,ei}}))^n \tag{2.37}$$

The coefficients a_0, a_1, b_n and c_n depend on the spectral range and the phase of water (see in Roeckner et al. (2003), tables 11.2 - 11.5). The optical depth of a cloud layer is given as a function of the mass extinction coefficients of liquid water clouds ($\tilde{\tau}_{\mathrm{l}}$) and ice clouds ($\tilde{\tau}_{\mathrm{i}}$), respectively, and the in-cloud Liquid Water Path (LWP) or in-cloud Ice Water Path (IWP) in

the respective model level:

$$\text{optical depth (liquid phase):} \qquad \tilde{\delta}_{\mathrm{l}} = \tilde{\tau}_{\mathrm{l}}\ LWP \tag{2.38}$$

$$\text{optical depth (ice phase):} \qquad \tilde{\delta}_{\mathrm{i}} = \tilde{\tau}_{\mathrm{i}}\ IWP\ . \tag{2.39}$$

In the longwave part of the spectrum scattering is assumed to be negligible. Hence, the impact of clouds on the longwave radiation can be described only by the mass absorption coefficient. The mass absorption coefficient of liquid clouds K_{l} is defined in terms of the effective radius of cloud droplets R_{el} (see Eq. (2.33)) according to

$$\text{mass absorption coefficient (liquid phase):} \qquad K_{\mathrm{l}} = 1.66\,[d_0\ +\ d_1 \exp(-d_2\, R_{\mathrm{el}})] \tag{2.40}$$

with the coefficients d_0, d_1 and d_2 (see in Roeckner et al. (2003), table 11.7). For the mass absorption coefficient of ice crystals K_{i}, the parameterisation following Ebert and Curry (1992) is used

$$\text{mass absorption coefficient (ice phase):} \qquad K_{\mathrm{i}} = 1.66\left(a_{\mathrm{c}}\ +\ \frac{b_{\mathrm{c}}}{R_{\mathrm{ei}}}\right) \tag{2.41}$$

with the effective radius of ice crystals R_{ei} (see Eq. (2.34)) and the coefficients a_{c} and b_{c}, which depend on the spectral range (see in Roeckner et al. (2003), table 11.8). Analogous to Eq. (2.38) and (2.39), the optical depth of a cloud layer for the liquid (ice) phase is defined for the longwave part using K_{l} (K_{i}) and LWP (IWP).

2.1.2.4 Surface albedo

When shortwave radiation is incident on the earth surface, one proportion will be reflected and the remainder will be absorbed. The shortwave reflectivity, also known as albedo, describes the fraction of the incoming shortwave radiation which is reflected from the surface. The albedo depends on different factors like the type and the properties of the surface (Petty, 2006).

Over snow-free land surfaces, an annual mean background albedo α_{bg}, which has been derived from satellite data is used following Hagemann (2002). Over snow-covered land surfaces, the grid-cell mean albedo is parameterised as a weighted average of the forest-covered and the forest-free part of the grid cell as follows

$$\alpha_{\mathrm{sfc}} = f_{\mathrm{for}}\,\alpha_{\mathrm{for}} + (1 - f_{\mathrm{for}})\,\alpha_{\mathrm{grd}}\ , \tag{2.42}$$

where f_{for} is the fractional forest area, α_{for} is the total forest albedo and α_{grd} is the albedo of the ground. The total forest albedo is defined as

$$\alpha_{\mathrm{for}} = (SVF)\,\alpha_{\mathrm{grd}} + (1 - SVF)\,\alpha_{\mathrm{can}} \tag{2.43}$$

with the Sky View Factor (SVF), a parameter related to the Leaf Area Index (LAI) which describes the degree of the canopy closure. The albedo of the ground is calculated as

$$\alpha_{\mathrm{grd}} = f_{\mathrm{sn}}\,\alpha_{\mathrm{sn}} + (1 - f_{\mathrm{sn}})\,\alpha_{\mathrm{bg}}\ , \tag{2.44}$$

where f_{sn} is the fractional snow cover at the ground, approximated as a function of the snow depth and the slope of the terrain. α_{sn} is the snow albedo, which is assumed to be a linear function of the surface temperature (see in Roeckner et al. (2003), equation 6.43) for glacier-covered land and a polynomial approximation for glacier-free land according to Roesch (2000). The minimum and maximum values of snow albedos for different land surface types are assigned in HIRHAM5 as listed in Tab. 2.2.
The albedo of the canopy α_{can} is given by

$$\alpha_{\mathrm{can}} = f_{\mathrm{snc}}\,\alpha_{\mathrm{snc}} + (1 - f_{\mathrm{snc}})\,\alpha_{\mathrm{bg}}\ , \tag{2.45}$$

where f_{snc} is the fractional snow cover of the canopy, a factor defined as the ratio between the snow depth at the canopy and the interception capacity of the canopy. α_{snc} is the albedo of the snow-covered part of the canopy and set to a constant value of $\alpha_{\mathrm{snc}} = 0.2$. According to the Eq. (2.42) - (2.45), $\alpha_{\mathrm{sfc}} = \alpha_{\mathrm{bg}}$ for a snow-free grid cell.
Over ice-free water surfaces (lake/ocean), the surface albedo is prescribed with a constant value ($\alpha_{\mathrm{sea}} = 0.07$).

surface type	$\alpha_{\mathrm{sn,min}}$	$\alpha_{\mathrm{sn,max}}$
glacier-free land	0.5	0.8
glacier-covered land	0.6	0.8
canopy	0.2	0.2

Table 2.2: Snow albedos for different land surface types defined in HIRHAM5 according to Køltzow (1992).

2.1.2.5 Land surface processes

Soil hydrology

The parameterisation of the soil hydrology takes into account the following water reservoirs: rain and snow intercepted by the canopy, snow accumulated at the surface and soil water.

The interception of rain water and melted snow by vegetation is limited by a threshold for the interception reservoir capacity, which is a function of the LAI. The residual amount of rain water and melting snow, which can not be intercepted by the canopy contributes to the amount of soil infiltration, surface runoff and drainage processes. Accordingly, the budget equation for soil water h_{ws} (depth in meter) can be written as

$$\rho_{\mathrm{w}} \frac{\partial h_{\mathrm{ws}}}{\partial t} = (1 - c_{\mathrm{v}})\, R + E_{\mathrm{ws}} + M_{\mathrm{sn}} + M_{\mathrm{snc}} - R_{\mathrm{sfc}} - D \tag{2.46}$$

with ρ_{w} the density of water, c_{v} = 0.25 an interception parameter, R the incoming rain, $E_{\mathrm{ws}} < 0$ the evaporation of soil water, $E_{\mathrm{ws}} > 0$ the dew deposition, M_{sn} the snow melt at the surface, M_{snc} the excess snow melt in the canopy, R_{sfc} the surface runoff and D the drainage. The computation of runoff and drainage follows the scheme of Dümenil and Todini (1992), which accounts for the heterogeneous distribution of local field capacities within a grid cell. In this scheme, the fractional saturated area f_{ws} of a grid cell is represented as a function of the degree of the grid-mean relative soil water $h_{\mathrm{ws}}/h_{\mathrm{cws}}$ and a shape parameter $\tilde{b}$

$$f_{\mathrm{ws}} = 1 - \left(1 - \frac{h_{\mathrm{ws}}}{h_{\mathrm{cws}}}\right)^{\tilde{b}}, \tag{2.47}$$

where h_{cws} is the total field capacity of the grid cell. Hence, f_{ws} defines the fraction of a grid cell where runoff would occur for a certain rainfall or snow melt event, while (1 - f_{ws}) describes the fraction of the grid cell, where the rainfall would infiltrate (Roeckner et al., 1992, 2003). The shape parameter $\tilde{b}$ is parameterised as a function of the sub-grid scale height distribution, which is a measure of the steepness of the terrain according to

$$\tilde{b} = \max\left(\min\left(\frac{\sigma_{\mathrm{z}} - \sigma_0}{\sigma_{\mathrm{z}} + \sigma_{\mathrm{max}}}, 0.5\right), 0.01\right), \tag{2.48}$$

where σ_{z} is the standard deviation of height in the grid cell and σ_0 and σ_{max} are prescribed minimum and maximum values of σ_{z} depending on the horizontal model resolution. In the standard setup of HIRHAM5, σ_0 and σ_{max} are assigned to values of σ_0 = 100 m and $\sigma_{\mathrm{max}} = \frac{1000 \cdot 64}{ngl}$ m for T159 resolution (approximately 80 km × 80 km grid cells), respectively. The number of latitudes referring to the atmospheric grid is set to ngl = 160, resulting in σ_{max} = 400 m. According to Eq. (2.48), the shape parameter varies between $\tilde{b}$ = 0.01 for relatively flat terrain and $\tilde{b}$ = 0.5 for steep terrain ($\sigma_{\mathrm{z}} \rightarrow \sigma_{\mathrm{max}}$).

The surface runoff R_{sfc} is computed by integrating all rain, snow melt and dew deposition that accumulate in the saturated part of the grid cell (f_{ws}) over one time step. It can be expressed as

$$\frac{\Delta t}{\rho_{\mathrm{w}}} R_{\mathrm{sfc}} = Q - (h_{\mathrm{cws}} - h_{\mathrm{ws}}) + \left[\left(1 - \frac{h_{\mathrm{ws}}}{h_{\mathrm{cws}}}\right)^{\frac{1}{1+\tilde{b}}} - \frac{Q}{(1+\tilde{b})\, h_{\mathrm{cws}}}\right]^{1+\tilde{b}}, \tag{2.49}$$

where Q is the total water input. Equation (2.49) is valid for the case that the soil is not brought to saturation during one time step. Then, $Q > 0$ will always lead to $R_{\mathrm{sfc}} > 0$ due to the contribution from sub-grid scale areas, which become saturated. Overall, the surface runoff is an extremely efficient process in steep terrain ($\tilde{b} \to 0.5$), while most of the precipitation can infiltrate the soil if the terrain is relatively flat ($\tilde{b} \to 0.01$). In the case, when Q and h_{ws} are large enough to cause an oversaturation of the whole grid cell, the traditional bucket scheme is applied. Then, the surface runoff is given by the excess of water above the maximum value i.e. that the square bracket on the right-hand side of Eq. (2.49) vanishes.

Drainage D is parameterised to occur independently of the water input Q if the soil water is between 5% and 90% (slow drainage) or between 90% and 100% (fast drainage) of the field capacity:

$$D = 0 \qquad \text{for } h_{\mathrm{ws}} \leq 0.05\, h_{\mathrm{cws}} \text{ (no drainage)} \tag{2.50}$$

$$D = d_{\mathrm{min}} \left(\frac{h_{\mathrm{ws}}}{h_{\mathrm{cws}}} \right) \quad \text{for } 0.05\, h_{\mathrm{cws}} < h_{\mathrm{ws}} \leq 0.9\, h_{\mathrm{cws}} \text{ (slow drainage)} \tag{2.51}$$

$$D = d_{\mathrm{min}} \left(\frac{h_{\mathrm{ws}}}{h_{\mathrm{cws}}} \right) + (d_{\mathrm{max}} - d_{\mathrm{min}}) \left[\frac{h_{\mathrm{ws}} - 0.9\, h_{\mathrm{cws}}}{h_{\mathrm{cws}} - 0.9\, h_{\mathrm{cws}}} \right]^{d} \quad \text{for } h_{\mathrm{ws}} > 0.9\, h_{\mathrm{cws}} \text{ (fast drainage)} \tag{2.52}$$

with the constants $d_{\mathrm{min}} = 2.8 \times 10^{-7}\,\mathrm{kg\,m^{-2}\,s^{-1}}$ and $d_{\mathrm{max}} = 2.8 \times 10^{-5}\,\mathrm{kg\,m^{-2}\,s^{-1}}$ and the parameter $d = 1.5$ which determines the efficiency of the fast drainage.

2.1.3 Model initialisation and forcing

2.1.3.1 Initial and boundary conditions

Due to the fact that HIRHAM5 is a RCM, the model needs not only initial conditions but also boundary values evolving in time from an external driving data set (Giorgi et al., 2001). In this case the model is operated by ERA Interim (Dee et al., 2011), the latest global atmospheric reanalysis produced by the European Centre for Medium-Range Weather Forecasts (ECMWF). At the lateral boundaries the model is driven by the ECMWF reanalysis data, updated every six hours. At the lower boundary HIRHAM5 is forced by six-hourly interpolated sea surface temperatures (SSTs) based on daily ERA Interim reanalysis fields. Moreover, surface characteristics (like e.g. land-sea-fraction, vegetation and soil type, glacier mask and orography) are prescribed by a monthly mean climatology data set.

2.1.3.2 Relaxation and nudging

Lateral boundary forcing provides the RCM with large-scale atmospheric conditions along the sides of the regional domain (Marbaix et al., 2003; Rummukainen, 2010). However, variations in process descriptions and different horizontal, vertical and time resolutions between the driving field and the regional model can cause numerical instabilities (Rummukainen, 2010). One technique to prevent the boundary condition problem is the relaxation method developed by Davies (1976). This boundary relaxation scheme of Davies (1976) is implemented in HIRHAM5. The principle of this method is that the model solution is 'relaxed' to the large-scale values of the driving field in a buffer zone next to the lateral boundaries. In HIRHAM5 the buffer zone size is set to 10 grid points. At the outermost lateral boundary the model solution is overwritten by the large-scale value of the boundary field. With increasing distance to the edge of the model domain the relaxation component, continuously added to the model-generated field decreases according to a weighted function (for details see e.g. in Sass et al. (2002), section 2.4). Finally, the free RCM solution remains unchanged in the inner model domain. In the standard version of HIRHAM5, all prognostic model fields are relaxed with the exception of the specific humidity (q). For the latter, the inflow-outflow formulation is applied, technically motivated by Christensen et al. (1996).

The motivation behind a RCM is to provide fine-scale details over a region fed by large-scale data of sparse resolution. In addition to that role, the RCM solution of the large-scale circulation should remain similar to that prescribed (Alexandru et al., 2009). However, sensitivity studies performed with HIRHAM5 over the whole Arctic region using only the lateral boundary relaxation scheme and the inflow-outflow formulation for q (Klaus, 2014) showed discrepancies at the synoptic-scale in the inner model domain relative to the driving data set. A way to mitigate the large-scale differences between the driving and the regional model field, is the technique of nudging. The procedure of nudging involves the use of large-scale atmospheric conditions not only at the lateral boundaries or in a relaxation zone but also within the inner model domain (Alexandru et al., 2009; Rummukainen, 2010). In HIRHAM5 an 1 % nudging is applied using the dynamical relaxation technique (Davies and Turner, 1977) at all levels in the inner model domain. That means that at every timestep 1 % of the corresponding ERA Interim field value is continuously added to 99 % of the internal model-generated field value (for details see in Klaus (2014), section 2.3.3). This ensures that the HIRHAM5 large-scale circulation does not diverge from the driving data set.

3 Reanalysis and observational data

To evaluate the skill of HIRHAM5 in simulating the South Asian climate, different reference data sets are taken into account. A brief overview of the data used in the present study is given in Tab. 3.1. More details of the data sets are presented in the following sections.

3.1 ERA Interim reanalysis

The ERA Interim reanalysis is the recent global atmospheric reanalysis produced by the ECMWF (Dee et al., 2011). Briefly, the ERA Interim atmospheric model and reanalysis system uses cycle 31r2 of the ECMWF Integrated Forecast System. It is configured for the following spatial and temporal resolution: 60 levels in the vertical with the model top at a pressure height of 0.1 hPa using a hybrid sigma-pressure vertical coordinate, T255

Data set	**Type (product)**	**Horizontal resolution and domain**	**Vertical resolution**	**Time period**	**Time resolution**
ERA Interim	reanalysis (atmospheric, hydrologic products)	$0.75° \times 0.75°$ global	60 level	1979 - 2012	6-hourly
APHRODITE	gauges-based (precipitation, temperature)	$0.25° \times 0.25°$ (15°S - 55°N, 60°E - 155°E)	surface data set	1951(1961) - 2007	daily
TRMM	satellite (precipitation)	$0.25° \times 0.25°$ (50°S - 50°N, 0°E - 360°E)	surface data set	1998 - 2012	daily
IITM	gauges-based (precipitation)	mean over India	surface data set	1871 - 2012	monthly

Table 3.1: Summary of the different data sets used in the present study for validation and in case of ERA Interim also as initial and boundary conditions for the HIRHAM5 simulations.

spherical-harmonic representation for the basic dynamical fields, a reduced Gaussian grid with approximately 79 km spacing for surface and other grid-point fields and a 30 min timestep using a semi-Lagrangean semi-implicit time stepping scheme (Berrisford et al., 2009; Dee et al., 2011). ERA Interim covers the period from 1 January 1979 onwards. In this study, the time period 1979-2012 is used in analogy to the HIRHAM5 simulations. To compare the HIRHAM5 to the ERA Interim data, the latter were interpolated onto the horizontal (0.25°) and vertical resolution (40 model levels) of the HIRHAM5 (cp. section 2.1.1.1).
A benefit of reanalysis data is that they provide a temporally coherent and spatially complete record of the global atmospheric circulation. The use of a forecast model enables the extrapolation of locally observed parameters to unobserved parameters with physical consistency and to propagate the information forward in time (Dee et al., 2011). Hence, reanalysis can provide useful estimates where observations are hardly available, for example in mountain regions like the Himalayas or over the oceans. Nevertheless, Dee et al. (2011) emphasised that reanalysis products produced by using a data assimilation scheme in combination with a forecast model, can not regard as equivalent to observations and should consider in tandem with observation-only climate data sets.

3.2 APHRODITE

The Asian Precipitation - Highly Resolved Observational Data Integration Towards Evaluation (APHRODITE) of water resources project has been conducted by the Research Institute for Humanity and Nature (RIHN) and the Meteorological Research Institute of the Japan Meteorological Agency (MRI/JMA). The project constructs state-of-the-art daily gridded precipitation data sets in high horizontal resolution covering the whole of Asia (Yatagai et al., 2012). The precipitation data sets base on rain-gauge-observations obtained from a dense network of meteorological and hydrological stations throughout the region. In this study, the latest version V1101 of the daily precipitation product for monsoon Asia (15°S - 55°N, 60°E - 155°E) is used in a horizontal grid resolution of 0.25° covering the period 1951-2007 (Yatagai et al., 2012).
In addition to the precipitation products, the APHRODITE project created a $0.25° \times 0.25°$ gridded daily mean temperature data set covering the same domain for the period 1961-2007 by utilising a collection of observed temperature data (Yasutomi et al., 2011). The recent version V1204R1 of this product is used to validate the HIRHAM5-generated near surface temperatures. In this study, for both APHRODITE products the time period 1979-2007 is considered to coincide with the HIRHAM5 simulations.
More detailed information on the algorithm and performance of the APHRODITE products are made available on the website (http://www.chikyu.ac.jp/precip/index.html).

3.3 TRMM

The Tropical Rainfall Measuring Mission (TRMM), launched in November 1997 is a joint mission between the National Aeronautics and Space Administration (NASA) and the Japan Aerospace Exploration Agency (JAXA) in order to develop precipitation products for weather and climate research (TRMM, 2015).
For this study, the version 7 of the "TRMM and Other Satellite Precipitation Product" 3B42 is used (Huffman et al., 2007). The TRMM 3B42 (V7) product is available at (ftp://disc2.nascom.nasa.gov/data/TRMM/Gridded/Derived_Products/3b42_V7/Daily). This product bases on the TRMM Multi-Satellite Precipitation Analysis algorithm and combines high quality microwave estimates with infrared precipitation estimates and a rain gauge adjustment. More details of the algorithm are provided on the website (ftp://meso-a.gsfc.nasa.gov/pub/trmmdocs/3B42_3B43_doc.pdf). The 3B42 (V7) gridded precipitation data set has a 3-hourly temporal and a $0.25° \times 0.25°$ spatial resolution in a global belt extending from 50°S to 50°N covering the period from 1 January 1998 onwards. In this study, the time period 1998-2012 is used.

3.4 IITM

The Indian Institute of Tropical Meteorology (IITM) provide different homogeneous Indian monthly rainfall data sets covering the data period from 1871 to 2012, which are available at (www.tropmet.res.in/static_page.php?page_id=53). The primary source of the meteorological records is the India Meteorological Department. The rainfall products base on a network of rain gauge stations including 306 almost uniformly distributed stations over 30 meteorological subdivisions. Due to a lack of rain gauge stations, four subdivisions in the foothill regions which are parallel to the Himalayan mountain range and two island subdivisions far off-shore have not been considered in the preparation of the rainfall products. In total, the contiguous area comprises about 90 % of the total area of the country India. Details of the data preparation are available at (ftp://www.tropmet.res.in/pub/data/rain/iitm-imr-readme.txt) and references there in.
In this study, the monthly resolved all-India rainfall data set (Parthasarathy et al., 1994), an area weighted rainfall series for all-India based on the 30 subdivisional rainfall series, is used as a proxy for the South Asian summer monsoon rainfall for the 1979-2012 time period.

4 Diagnostic methods

4.1 Identification of monsoon break events

Monsoon breaks are identified based on daily total precipitation from HIRHAM5 RCM simulations following the criterion of Prasanna and Annamalai (2012). They define a break event if, for at least three consecutive days rainfall anomalies averaged over central India (21°-27°N, 72°-85°E) are below one standard deviation. Therefore, only break events persisting three days and more are considered. The details of the identification procedure are described below.

- The first step is to compute a daily climatological total precipitation time series using the HIRHAM5 model simulation for the 1979-2012 period. Then, this climatology is used for the calculation of the daily total precipitation anomalies of every simulated year.
- In a next step central India (21°-27°N, 72°-85°E) (see for central India domain Fig. 5.9 e), a region which experiences dry conditions during break events associated with fluctuations in the location of the monsoon trough is considered to identify break events. After averaging over this domain, the daily total precipitation anomalies are divided by the corresponding standard deviation to get standardised anomalies.
- In a last step, the identification of break days focus on the period 1 July - 17 September, which represents the established phase of the monsoon over India in the HIRHAM5 control run. This avoids the selection of break days during the local onset and withdrawal phases. The reason for choosing a different time period compared to Prasanna and Annamalai (2012) (cp. Fig. 4.1) is due to the limited ability of HIRHAM5 to simulate the Indian summer monsoon rainfall and its intraseasonal variability, documented in detail in section 5.1. While Fig. 4.1 shows the simulated total precipitation climatology averaged over central India for the period 1979-2012 of the HIRHAM5 control run, it demonstrates the use of an subjective criterion that the domain averaged total precipitation should exceed a threshold of 1.2 mm day^{-1} during the established monsoon phase in the control run.

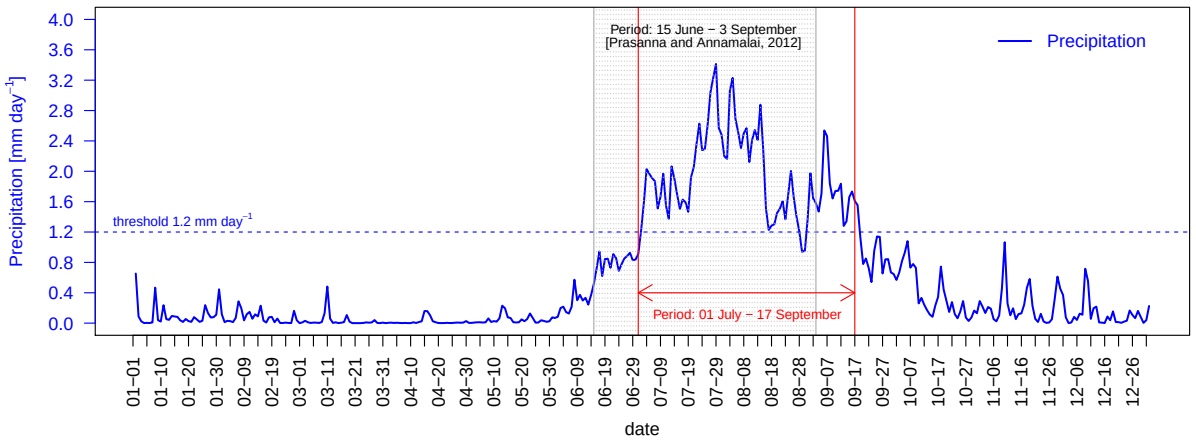

Figure 4.1: Daily climatology of total precipitation [mm day^{-1}] averaged over central India (21°-27°N, 72°-85°E) for the period 1979-2012 from the HIRHAM5 control run. The grey shaded area marks the core period, which represents the established monsoon phase over central India used in Prasanna and Annamalai (2012) based on rainfall observations, while the red arrows highlight the focus period in the HIRHAM5 control run based on the threshold subjectively chosen presented by the dotted blue horizontal line.

For an examination of the mean break anomalous features, composites of break phases are constructed using all identified monsoon break days. Furthermore, in order to identify precursor events and to present the life cycle of monsoon breaks, composites are generated from -20 days to +15 days with day 0 corresponding to the peak break phase over central India. That means, day 0 is defined as the day with the maximum amplitude of total precipitation anomalies during the break phase (Prasanna and Annamalai, 2012). The day 0 composite for any variable is constructed by averaging the day 0 values from all break phases. Likewise, the composites corresponding to 1, 2, ..., n days before (after) day 0 are prepared by backward (forward) shifting of data relative to day 0 for each of the break phases. Following Krishnan et al. (2000) and Prasanna and Annamalai (2012), who recommended the process of compositing as an efficient method to circumvent possible noise that can modulate regional features, five-day averages (pentads) of composite anomalies are calculated. In general, pentad p refers to the composited anomaly averaged over day p - 2, day p - 1, day p, day $p+1$, day $p+2$. That means, for example pentad day 0 is the composited anomaly averaged over day -2, day -1, day 0, day +1 and day +2.

4.2 Moisture and moist static energy budget equations

The nonlinear primitive equations for vertically integrated temperature T and moisture q have the form:

$$\partial_t \widehat{T} + \widehat{D_T T} + \widehat{\omega \partial_p s} = \widehat{Q_c} + \left(\frac{g}{p_T}\right)(F_{rad} + H) \tag{4.1}$$

$$\partial_t \widehat{q} \; + \; \widehat{D_q q} \; + \; \widehat{\omega \partial_p q} \; = \; \widehat{Q_{\mathrm{q}}} \; + \; \left(\frac{g}{p_{\mathrm{T}}}\right) E \tag{4.2}$$

where both T and q are in units of energy ($\mathrm{W\,m^{-2}}$) after absorbing the heat capacity at constant pressure c_{p} and latent heat of condensation L, respectively. The hat $\widehat{(\,)}$ denotes vertical integration over the entire troposphere from 1000 hPa to 10 hPa as follows:

$$\widehat{X} \; = \; \frac{1}{p_{\mathrm{T}}} \int_{10\,\mathrm{hPa}}^{1000\,\mathrm{hPa}} X \, dp \tag{4.3}$$

with convective heating assumed to be limited below 10 hPa. The operators D_T (for temperature) and D_q (for moisture) include horizontal advection and horizontal diffusion terms (K_{H}):

$$D_T \; = \; D_q \; = \; \mathbf{v} \cdot \boldsymbol{\nabla} \; - \; K_{\mathrm{H}} \nabla^2 \tag{4.4}$$

Also, $s = T + \Phi$ is the dry static energy, with Φ the geopotential, g is the acceleration due to gravity and p_{T} (= 1000 hPa − 10 hPa) is the constant reference pressure depth of the troposphere. The net radiative flux into the atmospheric column is

$$F_{\mathrm{rad}} \; = \; F_{\mathrm{SW}}^{\downarrow\,\mathrm{top}} \; - \; F_{\mathrm{SW}}^{\uparrow\,\mathrm{top}} \; - \; F_{\mathrm{SW}}^{\downarrow\,\mathrm{surface}} \; + \; F_{\mathrm{SW}}^{\uparrow\,\mathrm{surface}} \; - \; F_{\mathrm{LW}}^{\uparrow\,\mathrm{top}} \; - \; F_{\mathrm{LW}}^{\downarrow\,\mathrm{surface}} \; + \; F_{\mathrm{LW}}^{\uparrow\,\mathrm{surface}} \tag{4.5}$$

where the upward and downward shortwave radiative fluxes $F_{\mathrm{SW}}^{\uparrow}$, $F_{\mathrm{SW}}^{\downarrow}$, and longwave radiative fluxes $F_{\mathrm{LW}}^{\uparrow}$, $F_{\mathrm{LW}}^{\downarrow}$ are signed in the direction of the flux. The surface sensible and latent heat fluxes are H and E, respectively. Q_{c} and Q_{q} are the convective heating and the moisture sink and satisfy the energy constraint over the air column

$$\widehat{Q_{\mathrm{c}}} \; = \; - \, \widehat{Q_{\mathrm{q}}} \; = \; \left(\frac{g}{p_{\mathrm{T}}}\right) P \tag{4.6}$$

with P the precipitation in $\mathrm{W\,m^{-2}}$.

Studying moist dynamics in the deep tropics requires consideration of physical processes affecting temperature and moisture which is realised by the quantity moist static energy (MSE) (Annamalai, 2010; Prasanna and Annamalai, 2012; Su and Neelin, 2002). The MSE is given by $h = s + q$. Combining Eq. (4.1) and (4.2), the vertically integrated MSE equation can be written as

$$\partial_t (\widehat{T} + \widehat{q}) \; + \; \widehat{D_T T} \; + \; \widehat{D_q q} \; + \; \widehat{\omega \partial_p h} \; = \; \left(\frac{g}{p_{\mathrm{T}}}\right) (F_{\mathrm{rad}} \; + \; H + \; E) \tag{4.7}$$

where $\widehat{\omega\partial_p h}$ is the MSE convergence or vertical advection of MSE. The large terms of vertically integrated convective heating and moisture sink, $\widehat{Q_c}$ and $\widehat{Q_q}$, cancel each other in the MSE equation. Su and Neelin (2002) present the MSE budget as an approach to describe the stability in moist convective zones. The gross moist stability combines the gross dry stability associated with the baroclinic wind convergence and the gross moisture stratification related to the vertical integral of moisture convergence with baroclinic wind. This parameter determines the net thermal stratification as a response to the cancelling effects of adiabatic cooling and diabatic heating associated with rising motions (Annamalai, 2010; Prasanna and Annamalai, 2012; Su and Neelin, 2002).

Considering the anomalies associated with monsoon breaks, the anomalous moisture budget equation under steady state condition ($\partial_t \widehat{q} = 0$) and by using the energy constraint (Eq. (4.6)) can be obtain by subtracting the daily mean value of each term in Eq. (4.2) for the daily climatology from the daily mean value for the identified break days and averaging over composite break days (see section 4.1):

$$P' = \left(\frac{p_T}{g}\right)\left[- \widehat{\omega\partial_p q}' - \widehat{D_q q}'\right] + E' \tag{4.8}$$

where $()'$ indicates the difference between the break days and the daily climatology using the HIRHAM5 model simulations. The four terms of the moisture budget are the anomalous precipitation (P'), the anomalous moisture convergence ($\widehat{\omega\partial_p q}'$), the anomalous horizontal moisture advection ($-\widehat{D_q q}'$) and the anomalous evaporation (E').
By using the same subtracting method, the anomalous MSE equation under steady state condition ($\partial_t \widehat{q} = \partial_t \widehat{T} = 0$) can be obtained from Eq. (4.7) according to

$$\widehat{\omega\partial_p h}' = - \widehat{D_T T}' - \widehat{D_q q}' + \left(\frac{g}{p_T}\right)(F'_{rad} + H' + E') \tag{4.9}$$

The six terms of the MSE budget are the anomalous MSE convergence or vertical advection of MSE ($\widehat{\omega\partial_p h}'$), the anomalous horizontal temperature advection ($-\widehat{D_T T}'$), the anomalous horizontal moisture advection ($-\widehat{D_q q}'$), the anomalous net radiative flux ($F_{rad}{}'$), the anomalous surface sensible heat flux (H') and the anomalous evaporation (E').
For further details see Su and Neelin (2002) and Prasanna and Annamalai (2012).

5 Control run

The HIRHAM5 control run (HH5-CTRL), a continuous simulation was realised for the 1979-2012 period using the standard configuration setup, described in detail in chapter 2, with a small adaptation for the parameterisation of the horizontal diffusion. In order to achieve a stable model execution, the horizontal diffusion coefficient K_6 (see section 2.1.1.2) has been increased by three orders of magnitudes to a value of $K_6 = 1.0 \times 10^{27}$.

5.1 Evaluation

To investigate the skill of HIRHAM5 in simulating the South Asian climate, in particular the South Asian summer monsoon (SASM), the model is validated using the ERA Interim reanalysis fields, different gauges-based observational products and a satellite based data set introduced in chapter 3. The reanalysis fields present information about variables generated by the driving field and provide useful estimates where no observations are available. The evaluation of the HH5-CTRL results is divided in two subsections: spatial distribution (section 5.1.1) and temporal distribution (section 5.1.2).

5.1.1 Spatial distribution

Figs. 5.1-5.3 show a comparison of mean June-September (JJAS) climatologies between HH5-CTRL, ERA Interim, gauges-based observational product APHRODITE and satellite based data set TRMM (if available) for selected fundamental atmospheric model variables. HIRHAM5 reproduces a number of important features of the SASM dynamics, including the large-scale meridional surface temperature gradient over the Indian longitudes, the surface heat low over northwestern India and Pakistan causing a cyclonic flow pattern over the Bay of Bengal in the lower troposphere, the low-level westerly jet over the northern Arabian Sea, an important component in feeding moisture to the monsoon, as well as the Tibetan anticyclone and easterly jet at the upper troposphere. However, some discrepancies are also present.

Over northern India and Pakistan (Northern Indo-Gangetic Plain), the model is characterised by a warm 2m-temperature bias up to +4 K compared to ERA Interim and APHRODITE

(Fig. 5.1). May (2003) found a similar warm bias over the Indus basin using the GCM ECHAM4 and argued that it is caused by an unrealistic drying of the ground during the boreal winter and spring season due to limited water storage capacity of the ground parameterised in the model. The soil drying affects the following wet season (boreal summer and autumn) and leads to a reduced evaporation rate and consequently to a decreased local precipitation formation. In an early study, May (2002) also criticised the simple so-called bucket scheme used in ECHAM4 and recommended a more sophisticated parameterisation scheme for the land-surface hydrology. In contrast, Saeed et al. (2009) suggested that the non-representation of irrigated water is the reason of this positive temperature bias rather than the simple treatment of soil hydrology in the model. In their study with the RCM REMO, they showed that the representation of irrigation by increasing the soil wetness has caused a removal of the warm bias over the Indus basin and concluded that the presence of irrigation is unavoidable for a realistic simulation of the South Asian summer monsoon. This similar feature of a warm bias over the Northern Indo-Gangetic Plain in simulations with different climate models (e.g. ECHAM4 in May, 2003; REMO in Saeed et al., 2009 and Lucas-Picher et al., 2011; RegCM3 in Ashfaq et al., 2009; COSMO-CLM and HIRHAM5 in Lucas-Picher et al., 2011) confirms the conclusions of Saeed et al. (2009) that a characteristic process of the region might be absent in all these models. The largest 2m-temperature deviations of +9 to -20 K (compared to ERA Interim) and +5 to -16 K (compared to APHRODITE) occur over mountain regions, due to the higher horizontal resolution of HIRHAM5, which offers a finer definition of the orography compared to ERA Interim. Especially in mountain regions, due to the lack of stations per grid cell the observationally based variables distribution for APHRODITE strongly depends on the interpolation scheme used to provide continuous gridded coverage. Furthermore, the stations are probably located in valleys close to villages. Hence, the quality of observed variables is limited in remote mountain areas.

A warm 2m-temperature bias over northern India may cause an anomalous intensification of the heat low, which in turn can create an intense pressure gradient in south-north direction and modify the atmospheric dynamics of the monsoon system (Lucas-Picher et al., 2011; Saeed et al., 2009). Contrary to this behaviour, HIRHAM5 is able to simulate the mean sea level pressure distribution (Figs. 5.2 a,b,c) with regional scale features of monsoon circulation, such as the heat low over northwestern India and Pakistan, the monsoon trough with its axis running parallel to the Himalayan foothills, the ridge line on the western part of southern India and the off-shore west coast trough (Srinivas et al., 2012). High differences only occur over mountain regions attributed to the higher horizontal resolution compared to ERA Interim.

The above-mentioned regional characteristics of the lower tropospheric circulation are captured by HIRHAM5 (Fig. 5.2 d). Compared with ERA Interim, discrepancies can be

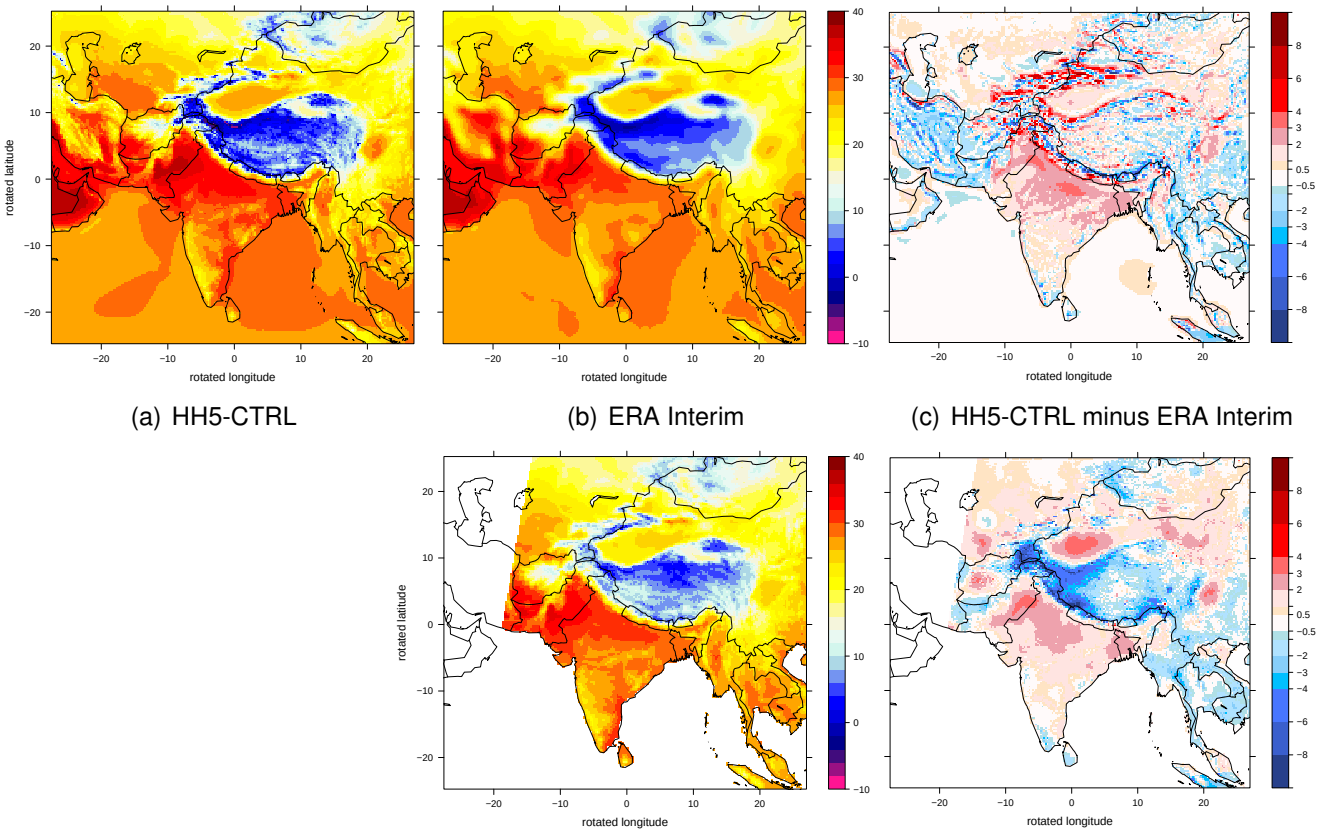

(a) HH5-CTRL (b) ERA Interim (c) HH5-CTRL minus ERA Interim

(d) APHRODITE (e) HH5-CTRL minus APHRODITE

Figure 5.1: Mean JJAS 2m-temperature climatologies [°C] of HIRHAM5 (1979-2012) (a), ERA Interim (1979-2012) (b), APHRODITE (1979-2007) (d) and the difference between HIRHAM5 and ERA Interim (1979-2012) (c) and the difference between HIRHAM5 and APHRODITE (1979-2007) (e)

found especially over northern Iran, Afghanistan, the Takla Matan desert in China, regions at the eastern edge of the Tibetan Plateau, the Himalayas and the southern tip of the Indian Peninsula as a result of the finer resolution of the orography in HIRHAM5 (Figs. 5.2 d,e,f). The major difference between HIRHAM5 and ERA Interim in the pattern of the flow field at 200 hPa is the underestimation of the upper tropospheric easterlies over the Bay of Bengal with largest deviations over the Andaman Sea west of Southern Myanmar (Figs. 5.2 g,h,i). The slightly weaker westerly flow in the lower-level (850 hPa) and a weaker easterly flow in the upper-level (200 hPa) over the northern Bay of Bengal result in a weaker easterly vertical shear in HIRHAM5 than that observed in the reanalysis data in this region (Figs. 5.2 d-i). The easterly vertical wind shear of the mean zonal wind is an important requirement for the northward propagation of the boreal summer intraseasonal oscillation over the tropical Indian Ocean, which is in turn associated with major active and break cycles of the Indian summer monsoon (Jiang et al., 2004). Hence, a sustained easterly vertical shear of zonal winds throughout the summer season as reproduced by HH5-CTRL (not shown) is essential for the skill of the model in simulating monsoon breaks over India (see next section 5.2).

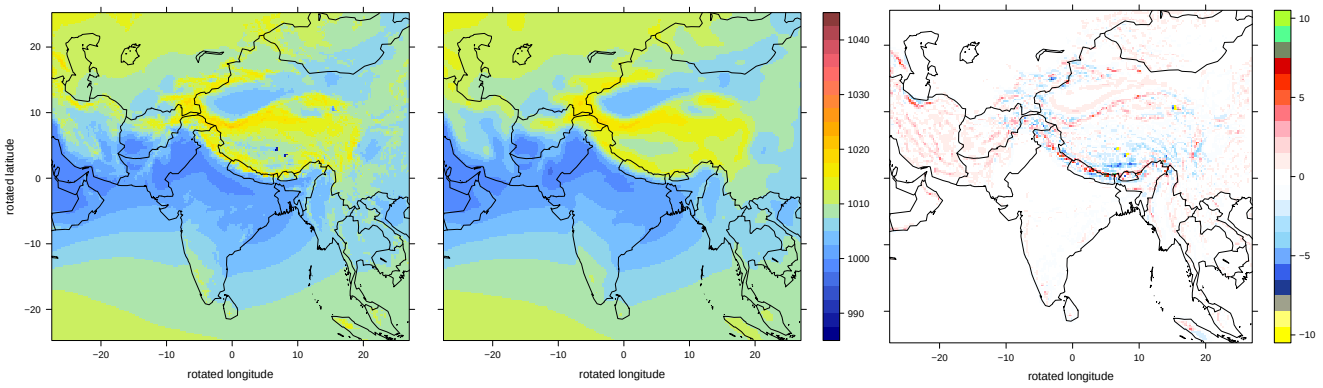

(a) HH5-CTRL mslp (b) ERA Interim mslp (c) HH5-CTRL minus ERA Interim

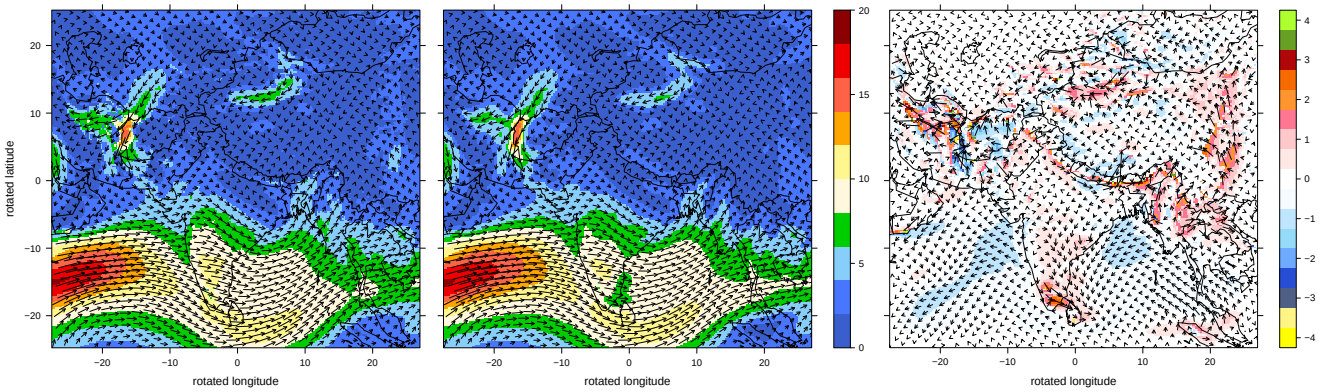

(d) HH5-CTRL 850 hPa wind (e) ERA Interim 850 hPa wind (f) HH5-CTRL minus ERA Interim

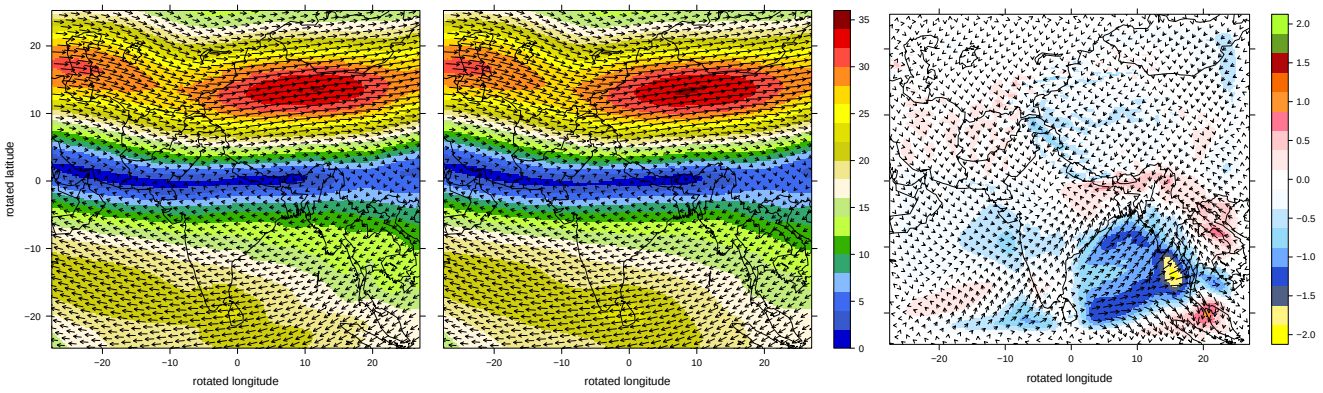

(g) HH5-CTRL 200 hPa wind (h) ERA Interim 200 hPa wind (i) HH5-CTRL minus ERA Interim

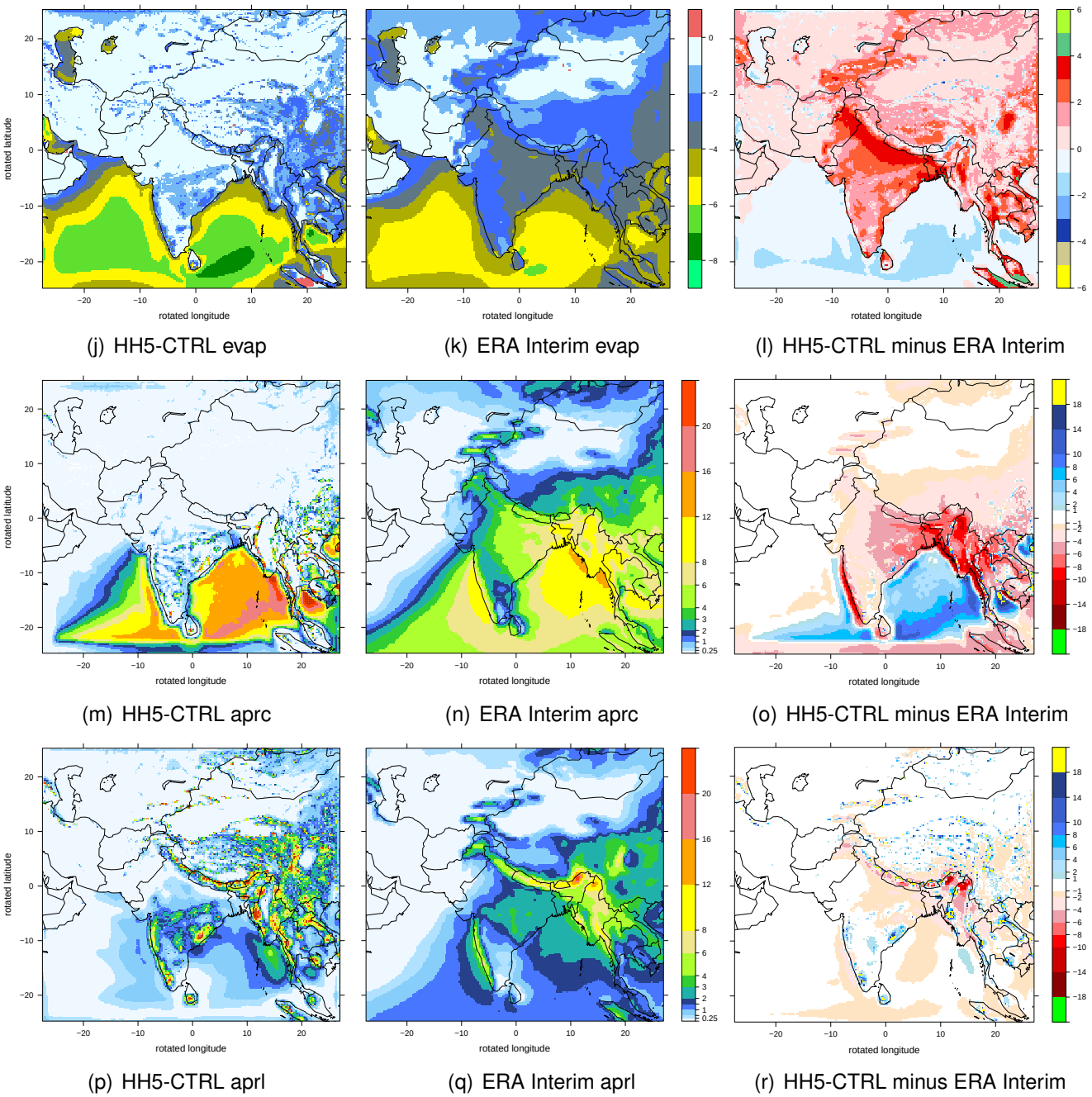

(j) HH5-CTRL evap (k) ERA Interim evap (l) HH5-CTRL minus ERA Interim

(m) HH5-CTRL aprc (n) ERA Interim aprc (o) HH5-CTRL minus ERA Interim

(p) HH5-CTRL aprl (q) ERA Interim aprl (r) HH5-CTRL minus ERA Interim

Figure 5.2: Mean JJAS 1979-2012 climatologies of HIRHAM5, ERA Interim and the difference between HIRHAM5 and ERA Interim for mean sea level pressure [hPa] (a,b,c), 850 hPa wind [m s^{-1}] (d,e,f) and 200 hPa wind [m s^{-1}] (g,h,i), evaporation [mm day^{-1}] (j,k,l), convective precipitation [mm day^{-1}] (m,n,o) and large-scale precipitation [mm day^{-1}] (p,q,r). Note evaporation is negatively defined in the model, i.e. a positive (negative) sign means underestimated (overestimated) evaporation.

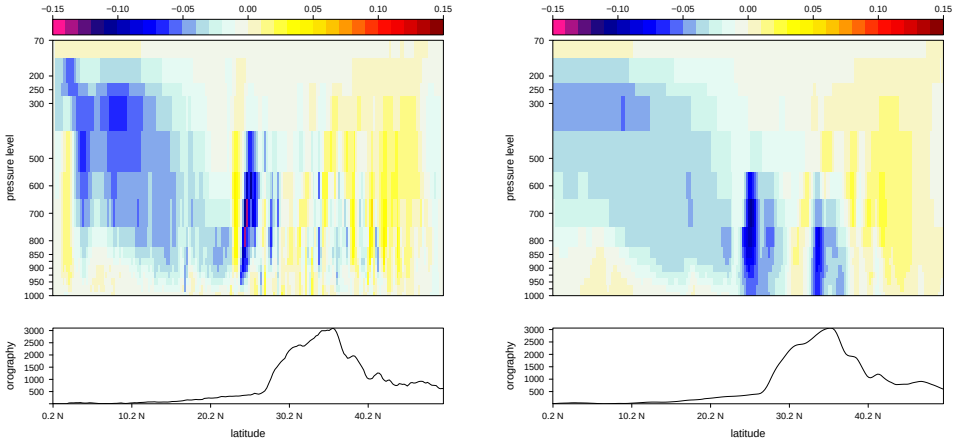

(a) HH5-CTRL (b) ERA Interim

Figure 5.3: Cross-sections of mean JJAS 1979-2012 vertical pressure velocity climatologies [Pa s^{-1}] of HIRHAM5 (a) and ERA Interim (b) averaged along the longitudinal sector of the whole model domain. The bottom panels show the cross-sections of the orography [m] for the same longitudinal sector based on the model and the ERA Interim reanalysis data, respectively. Note positive (negative) values of vertical pressure velocity mean descending (ascending) air.

Raghavan (1973) depicts in a schematic model of the normal monsoon vertical circulation that the Indian region is characterised by two vertical cells. Both, the Hadley cell and the anti-Hadley (monsoon) cell have a common ascending limb between 20° and 30°N. This region of strong upward motion, which is reproduced by HH5-CTRL (Fig. 5.3 a), marks the mean position of the continental ITCZ associated with the seasonal cycle of solar heating during the active monsoon months (Sikka and Gadgil, 1980). Compared to ERA Interim, the location of the descending limb of the monsoon cell close to the equator is simulated by HIRHAM5 (Figs. 5.3 a,b). The sinking limb of the Hadley cell can be noted at around north of 30°N, despite the orography of the Himalayas, which limits the reliability of the simulation. Different from ERA Interim, the model shows an anomalous descending limb at around 23°N (Fig. 5.3 a) caused by strong sinking motions along the foothills of the Himalayas (not shown), which can suppress local convective activity and reduce rainfall in this region (cp. Fig. 5.4).

The precipitation climatologies for ERA Interim, APHRODITE and TRMM (Figs. 5.4 b,d,f) reveal orographically induced rainfall maxima over the southern edge of the Himalayas, near the Western Ghats mountains on the west coast of India and near the Arakan Range and the western slopes of the Bilauktaung Range in Myanmar. Meso-scale convective systems embedded into the monsoon trough (Turner and Annamalai, 2012) induce high rainfall amounts over northeastern India. Another monsoon rainfall maximum is located over the warmest SST of the equatorial Indian Ocean. Considering the HIRHAM5 precipitation pattern (Fig. 5.4 a), the major discrepancies compared to ERA Interim, APHRODITE and TRMM are the underestimation of rainfall over the Indian Peninsula and the overestimation

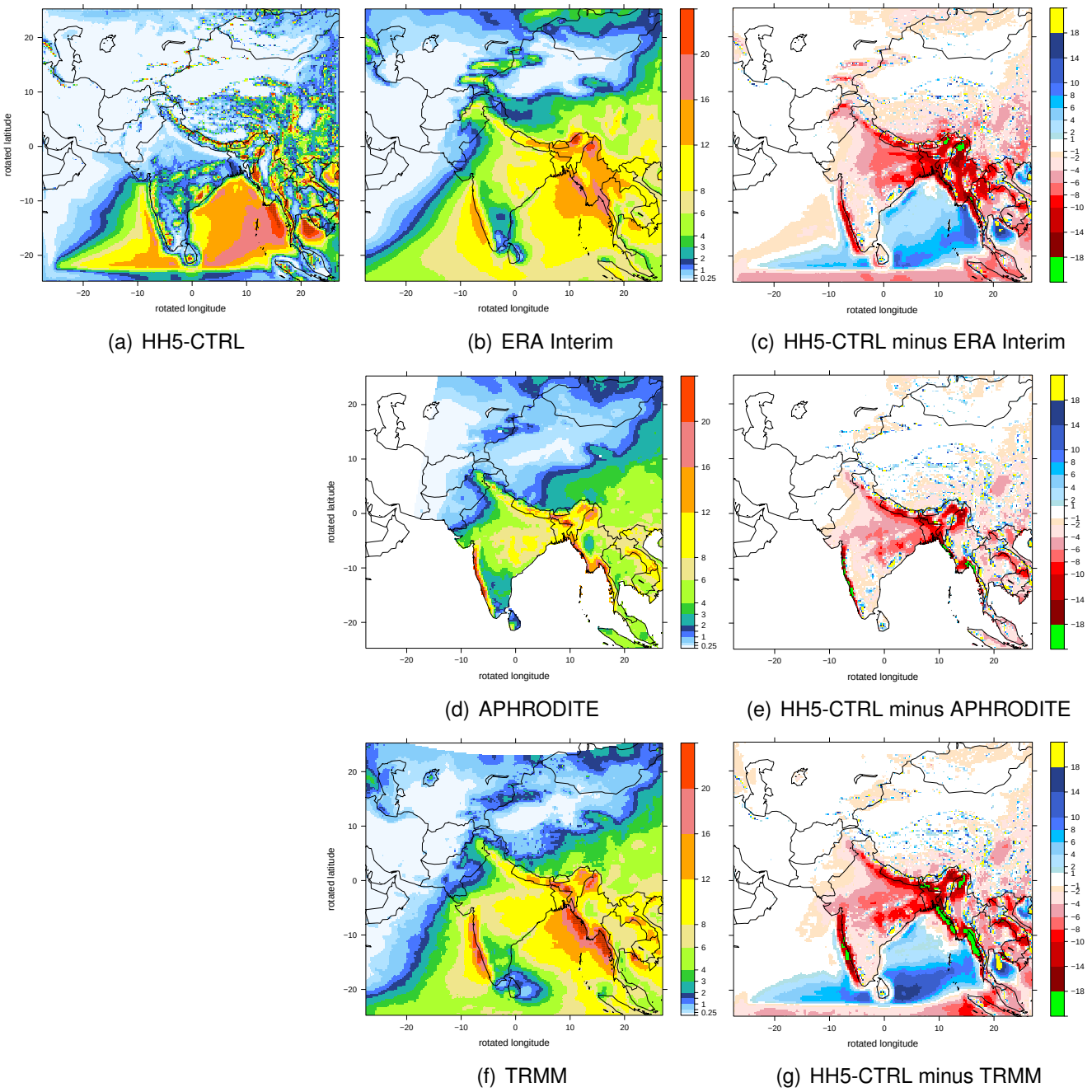

(a) HH5-CTRL (b) ERA Interim (c) HH5-CTRL minus ERA Interim

(d) APHRODITE (e) HH5-CTRL minus APHRODITE

(f) TRMM (g) HH5-CTRL minus TRMM

Figure 5.4: Mean JJAS total precipitation climatologies [mm day^{-1}] of HIRHAM5 (1979-2012) (a), ERA Interim (1979-2012) (b), APHRODITE (1979-2007) (d), TRMM (1998-2012) (f) and the difference between HIRHAM5 and ERA Interim (1979-2012) (c), the difference between HIRHAM5 and APHRODITE (1979-2007) (e) and the difference between HIRHAM5 and TRMM (1998-2012) (g)

over warm Indian Ocean (Figs. 5.4 c,e,g). An exception is the equatorial ocean region at the southern part of the model domain, where the ten-point boundary zone (described in detail in section 2.1.3.2) causes an artificial simulation of the precipitation pattern. This land-sea contrast is also found by Rockel and Geyer (2008), who run the RCM CLM over the Asian domain. They supposed that the overestimation of precipitation over warm oceans seems to remove too much moisture from the atmosphere leading to a reduced water vapour transport into land areas and inhibited precipitation over central India. Lucas-Picher et al. (2011) observed similar deficits in simulating the moisture transport over land with the RCM HIRHAM5 (Christensen et al., 2007) applied over the South Asian region in a horizontal resolution of 0.5°. In this study, the HIRHAM5 in its standard configuration setup generates too less precipitation over the above mentioned orographically induced monsoon rainbelts and fails to simulate the precipitation associated with the meso-scale convective systems of the tropical convergence zone over the heated subcontinent. These deficits in reproducing the convective precipitation over land (cp. Figs. 5.2 m,n,o) could indicate the lack of adaptation of the used convection scheme to the tropical climate. Rockel and Geyer (2008) stressed the importance of the implemented convective scheme in simulating precipitation over tropical climates. They chose the Kain-Fritsch convection parameterisation scheme (Kain and Fritsch, 1993) instead of the Tiedtke scheme (Tiedtke, 1989), used in the standard setting of CLM, after tests which yielded better results for the Kain-Fritsch scheme in some tropical climate regions at a horizontal resolution of 0.5°. Furthermore, many studies examined the sensitivity of model simulated Indian summer monsoon rainfall to the convective parameterisation scheme (e.g. Mukhopadhyay et al., 2010; Sinha et al., 2012; Srinivas et al., 2012;). Srinivas et al. (2012) emphasised that a realistic simulation of the monsoon rainfall requires the realistically representation of physical processes in the model which depends largely on a proper choice of the convection scheme. They evaluated the performance of the advanced research WRF regional model in the simulation of the regional scale precipitation during the Indian summer monsoon using three different schemes and reported the best result with the Betts-Miller-Janjić convective scheme (Betts and Miller, 1986; Janjić, 2000) at 30 km horizontal resolution.

Another striking mismatch in the HH5-CTRL run is the rather noisy precipitation pattern over land areas especially in regions of steep orography (cp. Figs. 5.4 a-g). Gollvik (1999) found similar small-scale noise pattern in precipitation forecasting experiments with the numerical weather prediction model HIRLAM over the Scandinavian mountain region by increasing the horizontal model resolution (22 km, 11 km and 5.5 km). He supposed that a part of this noise is generated by an orographic forcing that cannot be handled by the model dynamics. Furthermore, he assumed that the reason that no improvements could be found for higher horizontal resolutions could be that the convection parameterisation is somewhat

doubtful. Christensen et al. (1996) stressed out that horizontal diffusion will tend to mix air masses of very different nature causing artificial processes like an over-activation of the convective parameterisation scheme leading to non-physical precipitation formation over steep orography. In order to reduce these effects, Christensen et al. (1996) introduced a scheme that switches off horizontal diffusion in regions with steep orography in HIRHAM4. However, the increased value of the horizontal diffusion coefficient K_6 in HH5-CTRL in order to maintain model stability could be a possible reason for the strong overestimation of the total precipitation amounts up to +636.8 mm day^{-1} compared to ERA Interim and +655.1 mm day^{-1} compared to APHRODITE over high mountain ranges (cp. Figs. 5.4 a-g).

An analysis of the spatial patterns of different rain rate categories and their percentage contributions to the total JJAS rainfall amount attempts to get further insight into the seasonal rainfall bias of HH5-CTRL as noted in Fig. 5.4. Five rain rate classes are chosen: less than 0.5 mm day^{-1} (class 1), between 0.5 and 1 mm day^{-1} (class 2), between 1 and 5 mm day^{-1} (class 3), between 5 and 10 mm day^{-1} (class 4), and more than 10 mm day^{-1} (class 5). The proportionate contributions of each rain rate classes are constructed by binning the daily mean precipitation amount for each grid cell in 0.5 mm day^{-1} bins, expressing the percentage share of each rain rate bin to the total JJAS rainfall and adding up all contributions of the corresponding rain rate bins for the different classes. The spatial distributions of the percentage contributions of the five rain rate classes are given in Fig. 5.5 for HIRHAM5 and TRMM, respectively. The rain rate class 1 (< 0.5 mm day^{-1}) accounts for most of the total JJAS rainfall over large areas of Western Asia, the northwestern Arabian Sea, Central Asia and the northwest of China as shown by the TRMM data. HIRHAM5 captures the dominance of this rain category, but tends to overestimate its contribution to the seasonal rainfall. The model shows inaccurate high percentage contributions of the class 1 over the whole of India, especially, over central India and along the foothills of the Himalayas. However, the rain rate categories 4 (5–10 mm day^{-1}) and 5 (> 10 mm day^{-1}) simulated by HH5-CTRL make smaller contributions to the total than observed over the whole country. The analysis indicates that HIRHAM5 has a systematically high bias in the lightest rain rate category (class 1) and a low bias in the moderate and heavy rain rate categories (classes 4 and 5) over northern and central India (Fig. 5.5). This influences the performance of the monsoon simulation and brings out the dry bias of the mean summer monsoon rainfall in these regions (cp. Figs. 5.4 c,e,g). On the other hand, the overestimation of precipitation over the warm oceans is manifested in a large overestimation of the heaviest rain rate category 5 (> 10 mm day^{-1}) over the Bay of Bengal and of the rain rate class 3 (1–5 mm day^{-1}) over the southern Arabian Sea and on the windward side of the Western Ghats. Thus, the spatial distributions of the percentage contributions of different rain rate categories to the seasonal total (Fig. 5.5) are able to identify details of the dry bias over central India simulated by HIRHAM5.

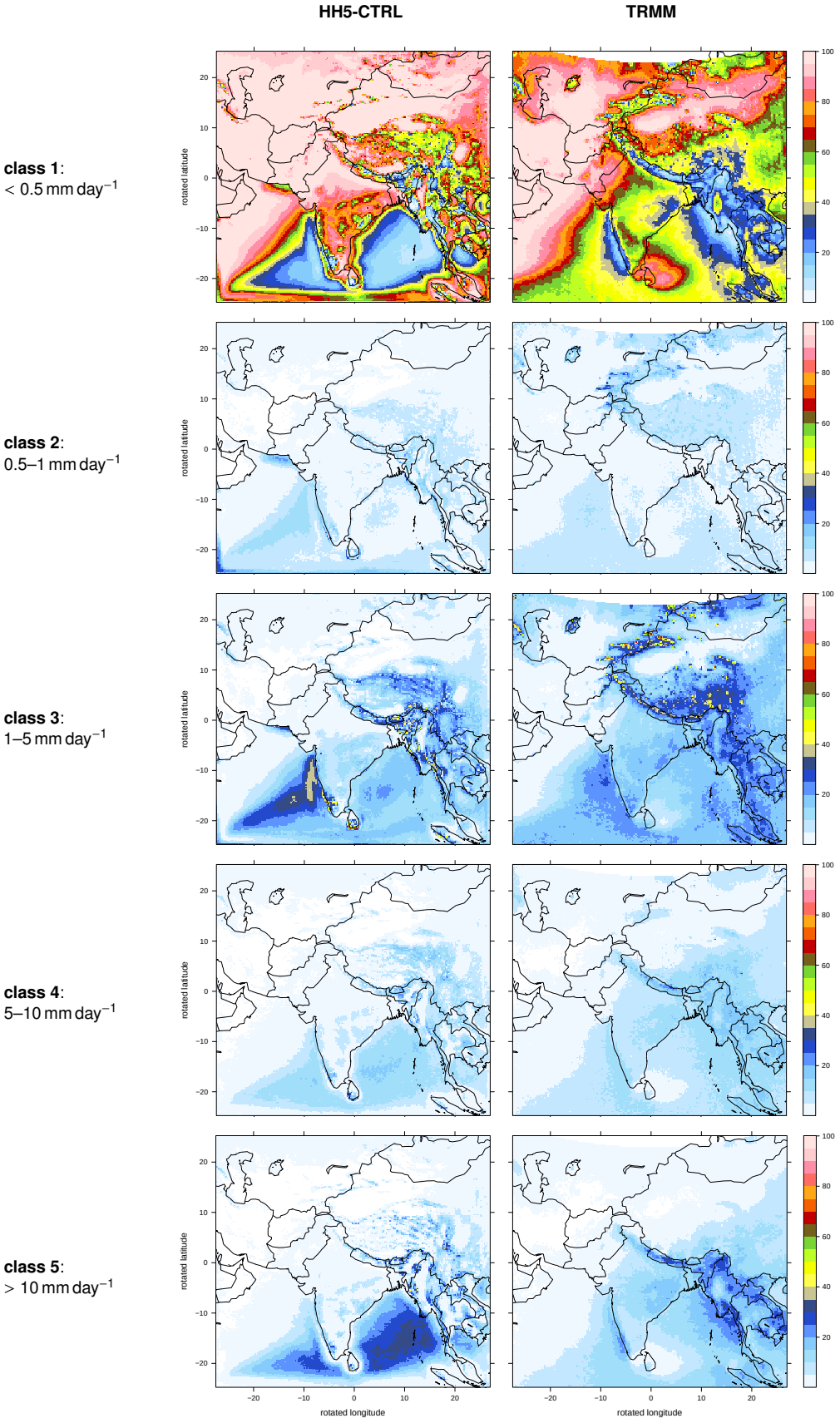

Figure 5.5: Spatial distribution of the percentage contributions of different rain classes to the total JJAS rainfall [%] based on the daily total precipitation of HIRHAM5 and TRMM from 1998-2012. The rainfall classes are: class 1: $< 0.5\,\mathrm{mm\,day^{-1}}$, class 2: $0.5–1\,\mathrm{mm\,day^{-1}}$, class 3: $1–5\,\mathrm{mm\,day^{-1}}$, class 4: $5–10\,\mathrm{mm\,day^{-1}}$ and class 5: $> 10\,\mathrm{mm\,day^{-1}}$.

In summary, the present study suggests that the use of the standard Tiedtke convective scheme (see section 2.1.2.1), which is not adapted to the tropical climate, is responsible for the underestimation of the convective precipitation over the Indian subcontinent and the overestimation over the warm Indian Ocean regions during the Indian summer monsoon. This scheme fails to realistically simulate the formation of off-shore vortices which cause heavy rainfall along the west coast and the genesis of transient low-pressure systems that develop in the Bay of Bengal along the monsoon trough and produce precipitation in the central and eastern parts of India (Srinivas et al., 2012). The reduced moisture transport into land areas results in an underestimation of the convective part of the precipitation over the Indian continent (Figs. 5.2 m,n,o) which leads to a deficiency of the total summer monsoon precipitation especially over central and eastern India (cp. Figs. 5.4 a-g). The decreased local rainfall causes a drying of the ground apparently in a reduced evaporation rate up to $4\,\mathrm{mm\,day^{-1}}$ over the Northern Indo-Gangetic Plain (cp. Figs. 5.2 j,k,l). Further, this low soil wetness (not shown) induces the warm bias over this area during the same boreal summer season (cp. Fig. 5.1 a-e).

5.1.2 Temporal distribution

While the defining variability of a monsoon system is its seasonal nature, the Asian monsoon fluctuates among a wide range of timescales. The annual deviation from its typical seasonal evolution is often of most interest (Waliser, 2006; Yang and Lau, 2006). However, the development of rainfall over the monsoon season, representing the intraseasonal variability can influence the seasonal mean and its interannual variability by active and break phases and have become the focus of increased attention (Goswami, 2012).

Fig. 5.6 compares the amplitude of the intraseasonal variability with that of the interannual variability of the seasonal JJAS mean and the annual cycle for HIRHAM5 and ERA Interim in order to investigate the representation of South Asian monsoon oscillations on subseasonal and annual timescales in the model. Following Goswami (2012), the intraseasonal signal is analysed by filtering daily mean total precipitation anomalies retaining only periods between 10 and 90 days. For the reanalysis data, the standard deviation of the 10 to 90 day filtered daily rainfall anomalies (Fig. 5.6 a) shows a larger amplitude than the interannual variability of the seasonal mean (Fig. 5.6 b), defined by the standard deviation of the JJAS seasonal rainfall mean. This is consistent with the study of Goswami (2012) based on the GPCP rainfall data. Rather, the amplitude of the intraseasonal variability (Fig. 5.6 a) is of the same order of magnitude as that of the annual cycle (Fig. 5.6 c), which is represented by the climatological mean absolute value of the difference between JJAS mean and DJF mean rainfall. This illustrates the important role of the subseasonal behaviour in the nature of the South Asian monsoon precipitation. The standard deviation of the 10 to 90 day filtered rainfall

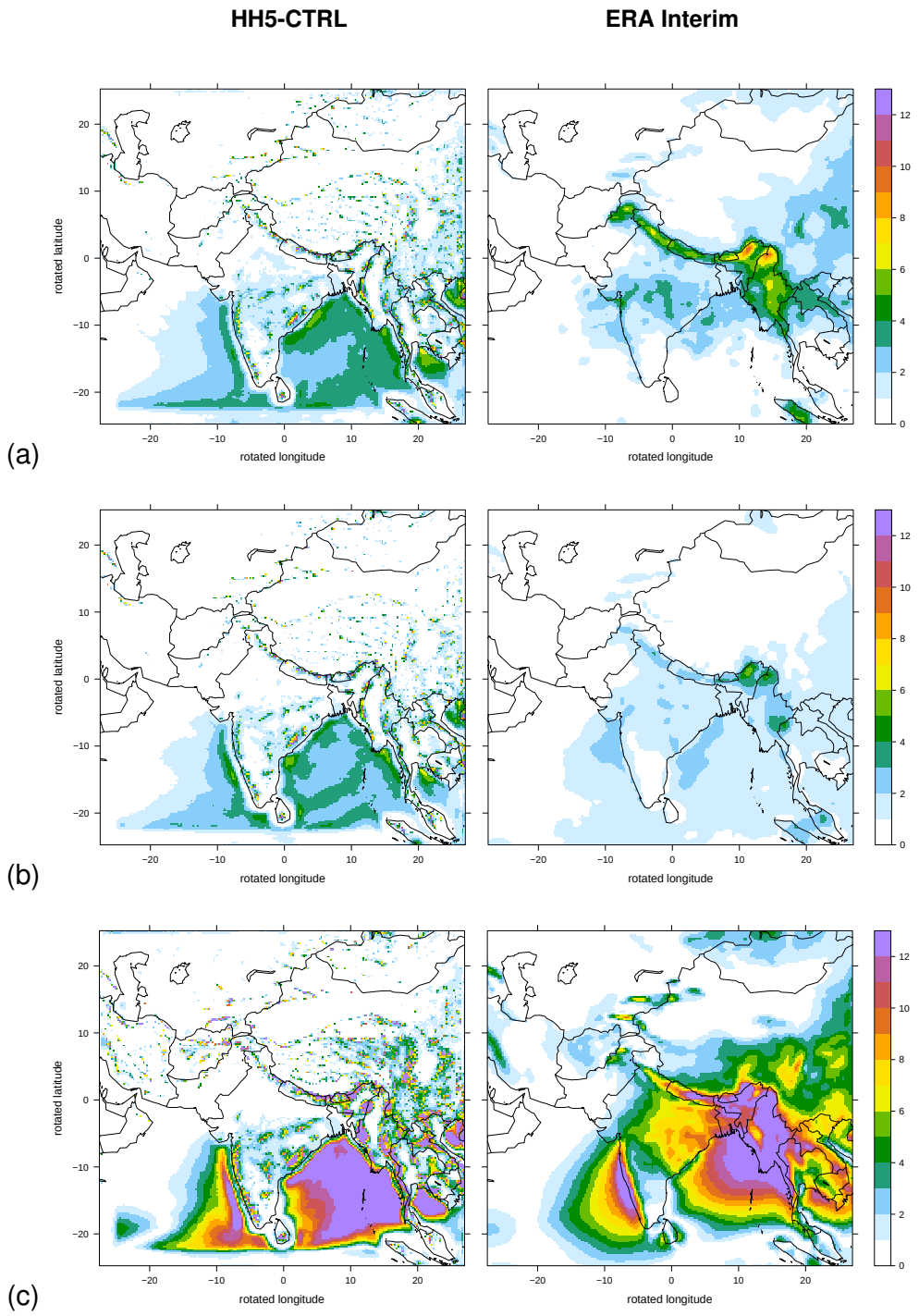

Figure 5.6: Total precipitation variability [mm day^{-1}] maps for HH5-CTRL and ERA Interim for the period 1979-2012. (a) Amplitude of the intraseasonal variability. In this case, the intraseasonal variability is represented by the standard deviation of filtered daily mean total precipitation anomalies based on JJAS seasons. Anomalies are calculated about the daily mean climatology. The data were filtered, retaining periods between 10 and 90 days. (b) Amplitude of the interannual variability. In this case, the interannual variability is defined as the standard deviation of JJAS seasonal mean values of the total precipitation. (c) Amplitude of the annual cycle. In this case, the annual cycle is represented by the climatological mean absolute value of the difference between JJAS mean and DJF mean total precipitation.

anomalies (Fig. 5.6 a) from ERA Interim reveals regions of high intraseasonal variability along the foothills of the Himalayas, at the southeastern edge of the Himalayas, over central India and Sumatra. Apart from the lower magnitude, the same regions show high variability in the seasonal JJAS mean at interannual timescales with the exception of more pronounced variation over the northern Bay of Bengal and along the windward side of the Western Ghats than over central India (Fig. 5.6 b). The pattern of the mean annual cycle from ERA Interim (Fig. 5.6 c) displays the major zones of precipitation in association with the summer monsoon as detected in Fig. 5.4 b.

HIRHAM5 is able to capture the characteristic major role of the seasonal cycle in rainfall associated with the South Asian monsoon (Fig. 5.6 c). However, the model fails to reproduce the dominance of the intraseasonal signal (Fig. 5.6 a) over the interannual signal (Fig. 5.6 b), because HH5-CTRL overestimates the amplitude of the interannual variability of the seasonal JJAS mean especially over the ocean areas (Fig. 5.6 b). The HIRHAM5 limitations noted here could be associated with its systematic error in basic state convective precipitation as discussed in detail in the previous section 5.1.1 and shown in Figs. 5.2 (m,n,o). But even

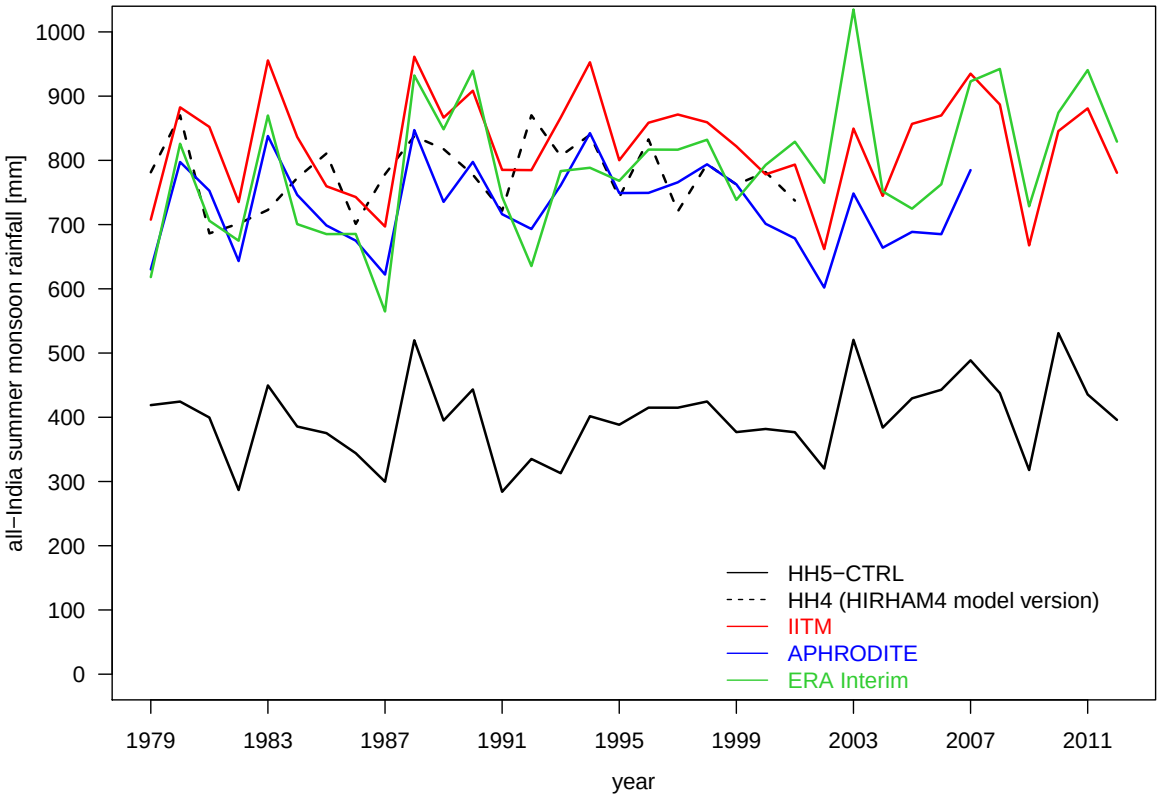

Figure 5.7: Interannual variation of the AIMR (all-India monsoon rainfall) Index [mm], defined by Parthasarathy et al. [1992] as the total rainfall during the June-September period averaged over India of HIRHAM5 (1979-2012), HIRHAM4 (1979-2001), IITM (1979-2012), APHRODITE (1979-2007) and ERA Interim (1979-2012).

though HH5-CTRL shows deficits in the simulation of the summer monsoon precipitation in particular over central and eastern India (cp. Fig. 5.4) the skill of the model in reproducing the intraseasonal variability provides hope for a comprehensive analysis of monsoon break phases in association with subseasonal oscillations (see section 5.2). Especially, the similar signature like that noted in ERA Interim at the intraseasonal timescales over central India (Fig. 5.6 a) promises a realistic identification of monsoon breaks using daily rainfall anomalies averaged over central India following the method of Prasanna and Annamalai (2012) (described in section 4.1).

Data	**Mean [mm]**	**SD [mm]**	**R**
HH5-CTRL	399	63.4	1
HH4	777	53.9	0.28
IITM	825	79.8	0.67
APHRODITE	730	66.0	0.58
ERA Interim	790	104.6	0.71

Table 5.1: Mean and standard deviation (SD) of the AIMR Index [mm] for HIRHAM5 (1979-2012), HIRHAM4 (1979-2001), observationally based datasets IITM (1979-2012) and APHRODITE (1979-2007) and reanalysis ERA Interim (1979-2012) and correlation (R) of all data sets with HIRHAM5 for a common time period.

The ability of HIRHAM5 to reproduce the SASM is further analysed using the All-India Monsoon Rainfall (AIMR) Index. This index was defined by Parthasarathy et al. (1992) as the cumulative value of the total rainfall during the June-September period averaged over India and represents a measure of the strength of the Indian summer monsoon. Fig. 5.7 compares the interannual variation of the AIMR index for HH5-CTRL, HIRHAM4, ERA Interim and observationally based data sets IITM and APHRODITE. HIRHAM5 in its standard configuration setup underestimates the AIMR index by a factor of around two. On average, the run of the earlier model HIRHAM4 is close to the reference data, but the control run of the newer HIRHAM5 shows a more precise simulation of the interannual variability. Tab. 5.1 shows the mean values and the standard deviations of the AIMR Index for the same data sets as in Fig. 5.7. Although HIRHAM5 underestimates the mean all-India summer monsoon rainfall sum, the interannual variability (measured by the standard deviation) is

well reproduced in the model (63.4 mm) and similar to that of the observationally based data sets, especially APHRODITE (66.0 mm). Whereas, the variability in ERA Interim is clearly overestimated (104.6 mm). Correlations of the simulated annually AIMR index for HIRHAM5 with indices in the reference data sets (Tab. 5.1) reveal the consistency of the HH5-CTRL to its driving field (R = 0.71) and the ability of the model in reproducing the observed interannual rainfall variability over India when compared with the IITM time series (R = 0.67).

Despite the limitations of HIRHAM5 in simulating the rainfall basic state (shown in section 5.1.1), the represented interannual and in particular intraseasonal variability of the SASM in the HH5-CTRL run (shown in section 5.1.2) forms the basis for the comprehensive monsoon break analysis as discussed next in section 5.2.

5.2 Monsoon breaks

The summer monsoon season of South Asia (June to September) is the main rainy season of the region (Ding and Sikka, 2006). Over a major part of continental India, the rainfall during these months accounts for about 70–80 % of the total annual rainfall and is therefore of paramount importance for the agriculture and socioeconomic sector. Within the established phase, the monsoon exhibits substantial intraseasonal variability and fluctuates between periods of enhanced and reduced rainfall, defined as active and break monsoon phases (Annamalai, 2010; Annamalai and Slingo, 2001; Krishnan et al., 2000; Prasanna and Annamalai, 2012). Although, monsoons are not a period of steady rains, prolonged phases of dryness can result in severe droughts and famines and hence influence the lives of more than one billion people in the South Asian monsoon region (Gadgil and Kumar, 2006; Raghavan, 1973).

The objective of the present study is to improve the understanding of moist dynamical processes that initiate and maintain breaks during the SASM. Therefore, the following approach is adopted. First, the output of the HH5-CTRL is applied to the identification procedure of breaks by Prasanna and Annamalai (2012) as described in detail in section 4.1. Second, by using compositing techniques, the spatiotemporal evolution of breaks is investigated. Finally, to get insight in the interaction between moist physics and circulation and to quantitatively estimate the various moist processes contributing to anomalous negative rainfall anomalies over central India, moisture and moist static energy budgets are analysed.

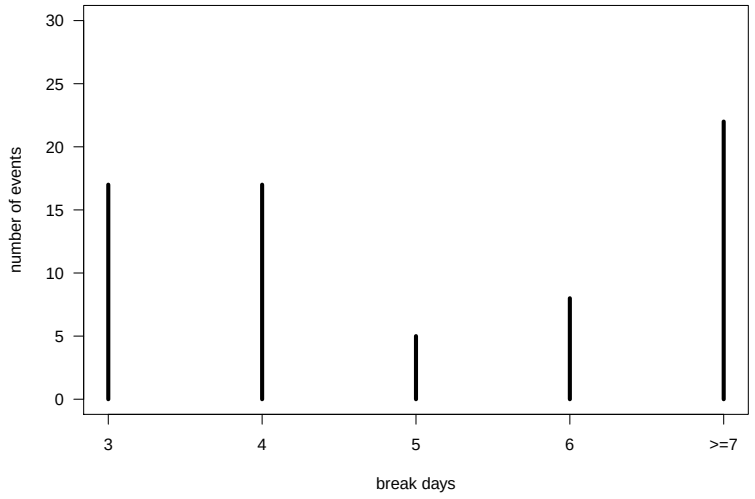

Figure 5.8: Histogram of break days identified from modeled total precipitation averaged over central India (21°-27°N, 72°-85°E) (see Fig. 5.9 e) using the HH5-CTRL run (1979-2012).

5.2.1 Break events

Following the definition of Prasanna and Annamalai (2012), 69 monsoon break phases are identified during the 34 years (1979-2012) of the HH5-CTRL run. The total number of break days for these 69 cases is 386. Consistent with the results of Prasanna and Annamalai (2012), who studied extended monsoon breaks during the period 1989-2007 based on daily gridded rainfall observations and the ERA Interim reanalysis, short breaks (3 days) and extended breaks ($\geq$ 7 days) tend to occur most frequently with the exception that breaks persisting for four days show the same frequency as breaks persisting for three days (see Fig. 5.8).

5.2.2 Characteristic anomaly patterns of breaks

To document the characteristic features of break phases, Fig. 5.9 shows spatial patterns of break composite anomalies constructed from the 386 break days for selected fundamental

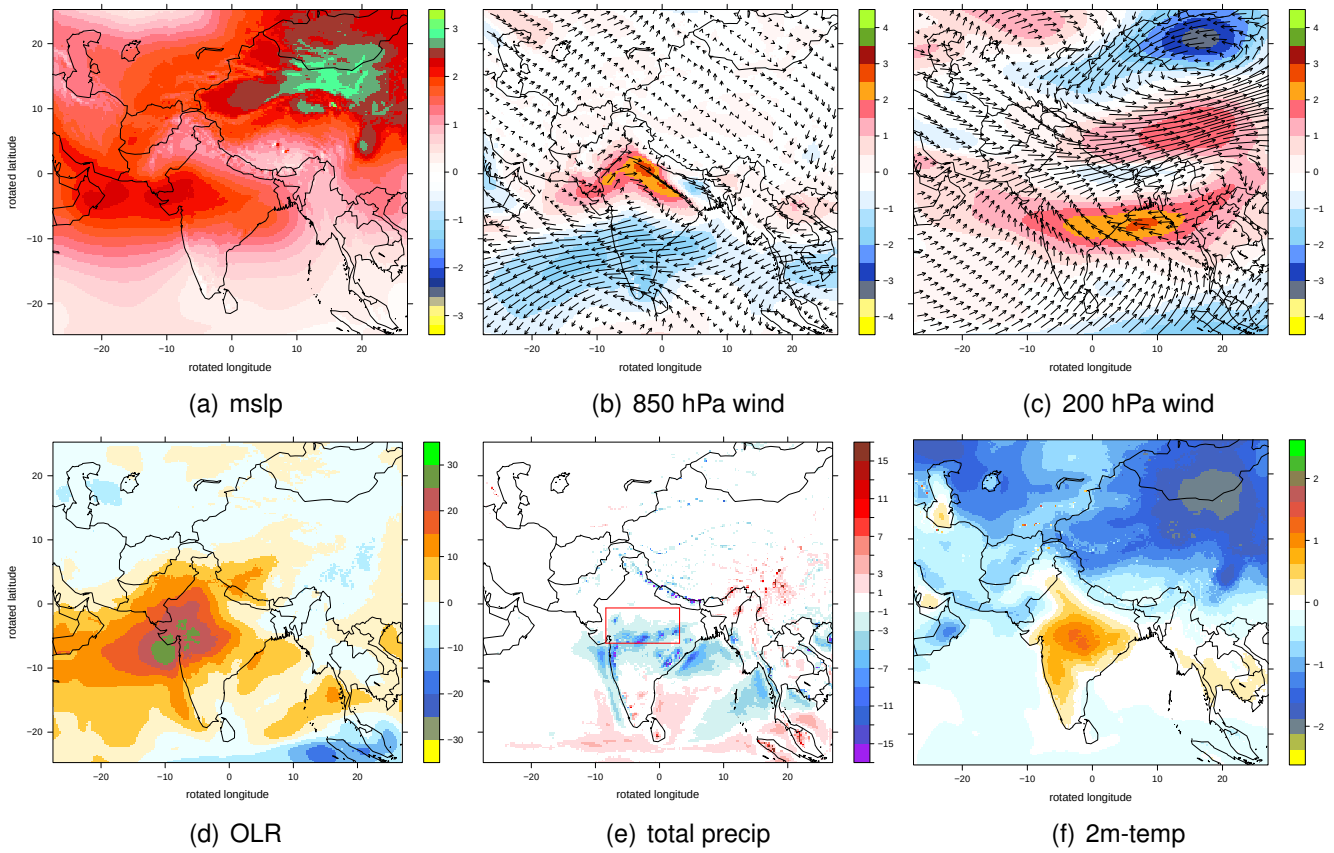

Figure 5.9: Break composite anomalies of mean sea level pressure [hPa] (a), 850 hPa wind [m s^{-1}] (b), 200 hPa wind [m s^{-1}] (c), outgoing longwave radiation at the top-of-the atmosphere (TOA) [W m^{-2}] (d), total precipitation [mm day^{-1}] (e) and 2m-temperature [K] (d) from the HH5-CTRL run. The composites are constructed from all 386 identified break days. The red box in (e) marks the central India region (21°-27°N, 72°-85°E).

atmospheric model variables. During monsoon breaks the monsoon trough migrates north of the plains of northern India toward the foothills of the Himalayas leading to an increase in sea-level pressure values south of the trough (Raghavan, 1973). HIRHAM5 captures this feature of a high pressure ridge over central India (Fig. 5.9 a) and the formation of an anticyclonic flow in the lower troposphere (Fig. 5.9 b). This ridge is often mentioned as an eastward extension of the subtropical anticyclone over Iran and Arabia (e.g. Ramaswamy, 1962; Raghavan, 1973). Increased northwesterly low-level wind anomalies evolve at the northern edge of the high pressure ridge along the foothills of the Himalayas. The low-level westerly jet, which approaches India from across the Arabian Sea during normal monsoon is suppressed by easterly winds during the break-monsoon. The anticyclonic flow over India and the anomalous easterlies over the Arabian Sea suggest a major reduction in the moisture transport into the monsoon region (Krishnan et al., 2000). Moreover, an anomalous cyclonic flow structure is found south of India over the central Indian Ocean, which feeds the south-east coast of India with moist air. In the upper troposphere the Tibetan anticyclone shifts southeastwards over Bangladesh and northern Myanmar leading to increased westerlies over northern India and the Tibetan Plateau (Fig. 5.9 c). Krishnan et al. (2000) also noted the presence of upper level westerly wind anomalies over the north of India using the NCEP-NCAR reanalysis data. These changes in the atmospheric conditions lead to generally cloudless skies and rainless days over the plains of northern India (Raghavan, 1973). In the Tropics, deep convective systems have low cloud-top temperatures and can be identified by small outgoing longwave radiation (OLR) values, whereas a scarcity or absence of clouds is characterised by large values of OLR (Krishnan et al., 2000). During breaks, the regions of suppressed convection, inferred from positive OLR anomalies are found over central India extending westwards over Pakistan, the Arabian Sea and parts of Arabia with maximum OLR values of about +30 $W\,m^{-2}$ occurring over western central India and adjacent areas over the Arabian Sea (Fig. 5.9 d). Eastwards, the positive anomalies extends over the Bay of Bengal into the Andaman Sea and the Gulf of Thailand. While the monsoon shows a break in the above mentioned regions, convection is active over the equatorial Indian Ocean with a maximum amplitude of OLR anomalies of around -18 $W\,m^{-2}$ west of Sumatra. Furthermore, small negative OLR anomalies over parts of Indo-China and central China suggest regions with enhanced convection. The out of phase structure of the two favourable locations of maximum cloud zones associated with the continental and the oceanic TCZ over the Indian longitudes is well studied (Gadgil and Asha, 1992; Sikka and Gadgil, 1980) and often referred as a bimodal structure in convection (Annamalai and Sperber, 2005). Annamalai and Slingo (2001) emphasised the occurrence of a further dipole pattern in the West Pacific by investigating OLR pattern of active/break phases for the dominant 30-60 day intraseasonal mode. They presented, both the north-south dipole over

the Indian longitudes and the complementary south-north dipole over the West Pacific as a characteristic quadrapole structure in convection over the Asian summer monsoon domain. The identified substantial rainfall reductions over a northwest-southeast diagonally oriented stretch from western central India over the northern Bay of Bengal to the Gulf of Thailand and positive rainfall anomalies over the equatorial Indian Ocean, southern central China and parts of Indo-China (Fig. 5.9 e) suggest this quadrapole structure in convection in spite of the limit of the model domain. While the precipitation is suppressed over large areas of central India, the southeastern tip of India and the island Sri Lanka are found to be a principal region of rainfall within the break period according to Raghavan (1973). Consistent with observations (Raghavan, 1973), the near surface temperature increases to above-normal values over the plains, central and western India during break periods (Fig. 5.9 f). Lower temperatures occur in north-east and north-west India as seen in Dunning et al. (2015), which use daily mean surface air temperature observations for June-August 1969-2005.

In summary, the composite patterns from all the 386 break days (Fig. 5.9) resemble the characteristic anomalous rainfall patterns of extended breaks as identified by Prasanna and Annamalai (2012). Furthermore, the composites are consistent with the spatial heating patterns and circulation features associated with the 30-60 day (referred as the 40-day) intraseasonal mode of the SASM as described by Annamalai and Slingo (2001). This demonstrates the dominant role of the 40-day mode compared to the weaker 15-day (10-20 day) mode in the subseasonal variability of the summer monsoon in accordence with the results of Annamalai and Slingo (2001). Hence, by using unfiltered data the following study concentrates on the identification of extended monsoon breaks in relation to the 40-day time scale.

5.2.3 Moist dynamical processes during the evolution of monsoon breaks

Precipitation and circulation anomalies

The break composite anomaly patterns of the selected atmospheric variables, prepared from all the 386 break days (Fig. 5.9) reproduce the observed circulation changes with the onset of monsoon breaks. However, these changes represent an effect rather than a necessary causative factor of monsoon breaks (Raghavan, 1973). Therefore, in order to study the genesis of monsoon breaks a time sequence of total precipitation, OLR (not shown), 850 hPa wind, 200 hPa wind and 850 hPa geopotential height composite anomalies are constructed and presented in Fig. 5.10.

The space-time structure of the composite precipitation from -20 days to +5 days (Fig. 5.10 a)

and OLR (not shown) anomalies reveal two major features. First, the rainfall anomalies show a pronounced northward propagation over India and the Bay of Bengal. This transition of convection from the oceanic to the continental zone represents one of the three identified propagating components, which dominates the 40-day intraseasonal mode of the Asian summer monsoon (Annamalai and Slingo, 2001; Annamalai and Sperber, 2005; Sikka and Gadgil, 1980). Second, the monsoon break phase over central India remains for 15 days or more (from -5 days to +10 days, not shown) in accordance with the results of Prasanna and Annamalai (2012).

At -15 days, positive rainfall anomalies over central India and the northern Bay of Bengal are bounded by negative rainfall anomalies along the foothills of the Himalayas in the north and near-equatorial Indian Ocean and southern parts of the Indian peninsula in the south (Fig. 5.10 a). With the northward movement of the oceanic zone of suppressed convection and precipitation, the negative anomalies intensify and cover central India and the entire Bay of Bengal by day -5. The transition to westerly winds over the plains of northern India in the lower troposphere (Fig. 5.10 b) leads to a collapse of the monsoon trough and brings the monsoon into its break phase over India. The presence of westerly winds over the plains of India during the establishment of a monsoon break was also found by other studies (e.g. Annamalai and Sperber, 2005; Krishnan et al., 2000; Raghavan, 1973). From -10 days onward, an anticyclonic anomaly develops over the continental TCZ regime (cp. Figs. 5.10 b,d) accompanied by strong easterly wind anomalies over the southern Arabian Sea in the lower troposphere. This clockwise anomaly over India could be the northern part of the large scale structure of an anomalous anticyclonic pair shown in earlier studies (e.g. Annamalai and Slingo, 2001; Annamalai and Sperber, 2005; Krishnan et al., 2000; Prasanna and Annamalai, 2012). It has been noted that, the symmetric pattern of these twin anticyclones with respect to the equator indicates the generation of a Rossby wave as a dynamical response to an anomalous heat source (Annamalai and Slingo, 2001; Annamalai and Sperber, 2005; Krishnan et al., 2000; Prasanna and Annamalai, 2012). The suppressed convection over the near-equatorial Indian Ocean (not shown) act as a diabatic heating sink, due to the reduced latent heating during the initiation phase of breaks. This in turn, induce the formation of a Rossby wave signal based on the theories of Webster (1972) and Gill (1980). A cyclonic shear in the equatorial Indian Ocean (Fig. 5.10 b) can be noted together with the evolution of convection (not shown) over the oceanic TCZ regime from -5 days onward. In the upper troposphere, westerly wind anomalies appear over northern India at day -5 (Fig. 5.10 c). Ramaswamy (1962) emphasised that this southward intrusion of the sub-tropical westerly jet into Indo-Pakistan associated with the weakening and southeastward shift of the Tibetan anticyclone plays a fundamental role in the development of breaks. He concluded that southward penetrating extratropical troughs by

controlling the movement of the Iranian high pressure system should be considered as the primary cause for the dry weather over India. At day 0, negative rainfall anomalies extending over the entire Indian monsoon region, stretching from western central India through the Bay of Bengal to the Gulf of Thailand along a northwest-southeast oriented diagonal. From day -5 onward, positive rainfall anomalies over the near-equatorial Indian Ocean suggest the formation stage of convection over the oceanic regime. As time progresses these positive anomalies grow in intensity and move northward and indicate the beginning of an active phase of the monsoon over India.

Moisture budget

In order to identify precursors and important moisture processes that lead to breaks a moisture budget analysis is performed following the method by Prasanna and Annamalai (2012) described in detail in section 4.2. The four terms of the moisture budget are the anomalous precipitation ($P^{'}$), moisture convergence ($-\widehat{\omega\partial_p q}^{'}$), horizontal moisture advection ($-\widehat{\mathbf{v}\cdot\boldsymbol{\nabla}q}^{'}$) (horizontal diffusion neglected) and evaporation ($E^{'}$) (see section 4.2). Fig. 5.11 shows the space-time evolution (-20 days to +5 days) of vertically integrated anomalous moisture convergence (a) and anomalous horizontal moisture advection (b), and anomalous evaporation (c), while anomalous precipitation is already shown in Fig. 5.10 (a). A positive (negative) sign denotes net moisture convergence (moisture divergence) in Fig. 5.11 (a). Similarly, a positive (negative) sign indicates net moist advection (dry advection) into the column in Fig. 5.11 (b). Evaporation is negatively defined in the model (cp. Fig. 5.2 j). Hence, a positive (negative) sign means reduced (enhanced) evaporation during monsoon breaks in Fig. 5.11 (c).

Consistent with other studies (e.g. Annamalai, 2010; Prasanna and Annamalai, 2012), precipitation (Fig. 5.10 a) and moisture convergence (Fig. 5.11 a) are the dominant terms in

	central India
$P^{'}$	-42.9 (100 %)
$-\widehat{\omega\partial_p q}^{'}$	-46.6 (65.5 %)
$-\widehat{\mathbf{v}\cdot\boldsymbol{\nabla}q}^{'}$	14.6 (-20.5 %)
$E^{'}$	-1.3 (1.8 %)
residual term	-8.7 (12.2 %)

Table 5.2: Area-averaged moisture budget anomalies in W m^{-2} for central India (21°-27°N, 72°-85°E) at day 0 (pentad) defined as the peak phase of monsoon breaks and maximum amplitude of rainfall anomalies. Numbers in parenthesis give percentage values relative to the area-averaged precipitation anomaly $P^{'}$.

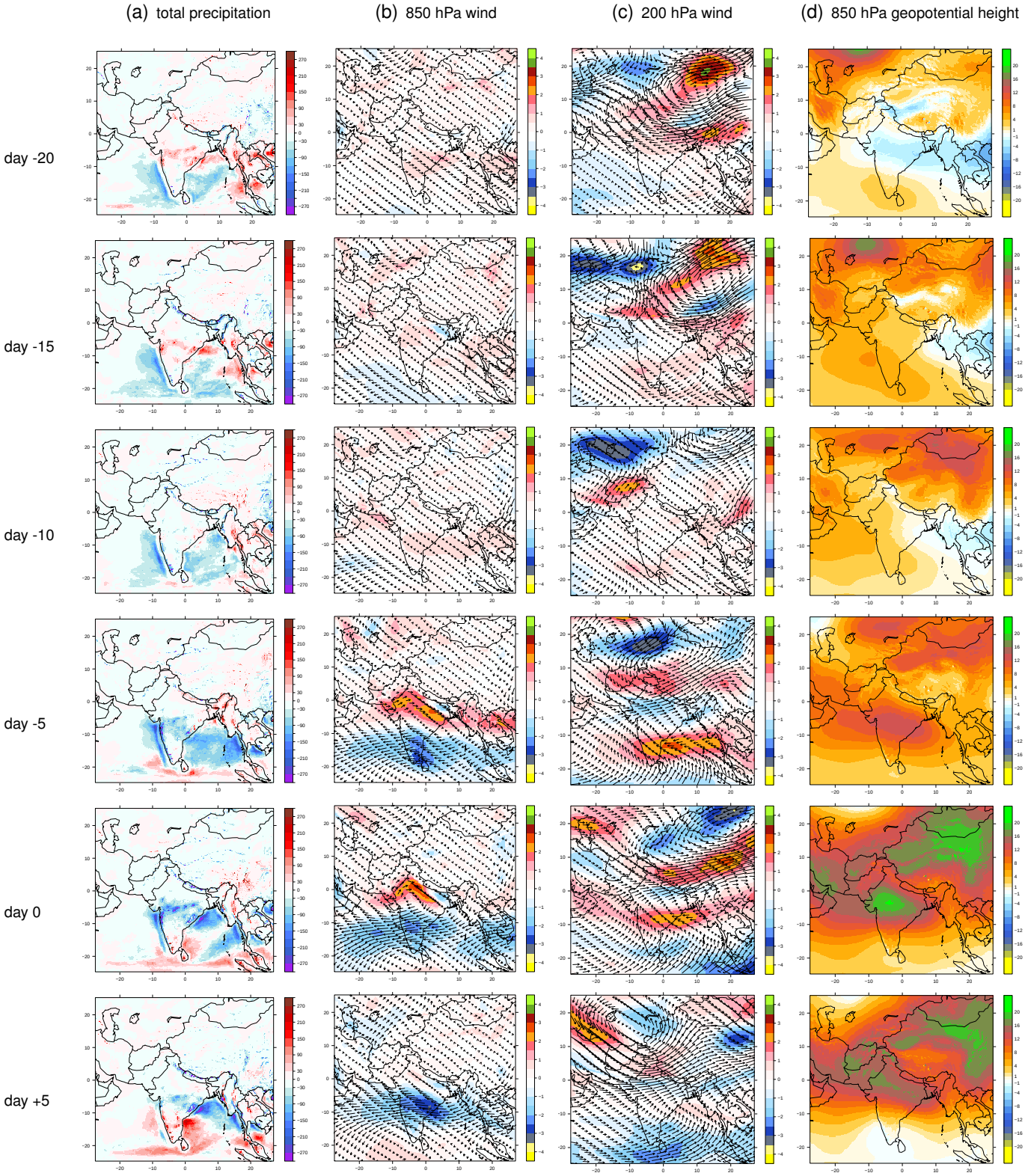

Figure 5.10: Space-time evolution of composite anomalies of total precipitation [$W\,m^{-2}$] (a), 850 hPa wind [$m\,s^{-1}$] (b), 200 hPa wind [$m\,s^{-1}$] (c) and 850 hPa geopotential height [m] (d) from HH5-CTRL during breaks. Units of precipitation anomalies are in $W\,m^{-2}$ ($mm\,day^{-1} \times 28.935\,19$) so that around $29\,W\,m^{-2}$ corresponds to around $1\,mm/day^{-1}$. The composites are shown from days -20 to days +5 (pentads) with day 0 defined as the peak phase of monsoon breaks and maximum amplitude of rainfall anomalies. Each panel is 5 days apart.

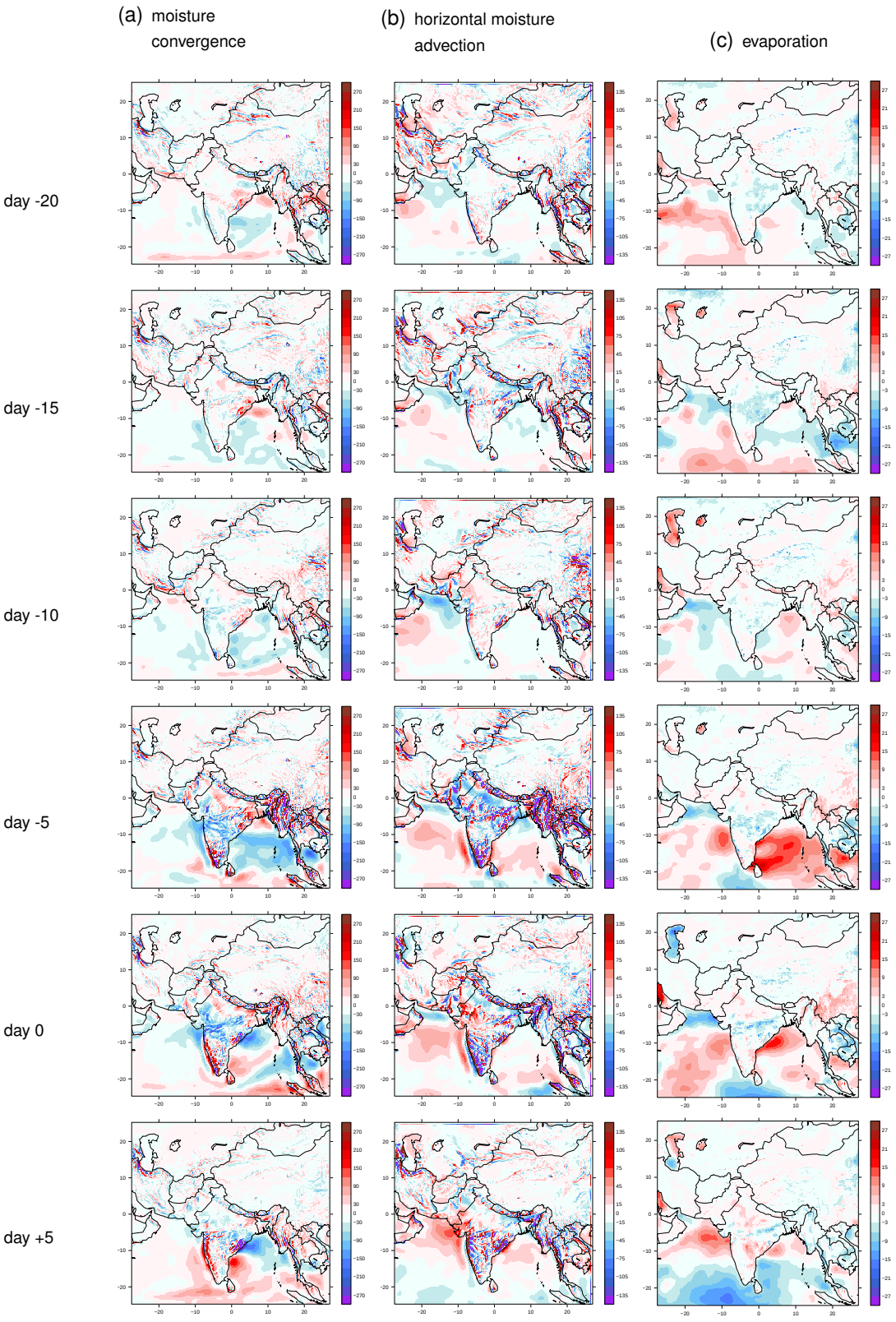

Figure 5.11: Moisture budget: space-time evolution of composite anomalies of vertically integrated moisture convergence [W m^{-2}] (a) and horizontal moisture advection [W m^{-2}] (b), and evaporation [W m^{-2}] (c) from HH5-CTRL during breaks. The precipitation is already shown in Fig. 5.10. The scaling differs for each variable. Note evaporation is negatively defined in the model, i.e. a positive (negative) sign means reduced (enhanced) evaporation. The composites are shown from days -20 to days +5 (pentads) with day 0 defined as the peak phase of monsoon breaks and maximum amplitude of rainfall anomalies. Each panel is 5 days apart.

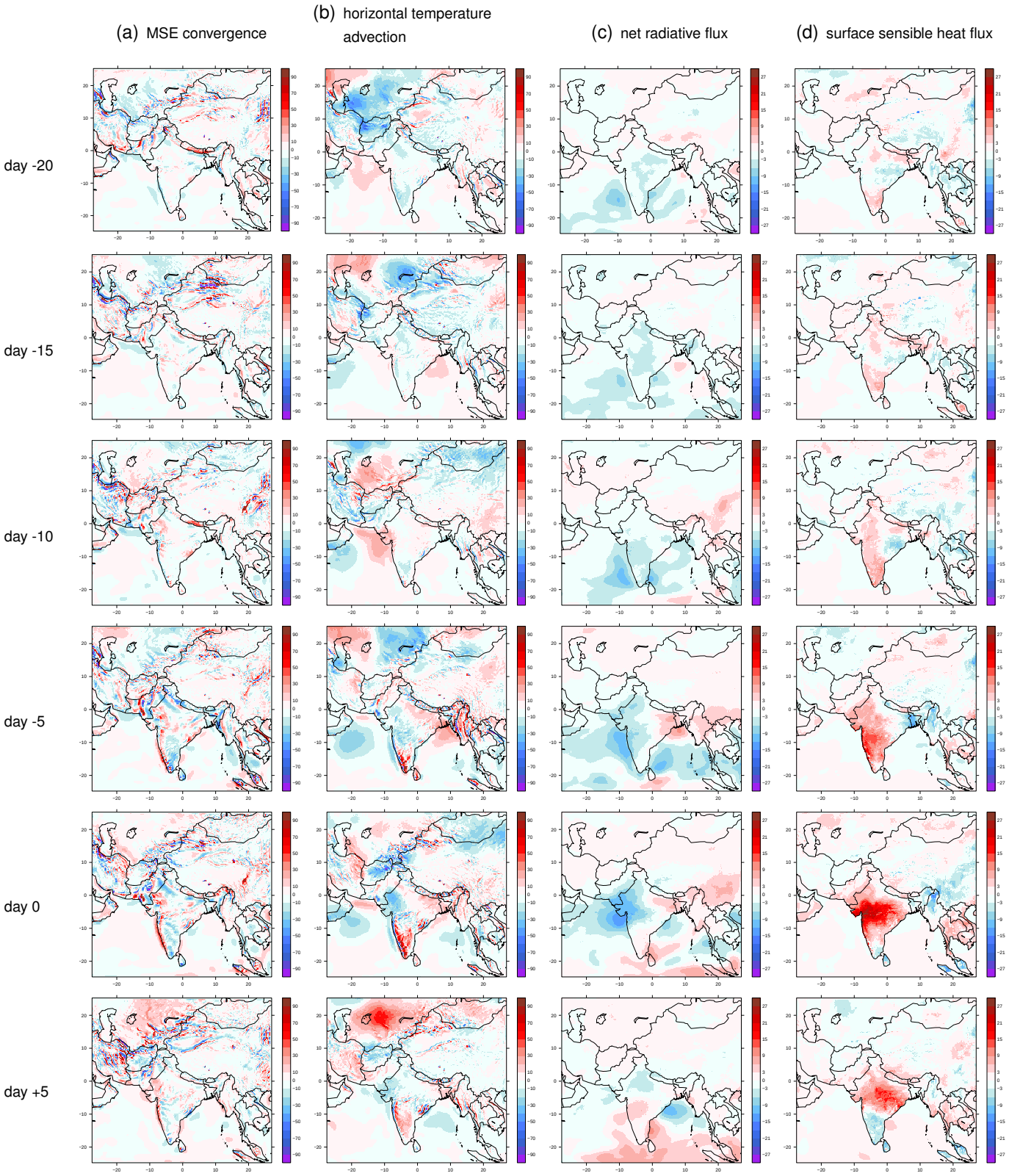

Figure 5.12: MSE budget: space-time evolution of composite anomalies of vertically integrated MSE convergence [W m^{-2}] (a) horizontal temperature advection [W m^{-2}] (b), net radiative flux [W m^{-2}] (c) and surface sensible heat flux [W m^{-2}] (d) from HH5-CTRL during breaks. The horizontal moisture advection and evaporation are already shown in Fig. 5.11. The scaling differs for each variable. The composites are shown from days -20 to days +5 (pentads) with day 0 defined as the peak phase of monsoon breaks and maximum amplitude of rainfall anomalies. Each panel is 5 days apart.

the moisture budget compared to moisture advection and evaporation (Fig. 5.11 b,c) in the deep tropics. Suppressed (enhanced) precipitation and moisture divergence (convergence) balance each other. At day -15, the negative precipitation anomalies along the near-equatorial Indian Ocean and southern parts of the Indian peninsula are accompanied by moisture divergence. As time processes, the moisture divergence moves northward and intensifies, and covers the northern Arabian Sea, central India and the central Bay of Bengal at -5 days. At this pentad, reduced evaporation over the Arabian Sea and the Bay of Bengal contributes in addition to the moisture divergence to the reduced precipitation in these areas. (Fig. 5.11 c). As expected, negative precipitation anomalies and moisture divergence peak simultaneously together over central India at day 0 (Fig. 5.13 a). Quantitatively, over central India moisture divergence accounts for about 65.5 % of the negative rainfall anomalies at day 0 (Tab. 5.2). The contributions from moisture advection and evaporation are approximately -20.5 % and 1.8 %, respectively. Nevertheless, of major importance is the role of anomalous dry advection of moisture over central India before the onset of breaks. Consistent with the study of Prasanna and Annamalai (2012) based on the ERA Interim reanalysis data, drier air advection leads both moisture divergence and negative rainfall anomalies by about 5 days over central India (Fig. 5.13 a). During the initiation of breaks, dry advection dominates the northern Arabian Sea and intensifies from days -20 to days -10 (Fig. 5.11 b). At day -5, dry air advection covers the whole northern part of the Indian peninsula with adjacent seas. With the onset of breaks, moist advection starts to dominate the northern Arabian Sea.

Su and Neelin (2002) emphasised that the seeming balance between precipitation anomalies and moisture divergence mask the importance of other moist processes (e.g. moisture advection and evaporation). They noted that moisture convergence is a ”feedback” rather than a ”cause” in the chain of convective response to warm SST forcing. Therefore, they recommended the MSE equation as a better approach to analyse the role of other physical processes in the moist dynamics of the deep tropics because of the cancellation of moisture convergence and adiabatic cooling associated with rising motions. Additionally to the moisture budget the MSE budget combines physical processes affecting temperature and moisture (Annamalai, 2010; Prasanna and Annamalai, 2012; Su and Neelin, 2002).

Moist static energy budget

The six terms of the MSE budget are the anomalous MSE convergence ($\widehat{\omega\partial_p h}^{'}$), horizontal temperature advection ($-\widehat{\mathbf{v}\cdot\boldsymbol{\nabla}T}^{'}$) (horizontal diffusion neglected), horizontal moisture advection ($-\widehat{\mathbf{v}\cdot\boldsymbol{\nabla}q}^{'}$) (horizontal diffusion neglected), net radiative flux ($F_{rad}{}^{'}$), surface sensible heat flux ($H^{'}$) and evaporation ($E^{'}$) (see section 4.2). Fig. 5.12 shows the space-time evolution (-20 days to +5 days) of vertically integrated anomalous MSE convergence

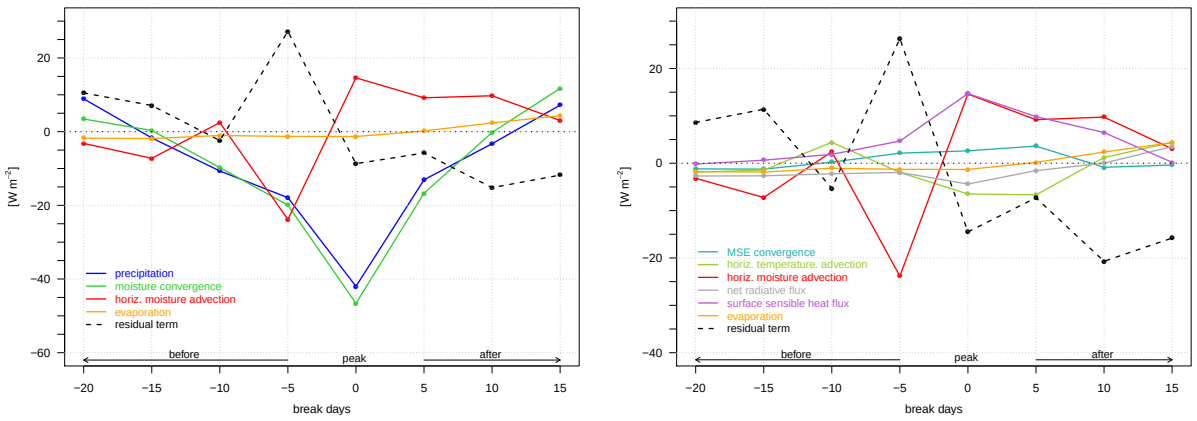

(a) moisture budget (b) moist static energy budget

Figure 5.13: Composite temporal evolution (pentads) of individual terms of the moisture budget (a) and of the moist static energy budget (b) averaged over central India (21°-27°N, 72°-85°E). The residuals are shown as black dashed lines. All units are in W m^{-2}. The time evolution is from left to right (-20 days to +15 days). The dotted black horizontal line marks the zero line.

or vertical advection of MSE (a), vertically integrated anomalous horizontal temperature advection (b), anomalous net radiative flux (c) and anomalous surface sensible heat flux (d), while anomalous horizontal moisture advection and anomalous evaporation are already shown in Fig. 5.11 (b,c). Positive (negative) values of MSE convergence mean energy import (export) in the column in Fig. 5.12 (a). A positive (negative) sign of net radiative flux represents radiative warming (cooling) in the column in Fig. 5.12 (c).

The MSE budget over central India (Fig. 5.13 b) reaffirms the dominant role of anomalous dry horizontal advection of moisture during the initiation of breaks. Drier air advection leads all the other terms of the MSE budget over the central India region and its contribution (−39.7 %) to the anomalous positive MSE convergence overtops the contributions by temperature advection (−3.2 %), net radiation (−3.2 %), and sensible heat (7.8 %) and evaporative (−2.2 %) fluxes at day -5. In accordance to Prasanna and Annamalai (2012), this suggests that dry advection acts as a precursor in the series of moist dynamical processes that induce a break monsoon situation over India. During break conditions, the positive MSE convergence follows inversely the negative precipitation anomaly and the moisture divergence (cp. Figs. 5.13 a,b) but with a time lag of around +5 days and a considerable reduced amplitude (by a factor of around 10). This import of low MSE, which means stable atmospheric conditions, may be caused by an advection of dry air into the region during the initiation phase of breaks. As noted by Sobel et al. (2001) and Prasanna and Annamalai (2012), the smallness of the Coriolis parameter near the equator leads to weak horizontal temperature gradients in the tropics. Therefore, the contribution from horizontal temperature advection to the MSE budget is rather small over central India. However, during the initiation of breaks, positive temperature advection is obvious over the northern part of the Arabian

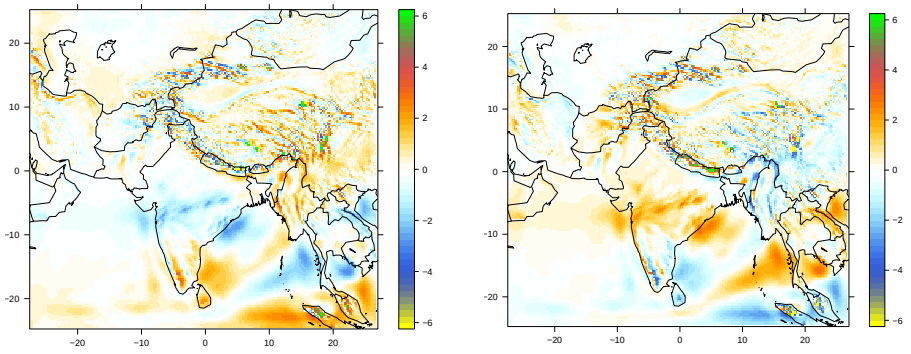

(a) diabatic heating (b) vertical temperature advection

Figure 5.14: Composite anomalies of terms of the thermodynamic-energy equation (equation 3 in Rodwell and Hoskins (1996)) calculated at 500 hPa from HH5-CTRL during day 0, defined as the peak phase of monsoon breaks and maximum amplitude of rainfall anomalies: diabatic heating $\frac{Q_\mathrm{d}}{c_\mathrm{pd}}$ [K day^{-1}] (a) and vertical temperature advection $-(\frac{p}{p_0})^{R_\mathrm{d}/c_\mathrm{pd}}\,\omega\,\frac{\partial\theta}{\partial p}$ [K day^{-1}] (b).

Sea with maximum at -10 days. This warm air advection coincides with the dry advection over the northern Arabian Sea (cp. Figs. 5.11 b and 5.12 b) and suggests the intrusion of warm dry air. Desert air incursions arriving over the Arabian Sea and central India from western Asia just before the onset of dry spells found by Krishnamurti et al. (2010) by calculating back-trajectories based on NCEP-NCAR reanalysis data could explain this detected warm dry advection. However, after the onset of breaks cold air advection occurring over central India (Fig. 5.13 b) could be a relevant process in maintaining dry conditions over India. The surface sensible heat flux increases from -5 days onward (Fig. 5.12 d) due to the lack of rainfall (Fig. 5.10 a) and suppressed convection (not shown) over India. The anomalous net radiative flux pattern (Fig. 5.12 c), mainly characterised by the OLR pattern (not shown) implies a net radiative cooling in the atmospheric column over regions with negative rainfall anomalies (Fig. 5.10 a). From a thermodynamic point, if the tropical atmosphere experience diabatic heating or cooling the pressure (mass) and wind fields will undergo an adjustment process (Hoskins and Wang, 2006). Hence, the net radiative cooling will be balanced by adiabatic warming due to descending air. Fig. 5.14 shows day 0 composite anomalies of terms of the thermodynamic energy equation

$$\frac{Q_\mathrm{d}}{c_\mathrm{pd}} = \mathbf{v}\cdot\boldsymbol{\nabla}_\mathrm{p}T \;-\; \left(\frac{p}{p_0}\right)^{\frac{R_\mathrm{d}}{c_\mathrm{pd}}}\omega\,\frac{\partial\theta}{\partial p} \qquad \text{(equation 3 in Rodwell and Hoskins (1996))},$$

namely the diabatic heating $\frac{Q_\mathrm{d}}{c_\mathrm{pd}}$ (a) and the vertical temperature advection $-(\frac{p}{p_0})^{\frac{R_\mathrm{d}}{c_\mathrm{pd}}}\,\omega\,\frac{\partial\theta}{\partial p}$ (b) at 500 hPa. The thermodynamic budget suggests that the reduced latent heat release due to suppressed convection is balanced almost entirely by adiabatic warming due to descent over central India and adjacent areas of the Arabian Sea and the Bay of Bengal during

breaks (cp. Figs. 5.14 a,b). This is consistent with the assumption by Rodwell and Hoskins (1996) that horizontal temperature advection is negligible in equatorial regions and hence the balance is between adiabatic warming and cooling associated with vertical motion, and diabatic heating.
According to the results of earlier MSE budget studies (e.g. Kiranmayi and Maloney, 2011; Prasanna and Annamalai, 2012), a residual term exists in the anomalous MSE budget (Fig. 5.13 b). The residual appears to be of the same order as the moisture advection and in opposite phase with it. It should be noted, that the present analysis bases on model data, which were interpolated from native model coordinates to standard pressure levels. This can contribute to residuals (Prasanna and Annamalai, 2012) and may lead to misrepresentation of MSE import/export processes during monsoon breaks. Kiranmayi and Maloney (2011) found residuals also in MSE budgets by using reanalysis products. They suggested that the residual term appears to be a result of missing or miscalculated MSE sources in the data sets. The use of standard output variables instead of advective terms output directly from the model dynamical core could introduce a residual of uncertain sign (Kiranmayi and Maloney, 2011). Residuals in this study can also result from neglecting horizontal diffusion in the horizontal advection terms $\widehat{D_T T}'$ and $\widehat{D_q q}'$ in Eqs. (4.8) and (4.9). Overall, this residual term raises a caveat on the presented MSE budget study.

Vertical structure

In the mean, during the summer monsoon season central India is an area of absolute ascending motion, as shown in Fig. 5.3 (section 5.1). However, during a break-monsoon this region experiences a radical change in the regime of rainfall, which implies a significant alteration in the vertical circulation (Raghavan, 1973).
A time sequence of latitude-height cross-sections of composite anomalous vertical pressure velocity averaged along the longitudinal sector of the whole model domain (Fig. 5.15 b) reveal the formation of an anomalous local Hadley circulation with rising over the equatorial Indian Ocean and sinking over central India and adjoining seas (cp. Figs. 5.15 b,c) during the development phase of breaks consistent with earlier studies (e.g. Prasanna and Annamalai, 2012; Rao et al., 2004). Likewise, Raghavan (1973) depicted in a schematic model of the vertical circulation a displacement of the anti-Hadley (monsoon) cell to the north and the development of a Hadley cell in the south with a common descending limb over central India during the transition from a normal monsoon to a break-monsoon. From -5 days to day 0, a strengthening of the rising limb over the near-equatorial belt can be associated with an intensification of precipitation (positive rainfall anomalies) (Fig. 5.10 a) and moisture convergence (Fig. 5.11 a) over this region. At the same pentads, the descending limb moves northward induced by the propagation of negative rainfall anomalies from the oceanic to the

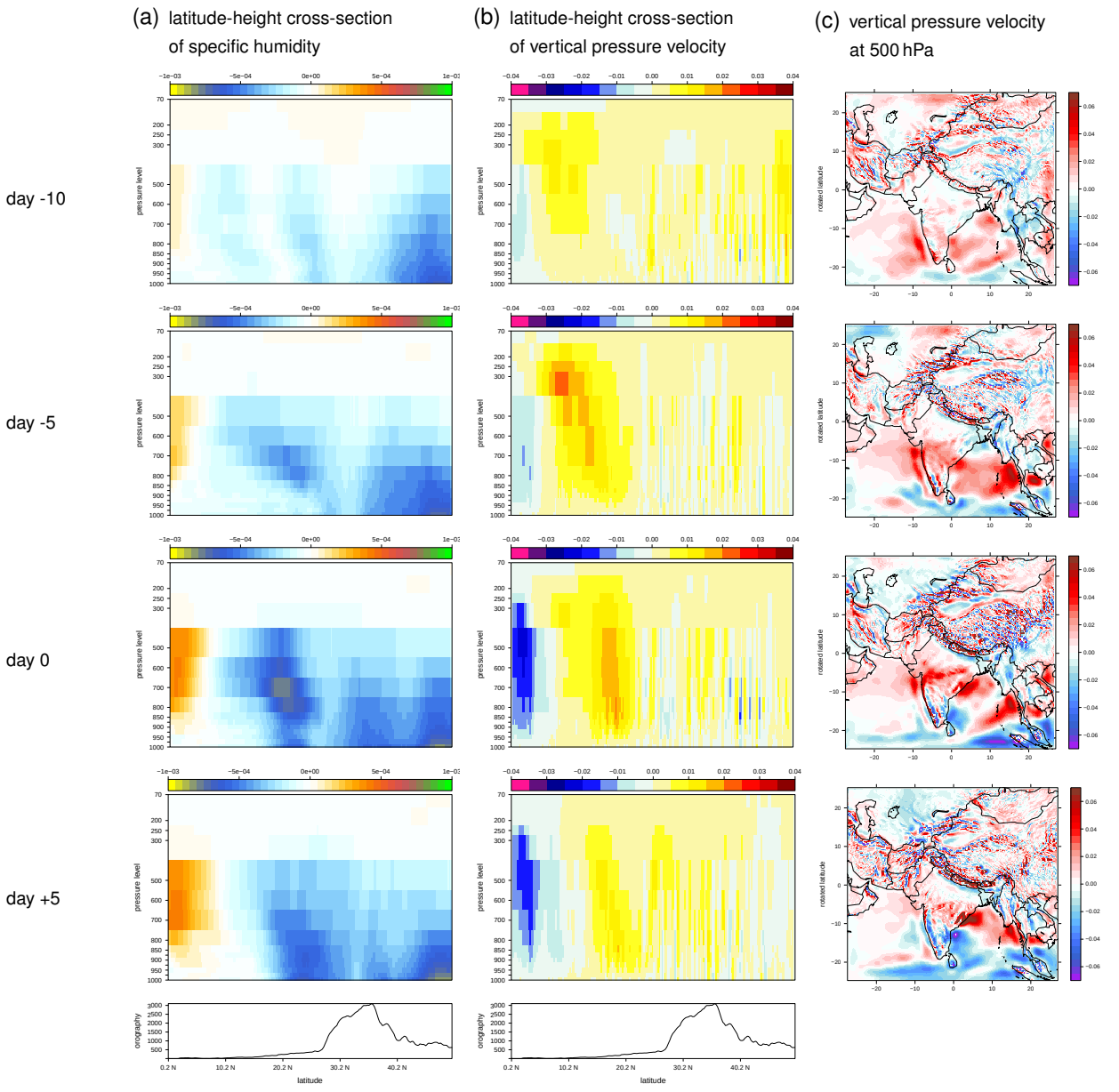

Figure 5.15: Space-time evolution of composite anomalies for the cross-section of specific humidity [kg kg^{-1}] (a) and vertical pressure velocity [Pa s^{-1}] (b) along the longitudinal sector of the whole model domain, and the vertical pressure velocity at 500 hPa [Pa s^{-1}] (c). Positive (negative) values of vertical pressure velocity mean descending (ascending) air. The bottom panel in (a,b) shows the cross-section of the model orography [m] for the same longitudinal sector. The composites are shown from days -10 to days +5 (pentads) with day 0 defined as the peak phase of monsoon breaks and maximum amplitude of rainfall anomalies. Each panel is 5 days apart.

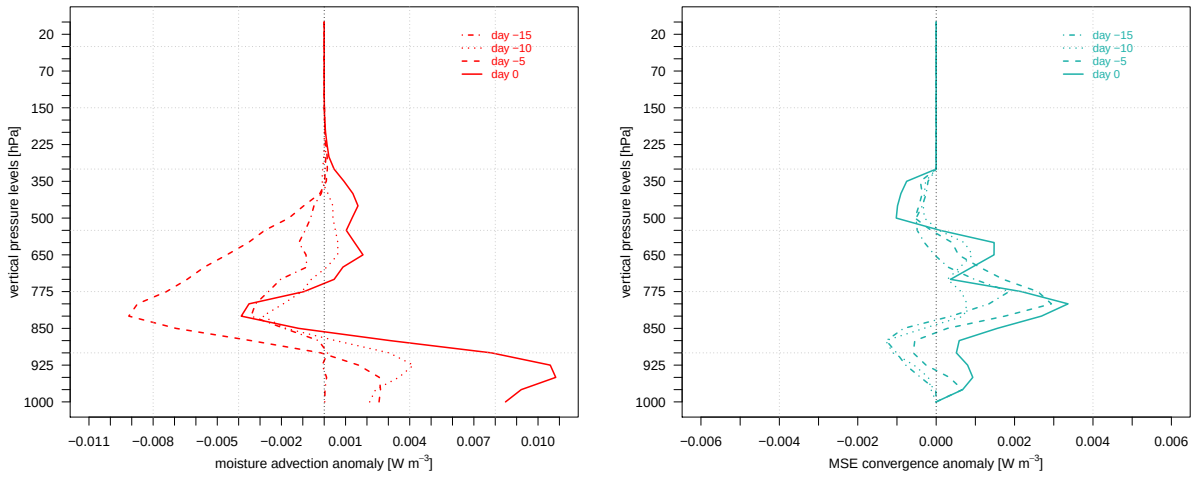

(a) horizontal moisture advection

(b) MSE convergence

Figure 5.16: Vertical distribution of composite horizontal moisture advection (a) and MSE convergence (b) averaged over central India (21°-27°N, 72°-85°E). All units are in W m^{-3}. Composites are shown from -15 days to 0 days (pentads). The dotted black vertical line marks the zero line.

continental maximum cloud zone (Sikka and Gadgil, 1980). Moreover, Fig. 5.15 (b) indicates that the strong descending motion begins in the higher troposphere at around 300 hPa, moves downward as time progresses, and reaches the lower troposphere (800–850 hPa) at day 0. The latitude-height cross sections of composite anomalous specific humidity reveal that this sinking over central India is accompanied by a relative drying of the middle and lower troposphere with the maximum at around 700–800 hPa at day 0 (Fig. 5.15 a). The depletion of low-level moisture is in agreement with the adiabatic warming of the descending air.

MSE budget studies of Maloney (2009) and Kiranmayi and Maloney (2011) showed a buildup of column-integrated MSE in advance of convective precipitation events associated with the eastward moving 30-60 day Madden-Julian oscillation (MJO) over the Indian and west Pacific Oceans. Furthermore, the results of Kemball-Cook and Weare (2001) suggested that the initiation of MJO convection is controlled by a destabilisation of the atmosphere through a combination of low-level MSE buildup and simultaneous depression of mid-tropospheric MSE. In contrast to that, prior to the onset of breaks a MSE import (export) can be found at the middle (lower) troposphere over the central India region (Fig. 5.16 b). This vertical gradient in MSE convergence indicates enhanced atmospheric stability in mid- to low-tropospheric levels and implies conditions of suppressed convective activity over this region. At day 0, the entire middle and lower troposphere experience a MSE import. Compared to Prasanna and Annamalai (2012), the MSE convergence anomalies constructed from HIRHAM5 are weak and equal to zero in the upper atmosphere (Fig. 5.16 b) and therefore the vertically integrated MSE convergence is weaker in amplitude (see Fig. 5.12 a and Fig. 5.13 b). The cause for this difference is the limitation of the vertical velocity calculation within HIRHAM5

based on the hydrostatic approximation.
As demonstrated by Maloney (2009), MSE anomalies are almost entirely regulated by water vapour in the lower troposphere during MJO-related precipitation events in the deep tropics. The vertical structure of anomalous horizontal moisture advection averaged over central India (Fig. 5.16 a, will be discussed in the next section) suggests this dominant role of specific humidity anomalies in determining middle to lower troposphere MSE anomalies.

Origin of the dry air advection

The column-integrated moisture and MSE budget studies have identified the leading role of anomalous dry horizontal advection of moisture over India during the initiation of monsoon breaks. Now an investigation of its vertical structure and horizontal wind fields in different vertical levels should help to explain the origin of the dry air advection.
The vertical distribution of composite horizontal moisture advection in Fig. 5.16 (a) reveals the 'level of maximum injection' (Prasanna and Annamalai, 2012) at around 800–825 hPa. This coincides with the results from the model diagnostics in Prasanna and Annamalai (2012). Compared to the ERA Interim reanalysis diagnostics (peak at 650–700 hPa), the model data detect the peak at lower atmospheric levels. Moreover, Fig. 5.16 (a) shows that the anomalous dryness covers the whole middle and lower troposphere, except for the near-surface layers (lower than 900 hPa) where anomalous moisture advection can be noted since day -10. With the onset of breaks, the advection of drier air decreases in intensity, while the moisture advection strengthens at around 950 hPa. This vertical gradient of anomalous moisture advection in the troposphere over India during the initiation of breaks corresponds to the findings of Krishnamurti et al. (2010). They showed that back-trajectories calculated from NCEP-NCAR reanalysis data terminating between 700 hPa to 400 hPa over central India had their origin over western Asian desert regions, whereas those arriving in the lowest kilometres (at around 850 hPa) were of oceanic origin during dry spells. HIRHAM5 seems to reproduce this predominating dry air advection lying on top of the transport of moist oceanic air over the central India region (Fig. 5.16 a). Krishnamurti et al. (2010) emphasised the formation of a blocking high over western Asia extending from 700 hPa to 300 hPa as a persistent feature for dry spells. Descending air circulations around this high cause the advection of upper tropospheric dry air to the Arabian Sea and central India (Krishnamurti et al., 2010). Likewise, a back-trajectory analysis of Bhat (2006) based on ERA 40 reanalysis data revealed advection of dry air from over the deserts at 800 hPa over the eastern Arabian Sea during the major Indian drought in the year of 2002 in contrast to marine air from southern Indian Ocean in a normal monsoon year. Composite anomalies of 800 hPa wind (around the "level of maximum injection" in HIRHAM5) at day -10 (Fig. 5.17 a) suggest the presence of north-westerly wind anomalies over Iran and western Pakistan,

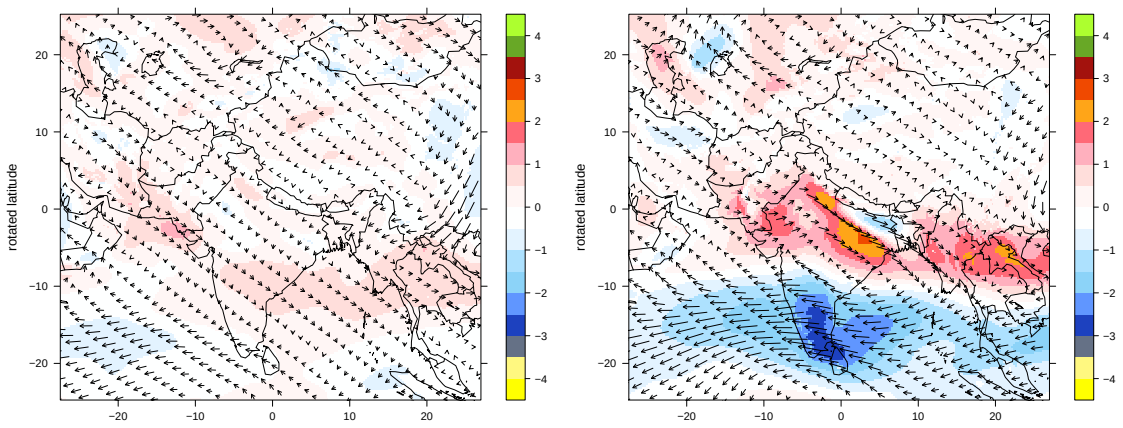

(a) day -10 (b) day -5

Figure 5.17: Composite anomalies of 800 hPa wind [$m\,s^{-1}$] at pentad day -10 (a) and pentad day -5 (b) from HH5-CTRL during breaks.

which could indicate a transport of drier air from western Asia to the northern Arabian Sea. This corresponds to the found dry advection strengthening over the northern part of the Arabian Sea at day -10 (cp. Figs. 5.11 b, 5.17 a). From day -10 to day -5, anomalous westerlies over western Pakistan and north-western India evolve (5.17 a,b). Such westerly wind anomalies could advect the dry air to central India (Fig. 5.11 b) and contribute to dry weather conditions over that part of India.

This is the first study applying moisture and MSE budget diagnostics following the method by Prasanna and Annamalai (2012) on the output of a regional climate model in order to investigate moist dynamical processes that initiate and maintain breaks during the SASM. Due to the benefit of a higher horizontal resolution compared to the model diagnostics of Prasanna and Annamalai (2012) the present research helps to improve the understanding of monsoon breaks. In summary, the budget analyses and time sequences of composite anomalies suggest the following mechanisms, which is also schematically illustrated in Fig. 8.1 in chapter 8.1. From 15 days to 10 days before the onset of monsoon breaks, anomalous dry advection intensifies over the northern Arabian Sea due to anomalous low-level northwesterlies over Iran and western Pakistan (Figs. 5.10 b and 5.17 a) carrying warm and dry air from western Asia (Figs. 5.11 b and 5.12 b). At day -5, with the transition to westerly wind anomalies in the lower troposphere over the plains of northern India (Fig. 5.17 b) the drier air advects to central India (Fig. 5.13 b). First, this dry advection contributes to the initiation of dry weather conditions over central India. Second, an anomalous anticyclonic low-level circulation over northern India, detected as a Rossby wave response by earlier studies (e.g. Annamalai and Slingo, 2001; Annamalai and Sperber, 2005; Krishnan et al., 2000;

Prasanna and Annamalai, 2012) to anomalous net heating over the near-equatorial Indian Ocean (Fig. 5.12 c), reduce the moisture transport into the monsoon region by anomalous easterlies over the Arabian Sea (Fig. 5.10 b). From -5 days onward, the lack of rainfall together with the increase in radiative cooling over parts of India is accompanied with enhanced precipitation and an increase in radiative warming along the near-equatorial Indian Ocean (cp. Figs. 5.10 a and 5.12 c). Since from a thermodynamic point radiative cooling is balanced by diabatic subsidence (Hoskins and Wang, 2006) the two out of phase heat regions are connected by a thermally driven meridional circulation. With the initiation of breaks an anomalous local Hadley cell with rising over the equatorial Indian Ocean and sinking over central India and adjoining seas is apparent (Fig. 5.15 b). The anomalous descent over central India is in turn associated with adiabatic warming and forces a vertical gradient in MSE convergence over this region (Fig. 5.16 b), which implies enhanced atmospheric stability and hence conditions of suppressed convective activity. Third, this feature of a local anomalous Hadley circulation plays an important role in maintaining break conditions over central India. Fourth, a cyclonic response to the positive precipitation anomalies over the near-equatorial Indian Ocean strengthens the anomalous low-level easterlies over southern India and the Arabian Sea and contributes further to a divergent flow over central India (cp. Fig. 5.10 b and Fig. 5.11 a).

In summary, the present study confirms that (i) dry air advection from western Asia is the dominant moist process which initiate monsoon breaks, (ii) regional circulation features forced by suppressed/enhanced rainfall anomalies trigger the break-monsoon conditions and (iii) an anomalous Hadley cell with descent motion over central India contributes to suppressed convective activity over that part of India.

6 Model tuning

The regional atmospheric climate model HIRHAM5, combining the dynamics of the HIRLAM7 model as a numerical short-range weather forecasting system developed for the midlatitude's atmospheric dynamics and the physical parameterisation schemes of the general atmospheric circulation model ECHAM5, is well adjusted for the arctic climate (e.g. Klaus, 2014). Although a regional model can be used around the globe, South Asia including the Himalayas remains an alien region for HIRHAM5, because its parameterisations, especially the convection scheme are not adapted to the tropical climate (Lucas-Picher et al., 2011). Rockel and Geyer (2008) examined the transferability of the regional climate model CLM to different climate zones of the earth. Their study reveals that the quality of the simulations for temperate and continental climates was similar to those over Europe. However, they found systematic overestimations of precipitation over warm oceans and underestimations over land for tropical climates, emphasising the important role of the applied convective schemes. Moreover, they detected a positive bias in precipitation occurring over high and narrow mountain ranges which stand perpendicular to the main wind systems in all analysed regions. Rockel and Geyer (2008) confirmed that in order to get optimal simulation results, one standard model setup is not applicable for all climate zones. Likewise, Mauritsen (2012) stressed in their study the need of model tuning as an integral part of model development in order to adjust uncertain or even non-observable parameters related to processes not explicitly resolved at the model grid resolution. Moreover, Giorgetta et al. (2013) pointed out that the new ECHAM version still contains several poorly constrained parameters related for example to clouds and convection processes, which are adjusted to yield an acceptable climate and a sufficiently stable model execution. Some of these parameters are dependent on the horizontal and vertical model resolution. Hence, these parameters have to adapt for a change in the model resolution from the global to the regional scale.

Based on the deficiencies of the HIRHAM5 control run in reproducing the monsoon climate, demonstrated in chapter 5.1, sensitivity experiments were conducted to assess the effect of modifying tuning parameters in atmospheric and soil moisture processes on the simulation of the Indian summer monsoon precipitation. An overview of the modified model parameter and the adapted model setup is given in section 6.1 and 6.2, respectively. Finally, a brief

evaluation of the sensitivity experiments is presented in section 6.3.

6.1 Tuning parameter

Sensitivity studies are performed to identify suitable tuning parameter which are able to reduce the systematic land-sea contrast of the precipitation bias during the summer monsoon season. Based on the results of the validation of the HH5-CTRL run showing deficiencies in the simulation of the convective precipitation and evaporation (cp. chapter 5.1), tuning parameters that controls convective cloud and soil moisture processes (illustrated in Fig. 6.1) are selected. An overview of the parameters tuned in this study, which are described in detail in chapter 2, is given in Tab. 6.1. The objective of the sensitivity studies is to find a tuned model setup, that yields a better simulation of the Indian summer monsoon rainfall and can be used for further model experiments (see chapter 7).

Parameter	**Meaning**	**Default**	**Tuning value**	**Sensitivity run**
k_{conv}	coefficient that determines the conversion rate of cloud water to rain (snow) in convective clouds	$1 \times 10^{-4}\,\mathrm{m}^{-1}$	$2 \times 10^{-4}\,\mathrm{m}^{-1}$	HH5-S1
τ	specified time scale in which the penetrative convection acts to reduce $CAPE$ towards zero	$\approx$ 47.5 min (with $nn = 159$)	$\approx$ 24 min (with $nn = 319$)	HH5-S2
σ_0	minimum threshold value of the terrain steepness, which controls the efficiency of the surface runoff for flat terrain	100 m	200 m ; 500 m	HH5-S3 ; HH5-S4
σ_{max}	maximum threshold value of the terrain steepness, which controls the efficiency of the surface runoff for steep terrain	400 m (with $ngl = 160$)	$\approx$ 200 m (with $ngl = 319$)	HH5-S5
d	constant that determines the efficiency of the fast drainage	1.5	3.0 ; 7.5	HH5-S6 ; HH5-S7

Table 6.1: Notation, description, default values and tuned values of modified model tuning parameters described in detail in chapter 2. The notation conforms to the ECHAM documentation (Roeckner et al., 1992, 2003), with the exception of k_{conv} (see chapter 2 for details). Here, nn is defined as the spectral resolution of the ECHAM model and ngl is the number of latitudes referring to the atmospheric grid.

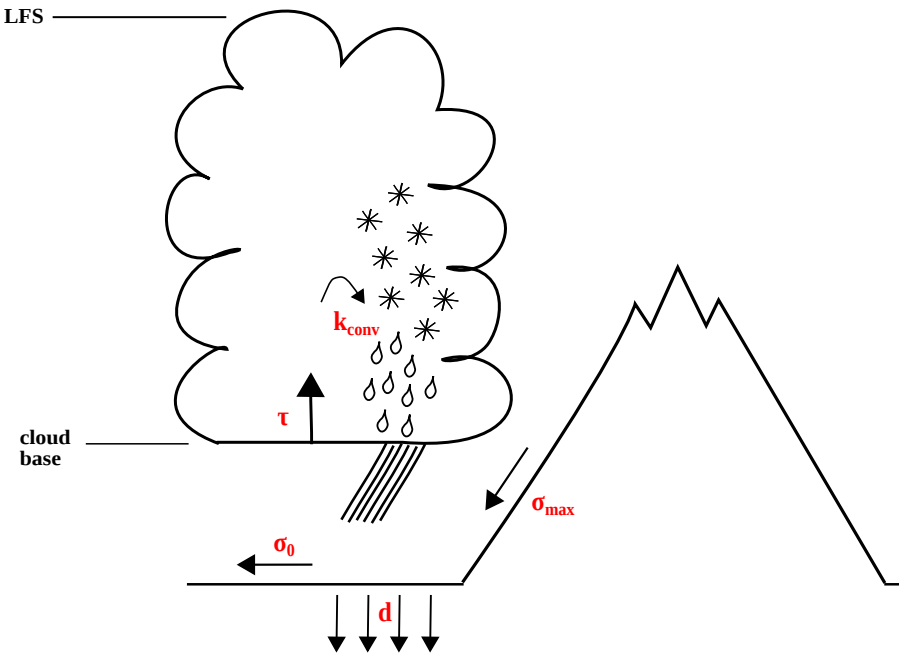

Figure 6.1: Illustration of the tuned convective cloud and soil moisture processes in HIRHAM5. LFS is the level of free sinking. Parameters are: (k_{conv}) coefficient that determines the convective cloud water conversion rate to rain (snow), (τ) time scale in which penetrative convection acts to reduce $CAPE$ to zero, (σ_0) minimum threshold value of the terrain steepness controlling the efficiency of the surface runoff for flat terrain, (σ_{max}) maximum threshold value of the terrain steepness controlling the efficiency of the surface runoff for steep terrain, and (d) constant that determines the efficiency of the fast drainage.

6.2 Model setup

For reasons of model stability, the configuration setup used for the HH5-CTRL was modified for the sensitivity studies. Following the stratiform cloud parameterisation in ECHAM6 (Giorgetta et al., 2013), the simulations were carried out with the diagnostic cloud cover scheme by Sundqvist et al. (1989) instead of the statistical cloud cover scheme by Tompkins (2002) used in ECHAM5. Due to the more stable model execution by using the diagnostic scheme, the adapted horizontal diffusion coefficient K_6 has been reset to the value as described in the standard configuration setup (cp. section 2.1.1.2). The model was applied with this new setup (HH5-S) representing the control condition for the sensitivity studies. Based on the run HH5-S, seven sensitivity runs are performed (HH5-S1 - 7), where always one tuning parameter is modified (see Tab. 6.1). In conclusion, a final run was carried out (HH5-FINAL), combining all modified tuning parameters that lead to a better representation of the summer monsoon rainfall. All experiments were realised for 9 months of the year 1979 (first year of HH5-CTRL), starting from 1 January to 30 September.

6.3 Evaluation

Clouds have a significant influence on the hydrological and thermodynamic budgets. Therefore, the inclusion of cloud processes in climate and forecasts models is an important task (Tompkins, 2002). There are many cloud schemes of different complexity, which parameterise cloud processes that cannot be resolved at the current model resolutions. Fractional cloudiness in a grid cell is the result of subgrid-scale variability of water vapor (Tompkins, 2002). In the statistical cloud cover scheme by Tompkins (2002) the subgrid-scale variability is specified by a PDF for the total atmospheric water content in terms of a beta distribution (see section 2.1.2.2 for details). If the statistical moments of the PDF are known, the fractional cloud cover can be calculated as the integral over the supersaturated part of the PDF. However, in the more simple diagnostic cloud cover scheme by Sundqvist et al. (1989) the onset of cloud formation is controlled by the grid-cell mean relative humidity and a height depending condensation threshold. Here, the critical relative humidity provides the subgrid-scale variability of cloud cover.

Fig. 6.2 shows a comparison of JJAS mean distributions of selected fundamental atmospheric and hydrologic model variables for the year 1979 between the control run using the statistical scheme (HH5-CTRL) and the sensitivity experiment using the diagnostic scheme (HH5-S). The diagnostic scheme by Sundqvist et al. (1989), produces more large-scale precipitation over Southeast Asia, central China and also over central and northern India compared to the statistical scheme by Tompkins (2002) (Figs. 6.2 d,e). Moreover, improvements in convective precipitation can be seen all over the domain, with increased rainfall over the Indian subcontinent and decreased rainfall over the warm Indian Ocean regions resulting in a reduced land-sea contrast bias by using the diagnostic scheme (Figs. 6.2 a,b). The larger convective and large-scale precipitation amounts over India simulated by the diagnostic scheme lead to a higher All-India Monsoon Rainfall (AIMR) index (Figs. 6.3, 6.4). This increase of the AIMR index of around 5.1 % in HH5-S compared to HH5-CTRL contributes to a better match of the ERA Interim reanalysis indicated by a smaller mean JJAS total precipitation bias (Fig. 6.5). Furthermore, when the diagnostic scheme is applied, a better representation of the hydrological cycle is yielded. The higher precipitation amounts lead to an increase of the soil water content (Figs. 6.2 m,n) causing more surface runoff (Figs. 6.2 p,q) and drainage (Figs. 6.2 s,t). The excess water will be lost from the model, as in HIRHAM5 the runoff and drainage generated in each time step will be removed from the simulated soil water reservoir (see section 2.1.2.5 for details). By evaporation, which is related to the soil moisture, the water can return to the atmosphere. The higher evaporation rate together with the wetter soil conditions in turn cause a reduce of the 2m-temperature bias especially over the Northern Indo-Gangetic Plain (not shown).

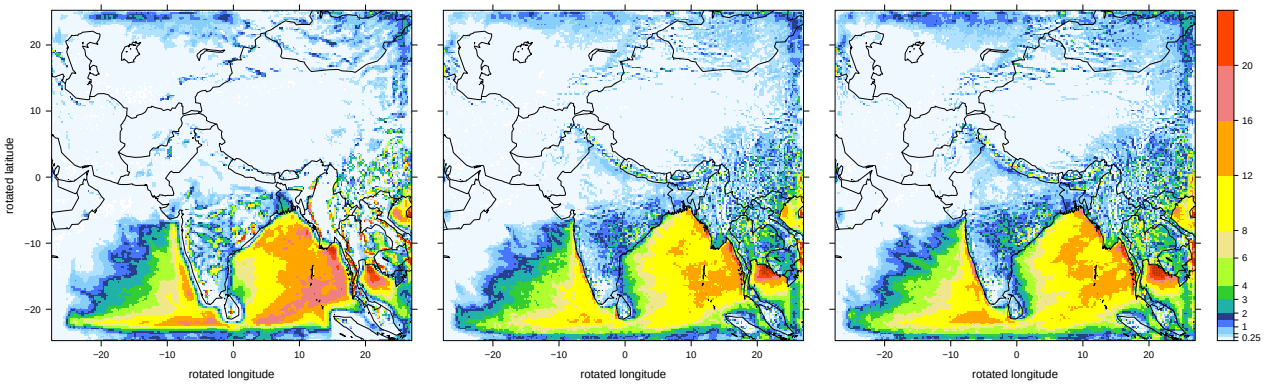

(a) HH5-CTRL aprc (b) HH5-S aprc (c) HH5-FINAL aprc

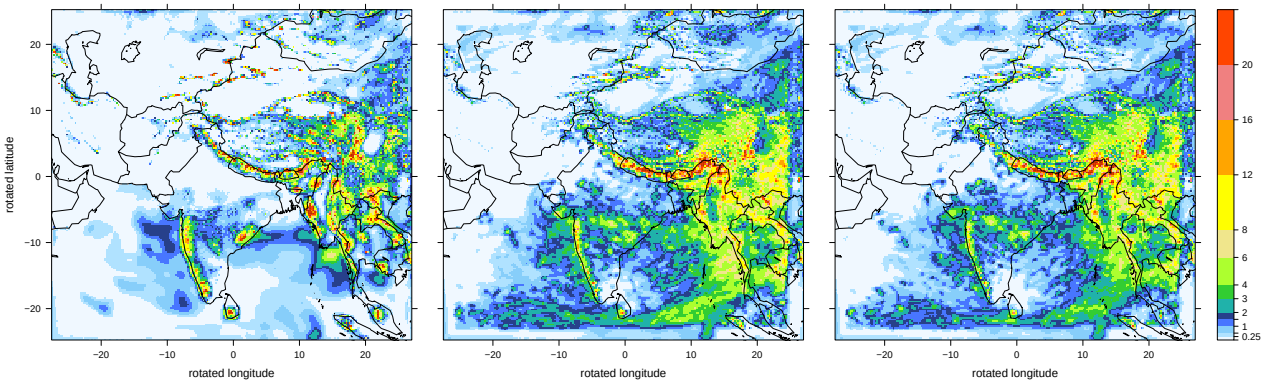

(d) HH5-CTRL aprl (e) HH5-S aprl (f) HH5-FINAL aprl

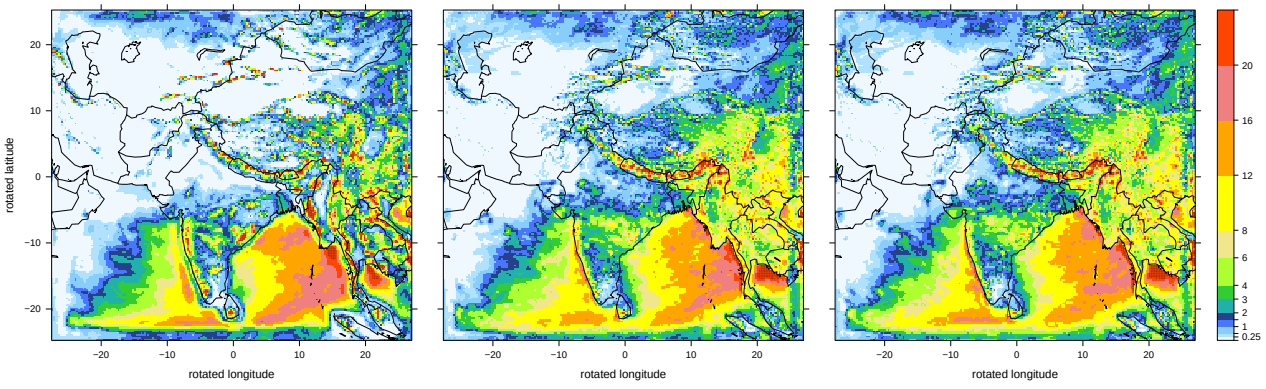

(g) HH5-CTRL precip (h) HH5-S precip (i) HH5-FINAL precip

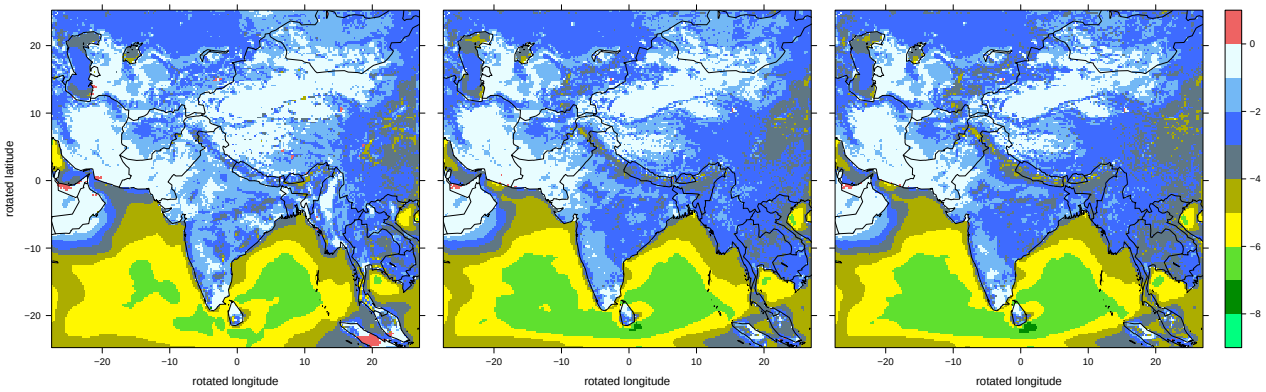

(j) HH5-CTRL evap (k) HH5-S evap (l) HH5-FINAL evap

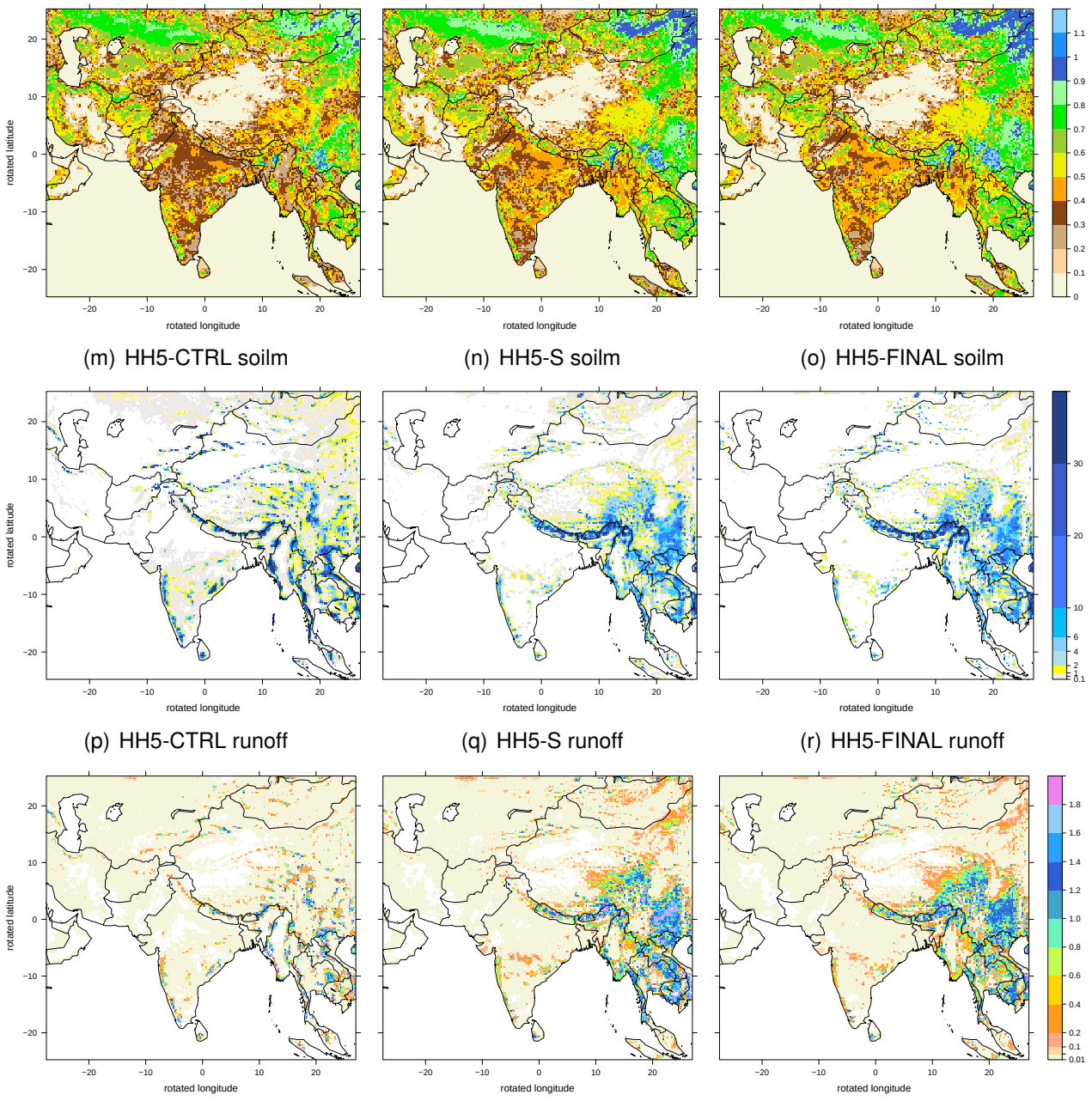

(m) HH5-CTRL soilm (n) HH5-S soilm (o) HH5-FINAL soilm

(p) HH5-CTRL runoff (q) HH5-S runoff (r) HH5-FINAL runoff

(s) HH5-CTRL drainage (t) HH5-S drainage (u) HH5-FINAL drainage

Figure 6.2: JJAS 1979 season means of HH5-CTRL, HH5-S and HH5-FINAL for convective precipitation [mm day^{-1}] (a,b,c), large-scale precipitation [mm day^{-1}] (d,e,f), total precipitation [mm day^{-1}] (g,h,i), evaporation [mm day^{-1}] (j,k,l), soil moisture [mm day^{-1}] (m,n,o), surface runoff [mm day^{-1}] (p,q,r) and drainage [mm day^{-1}] (s,t,u). Note evaporation as an upward flux is negatively defined in the model.

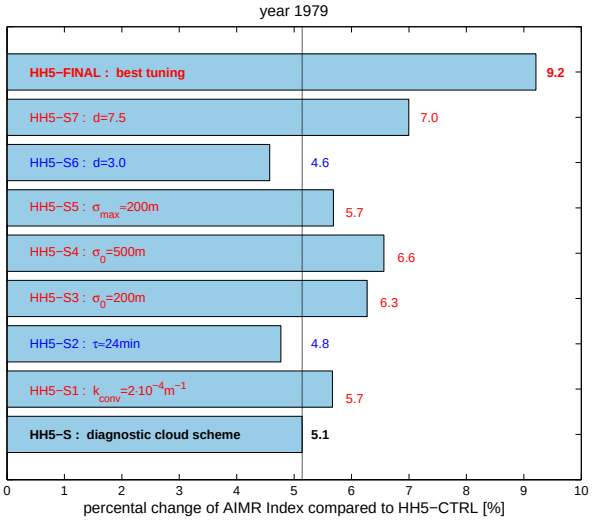

Figure 6.3: Percental change of the AIMR index [%] for the different sensitivity runs (HH5-S, HH5-S1-7 and HH5-FINAL) compared to that of the HH5-CTRL for the year 1979. Red (blue) colours indicate an increase (decrease) of the percental change relative to the control condition for the sensitivity runs represented by HH5-S. The vertical line marks the increase only due to the use of the diagnostic cloud cover scheme in HH5-S.

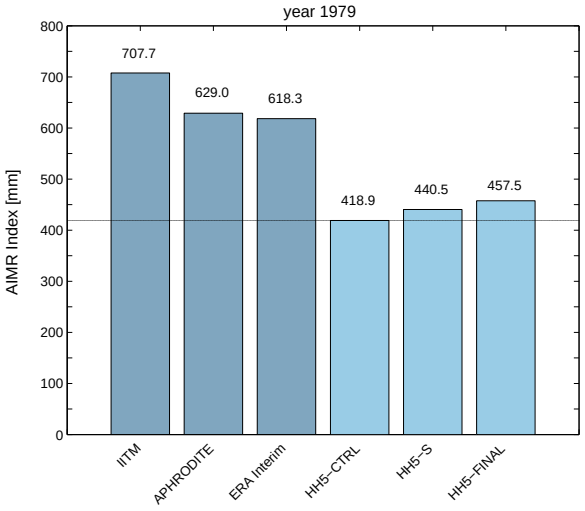

Figure 6.4: AIMR index [mm] of the year 1979 for the observationally based datasets IITM and APHRODITE, the reanalysis ERA Interim and the HIRHAM5 simulations HH5-CTRL, HH5-S and HH5-FINAL. The horizontal line marks the AIMR index of HH5-CTL.

The difficult task of statistical schemes is the specification of an appropriate PDF and the determination of the distribution moments (Tompkins, 2002). Therefore, an increase of the number of model tunable parameters, which are possibly not suitable for the monsoon climate, by using the more complex statistical scheme could be the cause of the fail of the statistical scheme in HIRHAM5 over the South Asia region. In conclusion, the simpler diagnostic scheme enables a stable model execution and leads to a more realistic representation of the summer monsoon precipitation distribution.

As introduced in section 2.1.2.1 the parameterisation of the convective precipitation formation in HIRHAM5 includes the adjustment parameter k_{conv}. This tunable parameter determines the conversion of cloud droplets to rain (snow) in convective systems. The larger the value of k_{conv}, the higher the conversion rate. This leads to more convective precipitation as more water is deposited directly from convective clouds to the surface. A doubling of the conversion rate in HH5-S1 leads to an increase of the AIMR index of around +0.6 % compared to the HH5-S run (cp. Tab. 6.1 and Fig. 6.3) and a considerable decrease of the mean precipitation bias (Fig. 6.5).

The adjustment closure by Nordeng (1994) for penetrative convection, which relates the cloud base mass flux to convective instability (see section 2.1.2.1, for details) uses a specified time

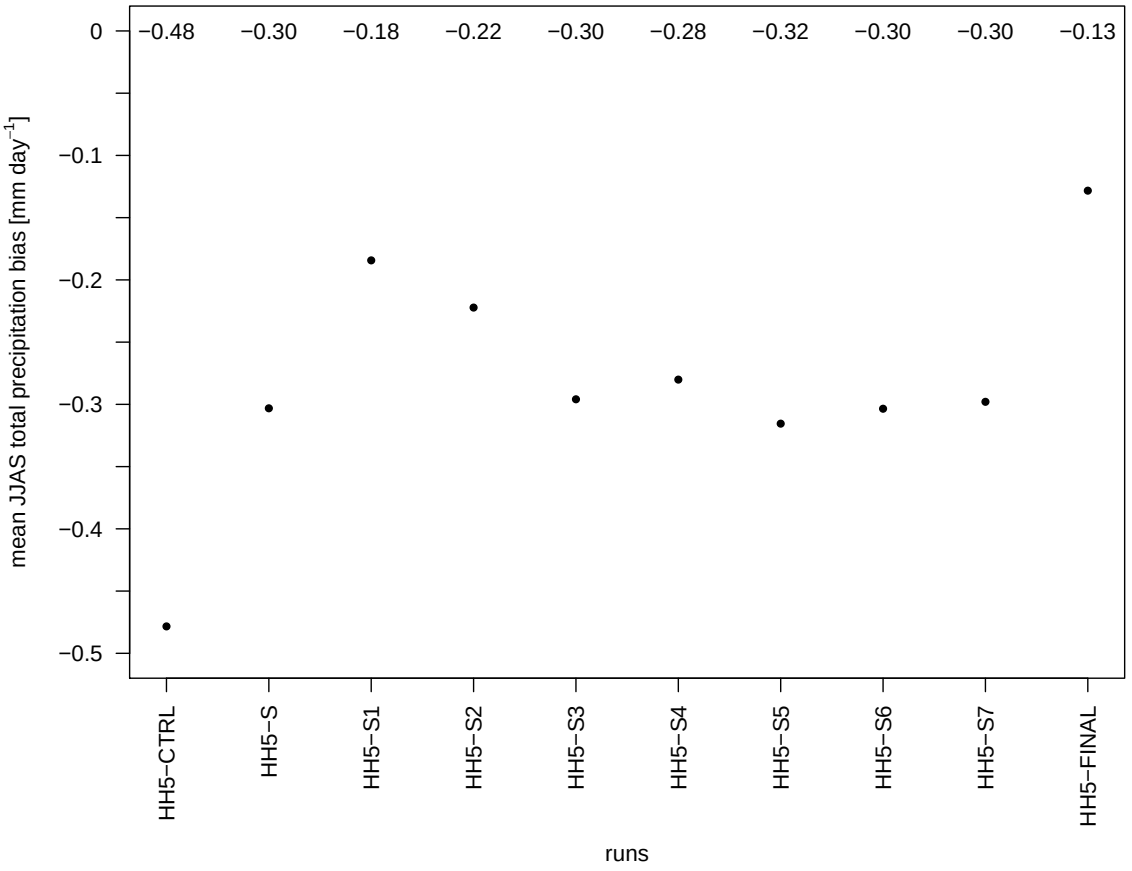

Figure 6.5: Mean summer monsoon (JJAS) total precipitation bias [mm day^{-1}] compared to ERA Interim (model minus ERA Interim) for the control run (HH5-CTRL) and different sensitivity experiments (HH5-S, HH5-S1-7 and HH5-FINAL) of the year 1979 averaged over the whole integration domain.

scale τ for which penetrative convection acts to remove convective instability. According to Nordeng (1994), this adjustable parameter τ depends on the horizontal grid resolution of the model and should be smaller (larger) with increasing (decreasing) resolution. Following that, τ was reduced to a value corresponding to a higher spectral resolution of $nn = 319$ (see Tab. 6.1). However, tuning this parameter to around half of the current value (HH5-S2) leads to a decrease of the AIMR index of around -0.3 % compared to the HH5-S run (Fig. 6.3) but with better match of the ERA Interim mean summer precipitation (Fig. 6.5).

Runoff and drainage are important processes in the hydrological cycle, which contribute to a reduction of the amount of soil water. Less soil infiltration leads to less moisture recycling by evaporation, which in turn inhibits the precipitation formation. A manipulation of the water for runoff shows an attempt to reduce the drying of the ground during the summer season found in the HIRHAM5 control run.

The parameterisation of the surface runoff in HIRHAM5 is related to a shape parameter b, which is a function of the steepness of the sub-grid scale terrain and two adjustable

threshold values (see section 2.1.2.5, for details). The minimum threshold value of the terrain steepness (σ_0), controls the efficiency of the surface runoff for flat terrain, whereas the maximum threshold value ($\sigma_{\max}$) controls the efficiency of the surface runoff for steep terrain. In relatively flat terrain, most of the precipitation can infiltrate the soil, while the runoff is extremely efficient in steep terrain. The value of σ_0 effects the terrain height, where the runoff starts to be efficiently. The larger the value of σ_0, the longer the runoff is reduced to a minimum in the transition from flat to steeper terrain and hence less water is lost from the model. The parameter σ_0 was increased to a value of $\sigma_0 = 200$ m (HH5-S3) and of $\sigma_0 = 500$ m (HH5-S4), respectively (see Tab. 6.1). Both sensitivity runs lead to an increase of the AIMR index, with the latter run (HH5-S4) resulting in the larger improvement of around +1.5 % compared to the HH5-S run (Fig. 6.3). The value of $\sigma_{\max}$, is defined indirectly proportional to the model horizontal resolution. Modifying this parameter to around half of the current value corresponding to a higher spectral resolution of $nn = 319$ (see Tab. 6.1) in HH5-S5 produces a change of the AIMR index of around +0.6 % compared to the HH5-S run (Fig. 6.3).
Both, slow and fast drainage are parameterised in terms of the soil water and storage capacity in HIRHAM5, while the efficiency of the fast drainage is additionally dependent on the adjustment parameter d (see section 2.1.2.5, for details). In two experiments, the value of d was increased to $d = 3.0$ (HH5-S6) and $d = 7.5$ (HH5-S7), respectively (cp. Tab. 6.1). The doubling of the constant leads to a reduce of the AIMR index of around -0.5 % compared to the HH5-S run, while the further increase of d results in a positive change of the index (+1.9 %) (Fig. 6.3).

In conclusion, a final sensitivity run (HH5-FINAL) was carried out combining all modified tuning parameters that lead to a better representation of the AIMR index (cp. Fig. 6.3). Following that, the final parameter settings are: $k_{\text{conv}} = 2 \times 10^{-4}\,\text{m}^{-1}$, $\sigma_0 = 500$ m, $\sigma_{\max} \approx 200$ m and $d = 7.5$. In the HH5-FINAL experiment, this combination of the adjustable parameters leads to the largest increase of the AIMR index among all sensitivity runs of around +4.1 % compared to the HH5-S run (Fig. 6.3). Moreover, this final tuning setup results in the best fit match of ERA Interim, and the mean JJAS total precipitation bias of the year 1979 between HH5-FINAL and ERA Interim is reduced to around -0.13 mm day^{-1} compared to the bias between HH5-CTRL and ERA Interim of around -0.48 mm day^{-1} (Fig. 6.5).

Overall, the model tuning could enhance the simulation of the mean Indian summer monsoon precipitation distribution with higher rainfall amounts over India. The largest improvement was achieved by using the diagnostic cloud cover scheme of Sundqvist et al. (1989) instead of the statistical cloud cover scheme of Tompkins (2002). However, compared to observationally based data sets and reanalysis data HIRHAM5 still shows a systematic underestimation of the summer monsoon rainfall amounts. The calculated HH5-FINAL AIMR index of the year

1979 is ~64.6 % of the IITM, ~72.7 % of the APHRODITE and ~74.0 % of the ERA Interim AIMR value, respectively (cp. Fig. 6.4) revealing the insufficient precipitation simulation in HIRHAM5 over South Asia including the Himalayas.

7 Sensitivity experiment: Increase of cloud droplet number concentration

It is a fact that atmospheric aerosols, whether from natural or anthropogenic sources, change cloud properties and thus contribute indirectly a substantial forcing to the climate system (Boucher et al., 2013). All clouds droplets must form on preexisting aerosol particles, which serve as cloud condensation nuclei (Rosenfeld et al., 2008). Thus, the amount of atmospheric aerosols plays a key role in cloud formation processes and hence in the initiation of precipitation. Increased aerosol concentrations modify the composition of clouds by providing more cloud condensation nuclei (Rosenfeld et al., 2008). In the past few decades, because of the increase of human activities the South Asia region has become a major source of aerosol emissions, most visible as the well-known Indo-Asian haze (e.g. Liu et al., 2011; Ramanathan et al., 2001; Ramanathan et al., 2005). Rosenfeld et al.

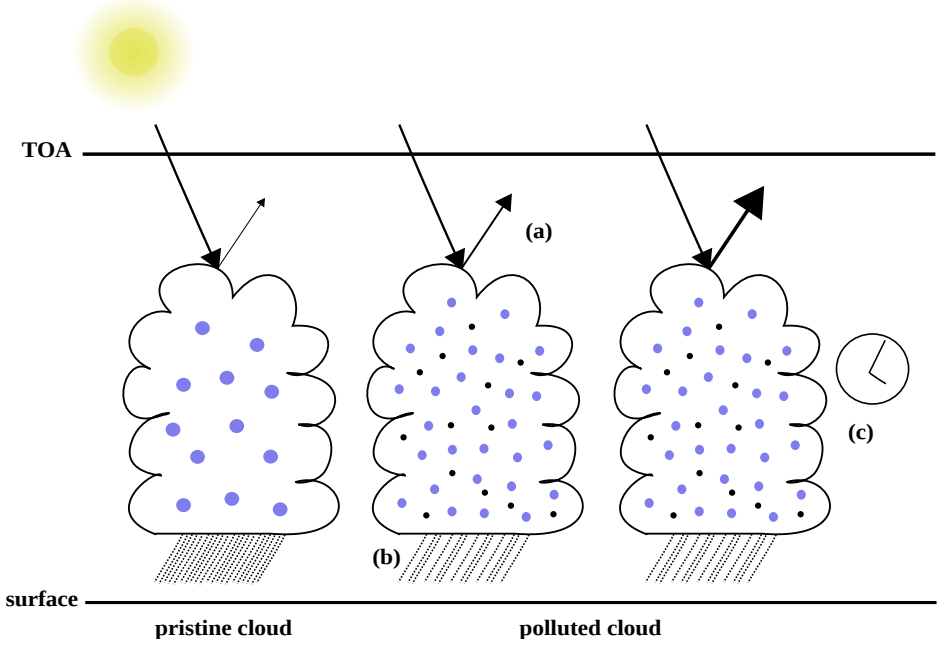

Figure 7.1: Schematic of aerosol effects: (a) first indirect radiative forcing (cloud albedo effect/ Twomey effect), (b) direct microphysical effect, (c) second indirect radiative forcing (cloud lifetime effect/ Albrecht effect). TOA refers to the top-of-the atmosphere. Blue (black) dots represent cloud droplets (aerosols).

(2008) noted that even though the effects of aerosols on clouds are more clearly understood, the effects on precipitation remain uncertain. Therefore, this study aims to improve the understanding of the climate impacts of increased loading of atmospheric aerosols on the SASM. To simulate the aerosol effects on clouds and precipitation in a scenario of higher atmospheric aerosol concentrations a simple experimental setup is used (described in section 7.1). By modifying the number of cloud droplets, this study imitates the aerosol's role in acting as cloud condensation nuclei in order to focus on the aerosol indirect effects. A schematic of the aerosol induced physical mechanisms that are subject of the present work is given in Fig. 7.1. Results from the model experiments are presented in section 7.2 with special focus on central India, a region known to have high load of atmospheric aerosols even during monsoon breaks (Manoj et al., 2012).

7.1 Experimental design

The newly tuned model setup (HH5-FINAL), described in chapter 6 is used in two numerical experiments, one representing the new HIRHAM5 control run condition (HH5-CTRL-nN) and the other the polluted case (HH5-POL-nN) in order to study the aerosol indirect effects on clouds and precipitation over the South Asian monsoon region. In both experiments, HH5-CTRL-nN and HH5-POL-nN, the nudging (see section 2.1.3.2) is switched off (no Nudging) to generate a free RCM simulation. To isolate the aerosol impact, the configuration setup including all boundary conditions are kept the same in the two simulations with the exception of the altered cloud droplet number concentration (N_l) in HH5-POL-nN. In this sensitivity study the influence of the cloud droplet concentration within the atmospheric boundary layer has been investigated. The HH5-POL-nN was performed using higher prescribed values for N_l in order to mimic the effects of aerosols by acting as cloud condensation nuclei. Aircraft measurements of continental and marine clouds (e.g. Heymsfield and McFarquhar, 2001; Nakajima et al., 2001; Ramanathan et al., 2001) show that in polluted atmosphere a sixfold increase in the aerosol number concentration led to a three- to fivefold increase in the cloud droplet number concentration (Kaufman et al., 2002). According to these findings, the fixed value of N_l in the standard setup was increased to a tripled (quadrupled) value of $N_\mathrm{l} = 660 \times 10^6\,\mathrm{m}^{-3}$ ($N_\mathrm{l} = 320 \times 10^6\,\mathrm{m}^{-3}$) over land (sea) (cp. section 2.1.2.2). The changed N_l directly effects the calculation of the mean volume droplet radius (R_vl) (see Eq. (2.28)) in the cloud microphysical scheme of HIRHAM5 with higher values of N_l leading to smaller values of R_vl. The aerosol effects on ice nucleation are not represented in this model experiment. Furthermore, this study does not take into account the chemical composition of the aerosol. It only investigates the following physical mechanisms (see Fig. 7.1): (a) the first indirect radiative forcing due to an increase in the reflection of solar radiation from clouds to space

by the higher cloud droplet number, (b) the direct microphysical effect due to the decrease of the cloud droplet radius by assuming the same amount of cloud liquid water content and (c) the second indirect radiative forcing due to an increase in cloud lifetime associated with a reduced precipitation efficiency (Ramanathan et al., 2001).
For reasons of model stability the configuration setup of both experiments was again modified following HIRHAM5 in Lucas-Picher et al. (2011). According to the prognostic model variables cloud liquid water content and cloud ice content (see section 2.1.1.1), an upstream advection scheme for the horizontal discretisation and an explicit Euler forward method for the time discretisation is used for the specific humidity. The two experiments were realised for thirteen years (2000-2012) from 1 May to 30 September.

7.2 Results

Fig. 7.2 shows the JJAS mean changes between the polluted case and the control condition (HH5-POL-nN minus HH5-CTRL-nN) in the spatial patterns of selected fundamental atmospheric model variables for the 2000-2012 period. Given that the same boundary conditions are used in the simulations, the changes between the two experiments are entirely caused by the modification of N_l.

Changes in the radiative forcing

Over the whole of the Indian peninsula with adjacent seas a decreased net shortwave radiation at the surface was simulated with maxima over the northern and western Arabian Sea and parts of Indo-China up to -55 W m^{-2} (Fig. 7.2 a). In order to provide a plausible explanation for the results the influence of a higher cloud droplet number concentration on the shortwave and longwave cloud optical properties has to be discussed. For the shortwave part of the spectrum the cloud optical properties in HIRHAM5 are expressed in terms of the effective radius of cloud droplets, which is a function of the cloud liquid water content and N_l (see section 2.1.2.3). In case of the liquid water phase, the higher N_l the smaller the effective radius of cloud droplets and the larger the mass extinction coefficient and the single scattering albedo. In the longwave part of the spectrum, where scattering may be neglected for typical 10 µm radius cloud droplets (Petty, 2006), the mass absorption coefficient of liquid clouds is formulated as a function of the effective radius of cloud droplets, where the absorption is exponentially growing with the increasing radius (see section 2.1.2.3). Hence, the change in the cloud optical properties due to the higher prescribed values of N_l in HH5-POL-nN directly influence the radiative fluxes calculated in the radiation code. Consistent with aircraft measurements (Kaufman et al., 2002), the more and smaller cloud droplets lead to an increased shortwave reflection of clouds. This is called the first indirect radiative forcing (Ramanathan

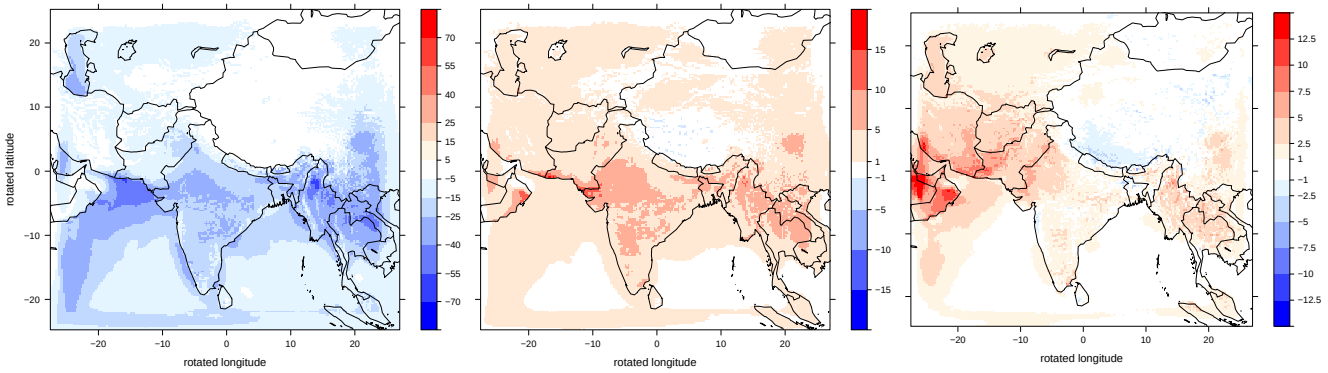

(a) srads (b) sradsu (c) trads

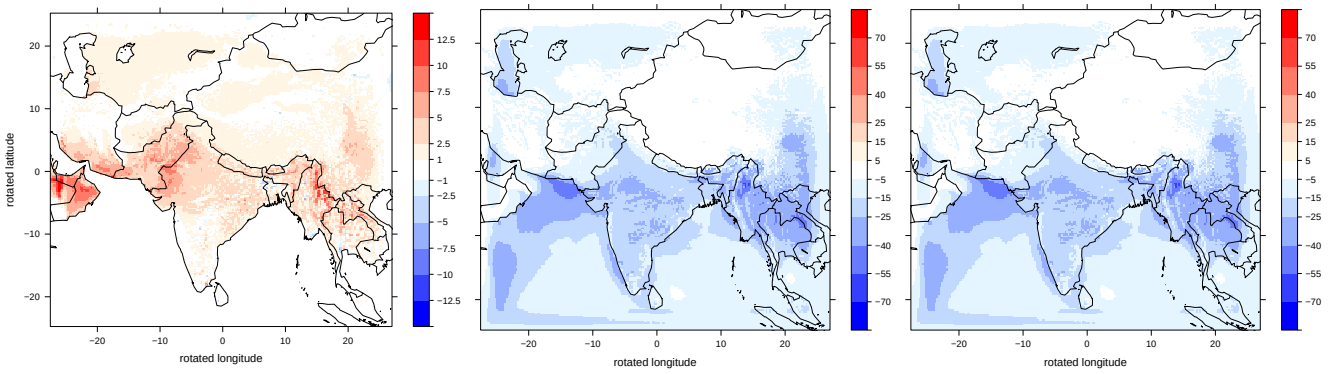

(d) tradsu (e) srad0 (f) srad0u

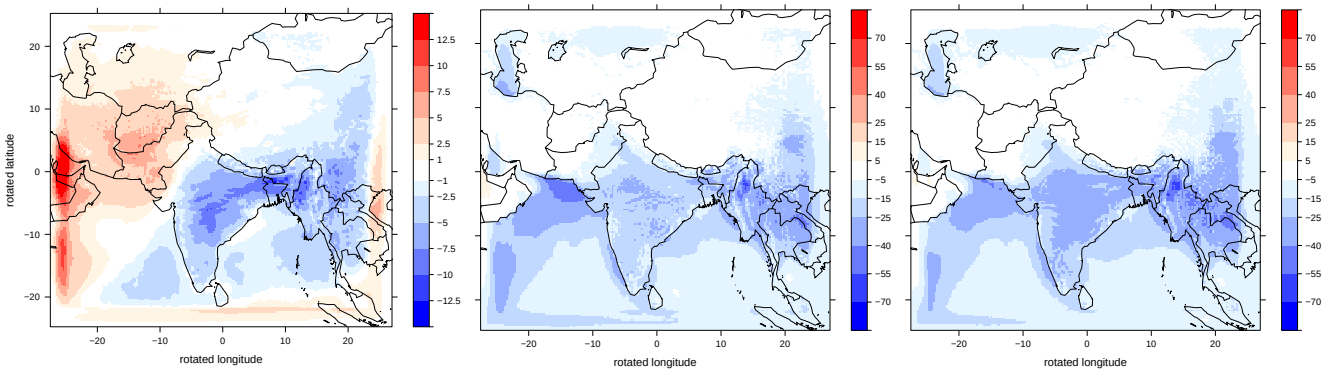

(g) trad0 (h) net rads (i) net rad0

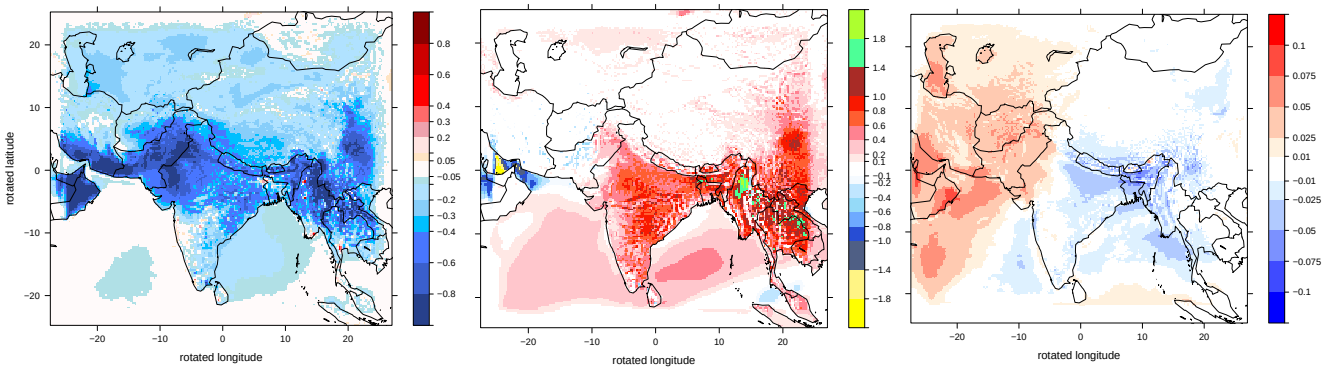

(j) temp2 (k) evap (l) tclcov

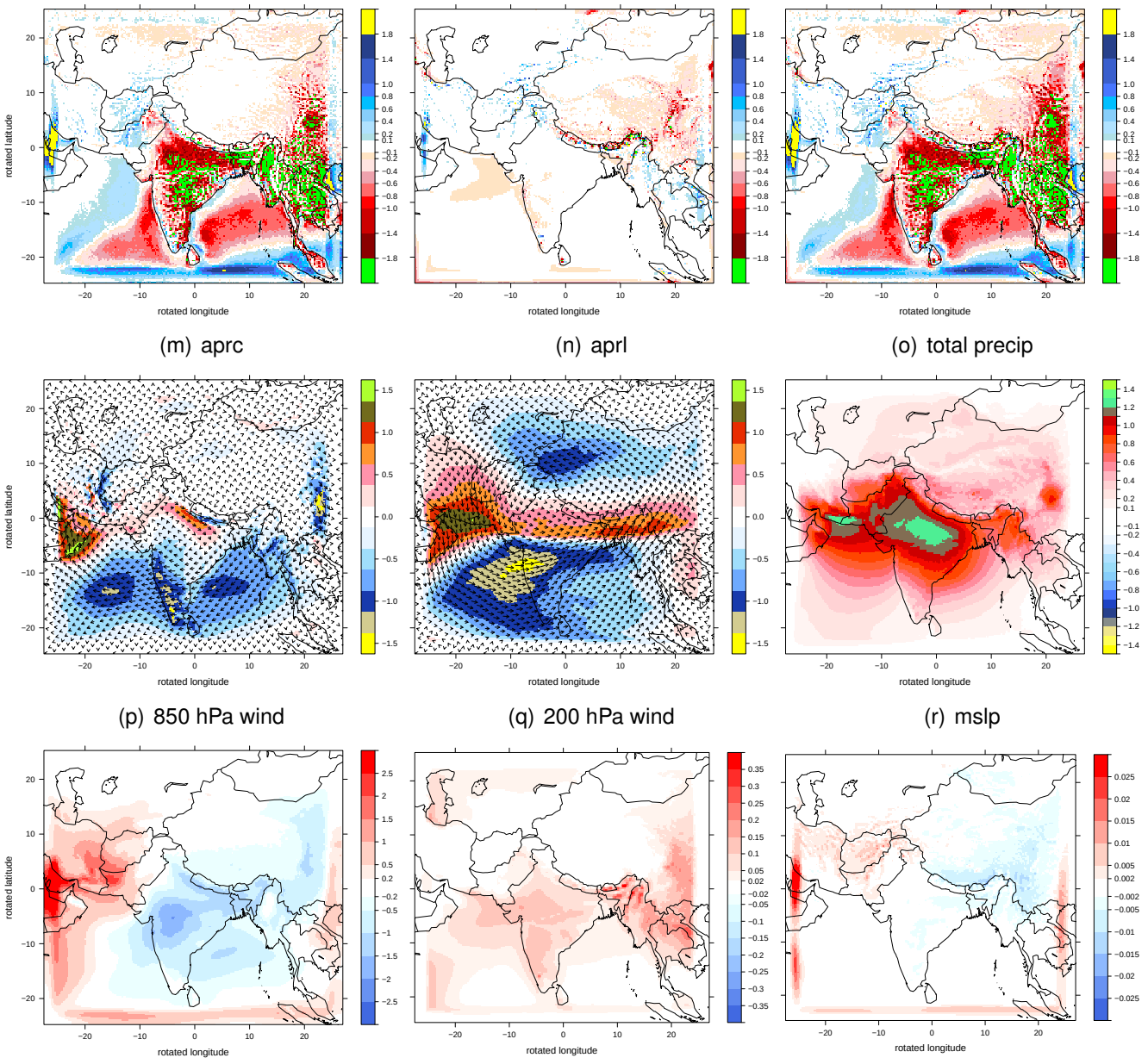

Figure 7.2: Mean JJAS 2000-2012 climatologies of the difference between HH5-POL-nN and HH5-CTRL-nN (HH5-POL-nN minus HH5-CTRL-nN) for net shortwave radiation at surface [W m^{-2}] (a), upward shortwave radiation at surface [W m^{-2}] (b), net longwave radiation at surface [W m^{-2}] (c), upward longwave radiation at surface [W m^{-2}] (d), net shortwave radiation at TOA [W m^{-2}] (e), upward shortwave radiation at TOA [W m^{-2}] (f), net longwave radiation at TOA [W m^{-2}] (g), sum of net shortwave and longwave radiation at surface [W m^{-2}] (h), sum of net shortwave and longwave radiation at TOA [W m^{-2}] (i), 2m-temperature [K] (j), evaporation [mm day^{-1}] (k), total cloud cover [dimensionless] (l), convective precipitation [mm day^{-1}] (m), large-scale precipitation [mm day^{-1}] (n), total precipitation [mm day^{-1}] (o), 850 hPa wind [m s^{-1}] (p), 200 hPa wind [m s^{-1}] (q), mean sea level pressure [hPa] (r), water vapour path [kg m^{-2}] (s), cloud liquid water path [kg m^{-2}] (t) and cloud ice water path [kg m^{-2}] (u). Note upward radiation fluxes including evaporation are negatively defined in the model, i.e. positive (negative) signs means reduced (enhanced) upward fluxes.

et al., 2001) or cloud albedo effect (Twomey, 1977). As a result, less solar radiation, which is the major source of energy for the climate system reaches the surface (around -30.5 W m^{-2} averaged over central India) (not shown) and hence less sunlight is reflected to space at the surface (Fig. 7.2 b, note upward radiation is negative defined in the model). The increase of the reflection of solar radiation by clouds is also indicated by the increase in the upward shortwave radiation flux at the top-of-the atmosphere (TOA) (around -23.5 W m^{-2} averaged over central India) (Fig. 7.2 f, note upward radiation is negative defined in the model), which is in the same order of magnitude as the changes in the net shortwave radiation at the surface (cp. Figs. 7.2 a,f). The comparison of the changes in the net shortwave and longwave radiative fluxes, at both the surface (Figs. 7.2 a and c, note the different scales) and TOA (Figs. 7.2 e and g, note the different scales) suggests that the contribution of the shortwave fluxes overwhelms the contribution of the longwave fluxes to the total net radiation (Figs. 7.2 h and i), especially at the surface. This implies that the total radiative forcing caused by the higher values of N_1 determines the surface energy balance crucially by reducing the net shortwave radiative fluxes (cp. Figs. 7.2 a,c,h).

In response to the first indirect radiative forcing less solar radiation can be absorbed by the Earth's surface. This corresponds to a cooling effect (Zubler, 2011). Averaged over central India the 2m-temperature is reduced by around -0.5 K in HH5-POL-nN. The largest temperature decreases up to -1 K were simulated over north-western India and Pakistan, parts of Indo-China and western Asia (Fig. 7.2 j). Overall, the differences in the 2m-temperature between HH5-POL-nN and HH5-CTRL-nN show a spatial pattern with cooling over the Asian continent and minor changes over the seas suggesting a decrease in the thermodynamic contrast between ocean and land. Liu et al. (2011) indicated in their modelling study on the effects of aerosols on clouds that such a spatial pattern of temperature changes could lead to the weakening of the Asian summer monsoon. Furthermore, it can be noted, that the regions of the largest cooling match that of the largest reduction in net shortwave radiative forcing at the surface with the exception of the areas with the strongest decrease in 2m-temperature over western Asia and Pakistan (cp. Figs. 7.2 j,a). This shows, that at the regional scale the temperature patterns and its responses to radiative forcing are affected by complex surface and atmospheric processes (Liu et al., 2011).

At the surface radiation, evaporation (latent heat flux from the surface to the atmosphere) and sensible heat flux balance each other (Ramanathan et al., 2001). The less solar radiation that reaches the surface causes less heat which is available for evaporating water (Rosenfeld et al., 2008). Therefore, over large parts of India and Indo-China the radiative surface cooling contributes to a reduced evaporation with changes up to 1 mm day^{-1} over India and up to 2 mm day^{-1} over regions of Southeast Asia (Fig. 7.2 k, note evaporation is negative defined in the model). Rosenfeld (2007) noted that around 37.3 % of the atmospheric heating occurs

by release of latent heat from vapour, when the reverse to evaporation occurs. This heat is left in the atmosphere and becomes available to energising convective rain clouds and drives the large-scale atmospheric circulation (Rosenfeld et al., 2008). Hence, a reduction in the amount of evaporation, which is balanced by the amount of rainfall at the global scale (Ramanathan et al., 2001; Rosenfeld et al., 2008), lead to a weakening of the hydrological cycle indicated by a decrease in the total precipitation (Fig. 7.2 o). The changes in the total precipitation over large parts of India and Indo-China (around -1.3 mm day^{-1} or -28.9 % averaged over central India) (Fig. 7.2 o) are primary caused by changes in the convective precipitation (around -1.2 mm day^{-1} or -27.3 % averaged over central India) (Fig. 7.2 m). While in these regions a reduction in the total precipitation is simulated, over parts of western Asia an increase in precipitation was found. Surprisingly, the large-scale precipitation is almost not affected by the higher prescribed values of N_l, especially over central India (Fig. 7.2 n). This is discussed in more detail below. Note that the ten-point boundary zone (described in detail in section 2.1.3.2) causes, as in the HH5-CTRL run (see chapter 5) an artificial simulation of the precipitation pattern (Figs. 7.2 m,l,o). An analysis of the spatial patterns of the changes in the different rain rate categories and their percentage contributions to the total JJAS rainfall amount between the polluted case and the control condition (HH5-POL-nN minus HH5-CTRL-nN) by using the same analysis method as in section 5.1.1 for the evaluation of HH5-CTRL is presented in Fig. 7.3. While, over large parts of India and Indo-China an increase of the percentage contribution to the total JJAS rainfall of 15–25 % is simulated for the rain class 1 (< 0.5 mm day^{-1}), a decrease of the percentage contribution for the rain class 4 (5–10 mm day^{-1}) and 5 (> 10 mm day^{-1}) of 5–20 % is found. This shows, that the suppression of total precipitation over these regions is a result of the reduced rainfall in the moderate to heavy rain rate categories.

By not raining, the condensed water remains in the clouds. This causes greater amounts of vertically integrated cloud liquid water over India and parts of Indo-China (Fig. 7.2 t). In addition to N_l, the cloud liquid water content within the cloud covered part of the grid cell is used to compute the cloud optical properties in the radiation code (see section 2.1.2.3). Thus, N_l also effects indirectly the cloud radiative properties due to the complex cloud dynamics in the model.

Changes in cloud microphysical properties

The cloud droplet number concentration determines largely precipitation-forming processes. In the cloud microphysical scheme of HIRHAM5 (see section 2.1.2.2) the autoconversion rate of cloud droplets is parameterised in terms of N_l. Assuming the same amount of cloud liquid water content, the higher N_l reduces the conversion of cloud droplets into raindrops due to the presence of more and smaller cloud droplets. Cloud droplets with smaller radii have

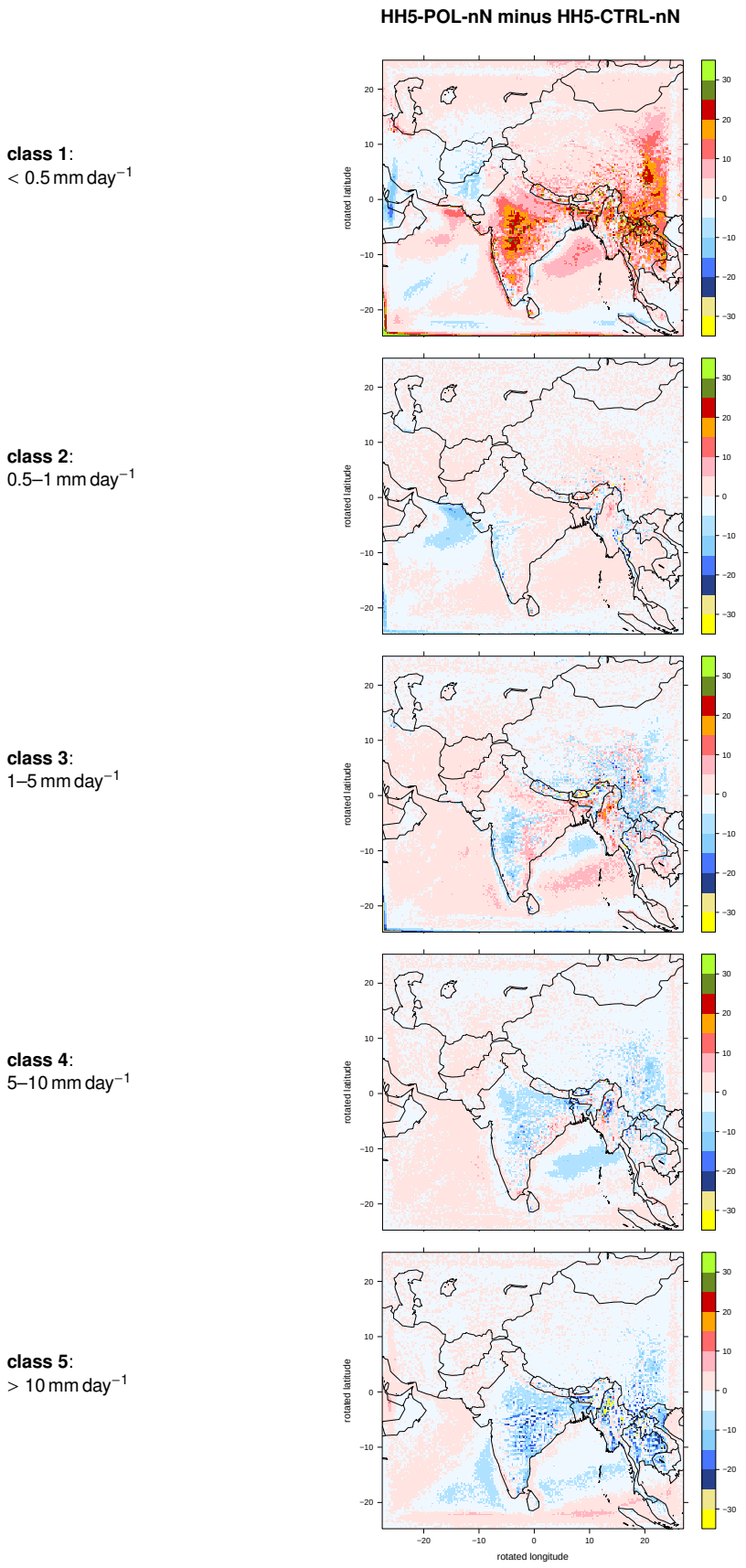

Figure 7.3: Differences in the spatial distribution of the percentage contributions of different rain classes to the total JJAS rainfall [%] based on the daily total precipitation of the sensitivity experiments HH5-POL-nN and HH5-CTRL-nN from 2000-2012. The rainfall classes are: class 1: $< 0.5\,\mathrm{mm\,day^{-1}}$, class 2: $0.5–1\,\mathrm{mm\,day^{-1}}$, class 3: $1–5\,\mathrm{mm\,day^{-1}}$, class 4: $5–10\,\mathrm{mm\,day^{-1}}$ and class 5: $> 10\,\mathrm{mm\,day^{-1}}$.

lower efficiencies to collide and coalesce, and can decelerate the formation of rain in warm clouds and hence suppress rainfall (Zubler, 2011). This is called the direct microphysical effect (Ramanathan et al., 2001). Furthermore, the reduced precipitation efficiency can increase the cloud life time, which in turn enhances the cloud reflectivity by the increased cloudiness. This effect is referred as the second indirect radiative forcing (Ramanathan et al., 2001) or cloud lifetime effect (Albrecht, 1989). Overall, both the direct microphysical effect and the second indirect radiative forcing may contribute to further spin down the hydrological cycle and hence suppress monsoon rainfall. However, it should be pointed out that only the stratiform cloud scheme (and not that of cumulus convection) includes the microphysics in HIRHAM5 (see section 2.1.2.2). Therefore, this study does not take into account the direct microphysical effect in cumulus convection. The observed changes in the total precipitation are dominated by changes in the convective precipitation, while the large-scale precipitation remains almost uneffected over India (cp. Figs. 7.2 m,n,o). Thus, this suggests that the reduction of the SASM precipitation mainly results from the indirect radiative forcing due to the important cloud-radiation interaction.

Changes in the monsoon circulation dynamics

During the summer monsoon season, the prominent regional feature of the South Asian region is the anticlockwise gyre of the monsoon trough over the Indo-Gangetic Plain in the lower troposphere (Ding and Sikka, 2006). With increased N_1 in the HH5-POL-nN experiment, the SASM has weakened. A clockwise anomaly over the Indian peninsula with anomalous easterlies over the Arabian Sea is simulated (Fig. 7.2 p). Such a circulation pattern leads to a suppression of the low-level westerly jet, which approaches South Asia from across the Arabian Sea and feeds moisture to the monsoon. As a consequence, this change in the large-scale atmospheric circulation contributes to a reduced moisture transport into the monsoon region. The damped intensity of the monsoon trough is also indicated by an increase in the mean sea level pressure up to 1.3 hPa over central India (Fig. 7.2 r). This anomalous high pressure system centres over central India and elongates with a second centre into the Northern Arabian Sea. In the upper troposphere, the Tibetan anticyclone and the easterly jet over India are attenuated by an anomalous cyclonic flow (Fig. 7.2 q).
The reduction in the inland directed water vapour transport, caused by the weakened SASM, combined with the radiation-related decrease in the evaporating fluxes lead to a loss of vertically integrated water vapour up to -2 kg m^{-2} over India (around -1.2 kg m^{-2} averaged over central India) (Fig. 7.2 s). However, over western Asia, the altered atmospheric circulation promotes an increase in the vertically integrated water vapour up to 2 kg m^{-2}. The anticyclonic anomaly over the Indian peninsula drives an anomalous northward directed moisture transport over the Northern Arabian Sea into western Asia (cp. Figs. 7.2 p,s). Such a spatial

dipole pattern of the changes in the vertically integrated water vapour between western Asia and South- and South-East Asia was also identified in the changes of the convective and hence total precipitation (cp. Figs. 7.2 m,o,s). This shows the important role of the atmospheric dynamics in influencing the free tropospheric moisture concentrations and thus the local rainfall patterns. Over western Asia, the enhanced moisture supply promotes an anomalous increase in the total cloud cover (Fig. 7.2 l). However, the cloudiness decrease over the northeast of the Indian peninsula seems inconsistent with the simulated local rainfall reductions and hence with the cloud lifetime effect (cp. Figs. 7.2 o,l). An examination of the vertical structure of the atmosphere, as discussed next for the central India region, is important to identify the responsible mechanism.

Effects over central India

While the vertical integrated picture of water vapour and cloud liquid water content over India suggests a free tropospheric moisture reduction in conjunction with an increase in the condensed water amount due to the local rainfall suppression, the decrease in total cloud cover over this region seems to be contradictory to the change in the cloud liquid water content (Figs. 7.2 s,t,l). This is likely related to various height-dependent N_l-induced effects on the vertical structure and stability of the atmosphere. Therefore, Figs. 7.4 (a,b,c) representatively examine for the central India region (21°-27°N, 72°-85°E) the differences in the vertical distributions of temperature and specific humidity (a), cloud liquid water content and fractional cloud cover (b), and dry static energy and MSE (moist static energy) (c) between the polluted case and the control condition (HH5-POL-nN minus HH5-CTRL-nN). In the tropics, within the first 5 km above the surface the temperature decreases steeply with altitude, resulting in an instability of the lower troposphere, which triggers together with low-level moisture convergence deep convection and rainfall (Ramanathan et al., 2005). The prescribed higher values of N_l in the polluted case inhibits this instability by cooling the surface and the lower troposphere due to radiative effects and less cooling the upper troposphere (Fig. 7.4 a). The radiative cooling up to -0.48 K is largely confined to the layer between the surface and 800 hPa. Over central India, the entire troposphere experiences a humidity reduction, with greater drying at the surface (Fig. 7.4 a) leading to a weakened vertical specific humidity gradient. This in turn is consistent with the decrease in the evaporative fluxes over the region (cp. Fig. 7.2 k).

As noted by other studies (e.g. Kiranmayi and Maloney, 2011; Maloney, 2009; Prasanna and Annamalai, 2012) lower tropospheric MSE changes are almost entirely determined by anomalous moisture. Thus, a strong similarity exists in the vertical behaviour of MSE and specific humidity changes (cp. Figs. 7.4 a,c). Over the entire troposphere MSE is reduced in the polluted case. This is important because a change in the planetary boundary layer

MSE effects the convective instability, and hence the frequency and magnitude of rainfall events in the Tropics (Pal and Eltahir, 2001). Thus, the decrease of tropospheric MSE results in a reduced moist convection. The upper tropospheric and lower stratospheric MSE anomalies are regulated by temperature anomalies, and the simulated warming of the upper troposphere results in an increase of dry and moist static energy (cp. Figs. 7.4 a,c).
While the total cloud cover suggests a decrease of cloud amount over central India (Fig. 7.2 l), the vertical structure of the fractional cloud cover reveals a mid-tropospheric increase in cloudiness with a peak at around 600–850 hPa (Fig. 7.4 b). According to the cloud lifetime effect, in this tropospheric layer the increased cloud cover is associated with the largest

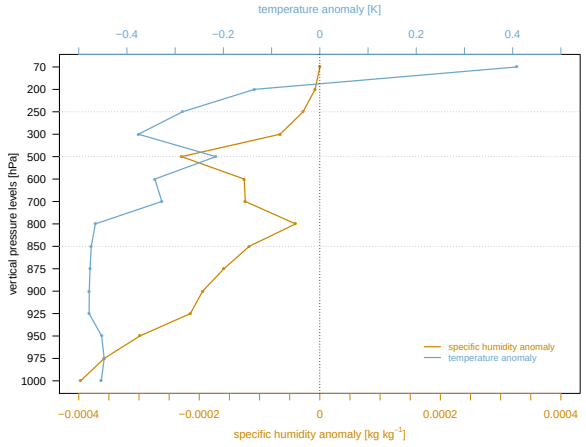

(a) temperature and specific humdity

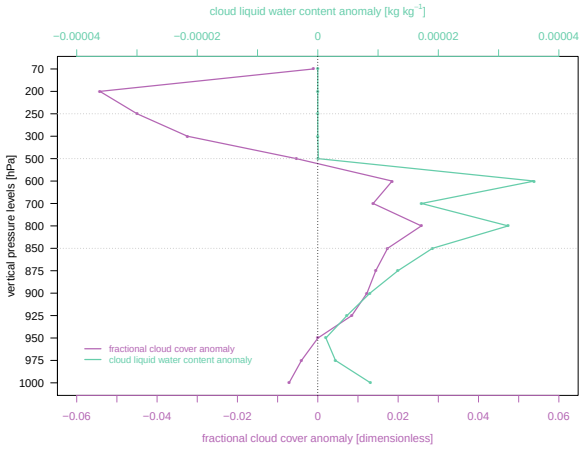

(b) cloud liquid water content and fractional cloud cover

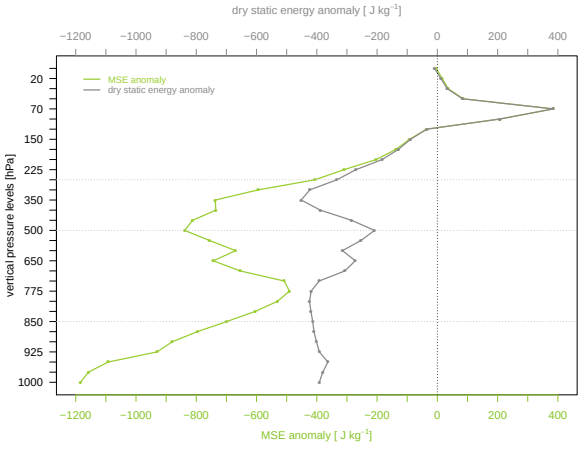

(c) dry static energy and MSE

Figure 7.4: Vertical distribution of changes between the polluted case and the control condition (HH5-POL-nN minus HH5-CTRL-nN) for temperature [K] and specific humidity [kg kg^{-1}] (a), cloud liquid water content [kg kg^{-1}] and fractional cloud cover [dimensionless] (b), and dry static energy [J kg^{-1}] and MSE [J kg^{-1}] (c) averaged over central India (21°- 27°N, 72°- 85°E). The dotted black vertical line marks the zero line. Note that the number of pressure level is different in (c) compared to (a,b), because the dry static energy and MSE calculation based on model level data, which are interpolated to pressure levels according to the MSE budget study in section 5.2.3.

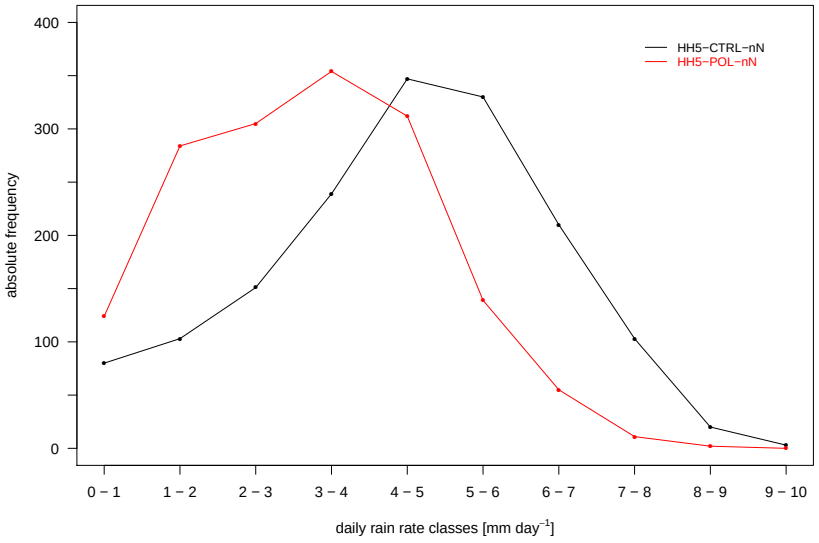

Figure 7.5: Absolute frequency of daily rain rates [mm day^{-1}] for the sensitivity experiments HH5-CTRL-nN and HH5-POL-nN averaged over central India (21°-27°N, 72°-85°E) of the summer monsoon period (JJAS) from 2000-2012.

increase in the cloud liquid water content (Fig. 7.4 b). Above 500 hPa, a strong reduction in cloud fraction is apparent. This could indicate that clouds in the control run reach higher levels of the atmosphere than in the polluted case, implying that radiative cooling of the lower troposphere reduces convective overturning of deep clouds (Fig. 7.4 a,b). This would be consistent with an analysis of the absolute frequency of daily rain rates averaged over central India during the summer monsoon period (Fig. 7.5). A decrease of the frequency of moderate to heavy rain rates together with an increase of the frequency of lighter rain rates in the polluted case is in line with the suppression of deep convective rain clouds and associated precipitation. Likewise, the reduction of the cloud ice content above 500 hPa (not shown) indicates the inhibition of deep cloud growth.

The results presented so far address the influence of higher prescribed values for N_1 on the seasonal mean monsoon climate. However, aerosols can also modify the monsoon on intraseasonal timescales (active-break cycles) (Manoj et al., 2011, 2012). Manoj et al. (2012) noted that the Twomey effect was the dominant factor in inhibiting efficient precipitation over central India during the long June break of 2009. They found that the aerosol indirect effect can promote dry spells through the suppression of cloud growth due to the decrease of the cloud effective radius associated with high loading of aerosols in fixed liquid water content scenario. Likewise, Bhawar and Rahul (2013) hypothesise that aerosols invigorate drought like conditions by affecting the deep cloud formation.
In order to investigate the break characteristics between the two experiments (HH5-CTRL-nN

and HH5-POL-nN) the number and duration of monsoon breaks are calculated by using the same identification procedure for breaks as described in section 4.1 but with a different time period for the established phase of the monsoon over India compared to HH5-CTRL (1 July - 17 September, see Fig. 4.1). The period 15 June - 25 September represents the prevailing monsoon phase over India in HH5-CTRL-nN. In total, for the polluted case 2 more break phases are identified during the 13 years (2000-2012). The analysis indicates a shift towards more frequent short breaks (3 days) due to the higher values of N_1 in HH5-POL-nN (Fig. 7.6). No substantial difference in the number of extended breaks ($\geq$ 7 days) is detected, but breaks persisting for 4-6 days seem to occur less frequently in the polluted case.

Although a simple approach is used to investigate the complex aerosol-cloud-interactions, the present research helps to advance the understanding of aerosol impacts on clouds and precipitation during the South Asian summer monsoon season. By increasing the cloud droplet number concentration the experimental design of this study mimics the role of aerosol particles acting as cloud condensation nuclei and focuses on the indirect aerosol effects. Motivated by recent investigations which postulate the aerosol induced microphysical effects as a trigger point in enhancing drought like conditions (e.g. Bhawar and Rahul, 2013; Manoj et al., 2012), the hypothesis is tested that the increase in cloud droplet number concentration, which imitates a scenario of higher atmospheric aerosol amounts, leads to spin down the hydrological cycle and hence promotes break events over central India. The tendency of occurrences of breaks in a polluted scenario is examined through analysing numerical model simulations.

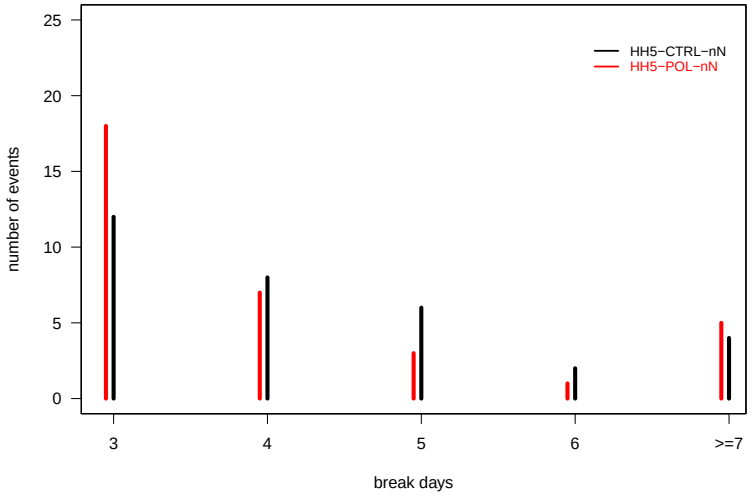

Figure 7.6: Histogram of break days identified from modeled total precipitation averaged over central India (21°-27°N, 72°-85°E) for the sensitivity experiments HH5-CTRL-nN and HH5-POL-nN (2000-2012). The identification of break days focus on the period 15 June - 25 September, which represents the established phase of the monsoon over India in HH5-CTRL-nN.

In summary the results propose the following mechanism. According to the first indirect radiative forcing, the more and smaller cloud droplets decrease the amount of shortwave radiation reaching the surface by enhancing the cloud reflectivity, and induce a radiative cooling over India. The cooling in turn causes that less heat is available for evaporation at the surface and hence for energising convective clouds in the atmosphere. First, this suppression of cloud growth contributes to a weakening of the hydrological cycle over India. Second, a stabilisation of the troposphere induced by a simulated stronger cooling of the surface and lower troposphere than of the upper troposphere over central India inhibits the convective activity. The suppressed development of deep convective rain clouds and the associated reduction of high-level ice clouds is reflected in an upper tropospheric decrease in cloudiness and a reduction in the cloud ice content above 500 hPa (not shown). In line with the second direct radiative forcing, by not raining the remaining condensed water increases the cloud fraction in the lower and middle tropospheric layers over central India. This in turn enhances further due to the cloud life time effect the reflection of solar radiation and thus the radiative cooling in the region. Changes in the cloud amount and cloud-top-height are key factors that determine the magnitude and sign of the climate forcing, because changes in cloud height can shift the effect of clouds from warming to cooling (Koren et al., 2008). While low clouds have a net cooling effect, high clouds more effectively trap longwave radiation and thus increase surface warming (Boucher et al., 2013). Therefore, the increase in low and mid-level cloud amount together with the decrease in high-level clouds amplifies the surface cooling. A different spatial pattern of temperature changes with largest cooling over land and minor changes over the adjoining ocean results in a reduced land-sea thermodynamic contrast and in turn weakens the intensity of the SASM. Third, the anomalous anticyclonic low-level circulation over central India reduces the moisture transport into the monsoon region, an important source of water vapour for monsoon rainfall, by anomalous easterlies over the Arabian Sea and the Bay of Bengal. A similar anomalous circulation pattern is simulated during break conditions (cp. section 5.2.2). Fourth, according to the direct microphysical effect the increased cloud droplet concentration together with the decreased cloud droplet size suppress the conversion of cloud droplets into rain drops in stratiform clouds and hence contribute further to reduce precipitation over central India.

All of the above discussed changes contributes to a weakening of the SASM and associated rainfall. However, over central India the simulated changes in the total precipitation, which are dominated by changes in the convective rainfall, are primary determined by the N_1-induced radiative forcing on the shortwave radiation fluxes. Furthermore, the study demonstrates that the changes in the monsoon circulation also influence the variation in the South Asian summer monsoon precipitation.

In summary the present research confirms that higher concentrations of cloud droplets, caused for example by a higher load of atmospheric aerosols, reduce moderate and heavy rainfall events by inhibiting deep convective cloud growth over central India. However, the monsoon break analysis disproves the hypothesis of Bhawar and Rahul (2013). More and smaller cloud droplets clearly reduce the mean summer monsoon precipitation, but do not trigger more long breaks over central India. Only an increase in the occurrence of short breaks (3 days) is simulated.

8 Summary and conclusion

8.1 Summary

Moist dynamical processes that control breaks during the South Asian summer monsoon (SASM) are investigated using the atmospheric regional climate model (RCM) HIRHAM5 at a horizontal resolution of 0.25° driven by the ERA Interim reanalysis. By performing moisture and moist static energy (MSE) budgets on the output of the RCM, the various competing mechanisms are quantitatively estimated. Furthermore, a current issue of large uncertainty is addressed that an increase in aerosols over India can play an important role in suppressing monsoon rainfall and hence in initiating breaks. Given the fact that cloud-radiation interactions influence the evolution of monsoon breaks, the changes in the frequency and duration of break phases in a scenario of higher atmospheric aerosol concentrations are examined by a sensitivity experiment.

While an evaluation of the model in its standard configuration set up against state-of-the-art gauges-based observational products and satellite data reveals an underestimation of the mean summer monsoon rainfall due to deficiencies in the simulation of the convective precipitation, the model is capable of reproducing the spatial pattern of the subseasonal variation of the SASM. This ability of HIRHAM5 in simulating the monsoon's intraseasonal variability formed the basis for the comprehensive monsoon break analysis following the method by Prasanna and Annamalai (2012).
The moisture budget analysis shows that over central India, precipitation and moisture convergence are the dominant terms. While quantitatively moisture divergence accounts for around 65.5 % of the rainfall anomalies during the peak break phase, the role of moisture advection deserves attention (~20.5 %). Su and Neelin (2002) noted that the reason for the seeming balance between precipitation and moisture convergence, is that moisture convergence is a "feedback" term in the chain of moist convective response to warm SST forcing. However, the MSE budget analysis sheds light on the processes responsible for monsoon breaks and highlights the dominance of dry advection during the initiation phase of breaks. The proposed moist dynamical mechanisms that trigger and maintain monsoon

breaks can be summarised as follows. 15–10 days before the negative rainfall anomalies develop over central India, anomalous dry advection intensifies over the northern Arabian Sea due to anomalous low-level north-westerlies over Iran and western Pakistan, which carry warm and dry air from the deserts of western Asia. As noted by earlier studies (e.g. Annamalai and Slingo, 2001; Annamalai and Sperber, 2005; Krishnan et al., 2000; Prasanna and Annamalai, 2012), an anticyclonic circulation anomaly over India develops as a Rossby wave response to anomalous negative rainfall over the equatorial Indian Ocean during these pentads. At day -5, the westerlies at the northward flank of this anomalous circulation transport the drier air originating from over the deserts of western Asia toward central India. First, this advection of low-MSE air triggers the dryness over central India (Fig. 8.1). Second, the easterlies at the southern flank of this anomalous anticyclone weaken the low-level cross-equatorial jet and thus reduce the moisture transport into the monsoon region (Fig. 8.1). From -5 days onwards, the dry conditions over India, which are associated with a reduction in cloud cover (Prasanna and Annamalai, 2012) lead to an anomalous radiative cooling. During the same period, enhanced precipitation along the near-equatorial Indian Ocean promotes anomalous radiative warming. Since, from a thermodynamic point radiative cooling is balanced by diabatic subsidence (Hoskins and Wang, 2006), these two out of phase heat regions are connected by a thermally driven meridional circulation. Third, this local Hadley circulation can inhibit convective cloud growth by causing anomalous descent over central India and hence can maintain break conditions (Fig. 8.1). Fourth, a cyclonic response to the positive rainfall anomalies along the near-equatorial Indian Ocean amplifies further the anomalous low-level easterlies over southern India and the Arabian Sea, and thus contributes also to a divergent flow over central India (Fig. 8.1).

A sensitivity experiment that mimics a scenario of higher atmospheric aerosol concentrations is performed to study the indirect aerosol effects over the South Asian monsoon region. The aerosol's role in acting as cloud condensation nuclei is realised by an increased cloud droplet number concentration. The change of the microphysical cloud properties leads to a reduction of the mean SASM rainfall due to many competing effects. Results of the sensitivity study propose the following mechanisms. According to the first indirect radiative forcing, the larger number concentration of smaller cloud drops enhances the reflectivity of solar radiation, which promotes less shortwave radiation reaching the surface and hence induce a radiative cooling over India. This surface cooling causes a decrease in evaporation, an important source of moisture for the monsoon and thus contributes to a weakening of the hydrological cycle. Furthermore, the aerosol-imposed cooling of the surface and lower troposphere, and less cooling of the upper troposphere stabilise the troposphere and thus inhibit vertical growth of clouds. An analysis of the frequency of different daily rain rates over central India,

confirms this suppressed deep convective clouds developing in the polluted atmosphere by identifying less events of moderate and heavy rainfall and more events of lighter rain rates. In line with the second indirect radiative forcing, the suppression of precipitation can enhance the cloud life time and hence the cloud reflectivity, which intensifies further the radiative cooling. Likewise, the simulated increase in low and mid-level clouds together with the decrease in high-level clouds over central India amplify the surface cooling. Changes in the monsoon circulation dynamics are also found to be responsible for the reduction in monsoon precipitation. A spatially differential cooling, caused by radiative forcing through the indirect aerosol effects leads to a reduced land-sea thermodynamic contrast, which in turn weakens

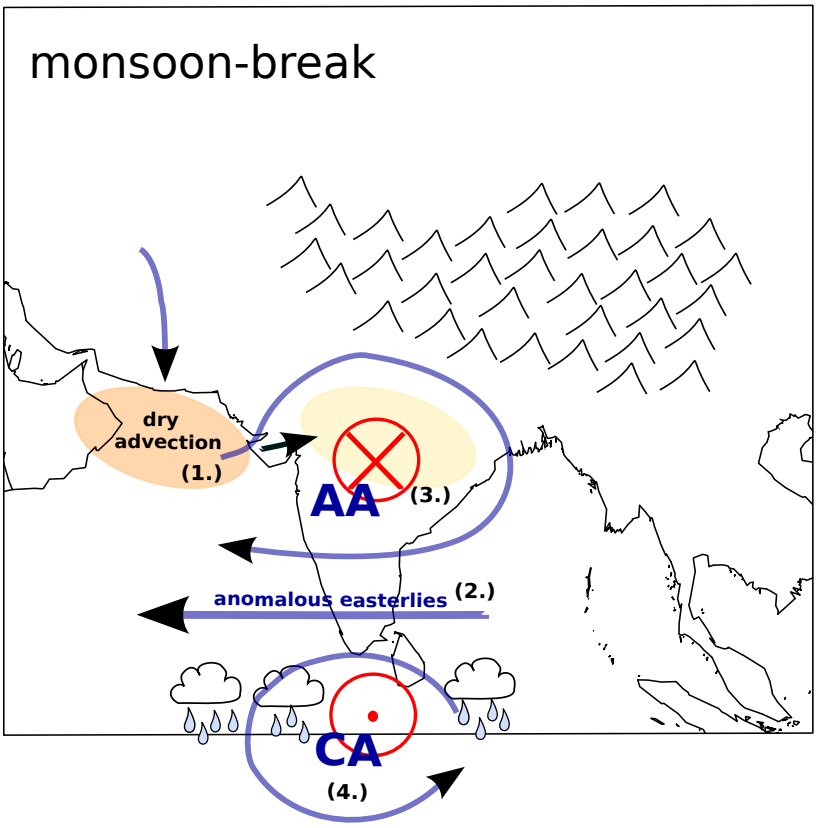

Figure 8.1: Schematic of moist dynamical processes that control breaks during the South Asian summer monsoon. While negative rainfall anomalies prevail over central India, convection is enhanced over the near-equatorial Indian Ocean during monsoon breaks. The break conditions arise and maintain due to different competing processes: (1.) Advection of dry air from western Asia toward central India, (2.) anomalous easterlies in association with an anticyclonic circulation anomaly over India reduce the moisture transport into the monsoon region, (3.) a local Hadley circulation forced by cloud-radiation feedbacks promotes anomalous descent over central India, and (4.) a cyclonic response to positive rainfall anomalies over the near-equatorial Indian Ocean contributes to the divergent flow over central India by amplifying the anomalous low-level easterlies over the Arabian Sea. 'AA' and 'CA' refer to the anticyclonic circulation anomaly over India and the cyclonic circulation anomaly over the equatorial Indian Ocean, respectively. Blue marks low-level circulation features. The anomalous meridional circulation with anomalous rising over the equatorial Indian Ocean and anomalous descent over central India (local Hadley cell) is highlighted in red.

the intensity of the SASM by an anticyclonic circulation anomaly over India, similar to break conditions. This anomalous anticyclone reduces the moisture transport over the Arabian Sea and the Bay of Bengal into the monsoon region. Besides the aerosol indirect radiative effects, microphysical impacts of aerosols determine the changes in monsoon rainfall. According to the direct microphysical effect, the more and smaller cloud droplets slow the coalescence and conversion of cloud droplets to raindrops and subsequently reduce precipitation.
All of the above processes work in the same direction. Higher cloud droplet number concentrations reduce heavy rainfall events by inhibiting deep convective activity mainly due to the aerosol indirect radiative effects, and lead to a reduction of the SASM precipitation associated with a weakening of the monsoon circulation. However, an analysis of the statistics of break days in the polluted cloud scenario disproves the hypothesis of Bhawar and Rahul (2013), derived from investigations of satellite products, that aerosols can trigger long drought like conditions. The larger number concentration of smaller cloud droplets clearly suppresses the mean SASM precipitation, but does not initiate more long breaks over central India. On the contrary, an increase in the occurrence of short breaks (3 days) is noticeable.

Based on the identified deficiencies of HIRHAM5 in reproducing the SASM climate by using its standard configuration set up, a set of numerical model simulations is conducted in order to assess the monsoon's sensitivity in terms of tunable model parameters, that are related to processes not explicitly represented at the model grid resolution (Mauritsen, 2012). Biases in the mean June-September patterns of convective precipitation and evaporation motivated the selection of tuning parameters controlling convective cloud and soil moisture processes. Likewise, the effects on the monsoon climate are tested with respect to the choice of the cloud cover scheme. The study reveals that HIRHAM5 is highly sensitive to the cloud cover scheme used in the model set up. A ~5.1 % increase in the simulated All-India Monsoon Rainfall (AISMR) is achieved by using the diagnostic clover scheme of Sundqvist et al. (1989) instead of the statistical cloud cover scheme of Tompkins (2002). Furthermore, higher values of the cumulus convection scheme tuning parameter k_{conv}, that determines the conversion rate of cloud water to rain and snow, higher (lower) values of the minimum (maximum) threshold of the terrain steepness σ_0 (σ_{max}), which control the efficiency of surface runoff in the surface parameterisation scheme, and higher values of d, a parameter that determines the efficiency of the fast drainage are able to improve the underestimation of the summer monsoon rainfall over India. A combination of these adjustable parameters leads to a further increase of the AISMR index of ~4.1 %.

8.2 Discussion

While it is a fact that the frequency of break spells has been increasing over India in the recent decades (Singh et al., 2014), the identification of the processes responsible for breaks during the SASM is still in the beginning stage. By analysing gauges-based observational products, satellite and reanalysis data sets, several studies addressed the dynamics of the transition from active to break monsoon phases (e.g. Annamalai and Slingo, 2001, Bhat, 2006, Krishnamurti et al., 2010, Rao et al., 2004). Efforts to simulate aspects of the monsoons active and break cycles by dynamical models are also in progress (e.g. Annamalai, 2010, Krishnan et al., 2000, Prasanna and Annamalai, 2012). However, the use of RCMs to improve the understanding of the SASM dynamics and intraseasonal variability by benefiting from its resolution advantage has not yet become established. This work is the first study applying moisture and MSE budget analyses according to the method by Prasanna and Annamalai (2012) on the output of a RCM in order to identify moist dynamics that trigger and maintain monsoon breaks during the SASM. Despite deficiencies in the simulation of the mean monsoon precipitation, the ability of HIRHAM5 in reproducing the proposed moist mechanism by Prasanna and Annamalai (2012) encourages the use of this RCM in analysing the interactions of moist physics and circulation that lead to monsoon breaks.

Nevertheless, climate models need to capture the mean monsoon structure (Annamalai, 2010). But, this represents a challenge, because of the complexity of the monsoon phenomenon and not adequately represented physical processes in the models (e.g. the cloud generation and precipitation formation). Tuning of uncertain or non-observable model parameters is an integral part of the model development process (Mauritsen, 2012). The adaptation of parameterisations implemented in HIRHAM5 to the tropical monsoon climate is addressed in this study for the first time and still an ongoing process.

HIRHAM5 is a hydrostatic model. Contrary to non-hydrostatic models, which solve a prognostic equation for the vertical velocity, in hydrostatic models the vertical equation is reduced to an approximation of hydrostatic balance between the pressure gradient force and the force of gravity (Holton, 2004). As a consequence the vertical velocity is diagnosed from the continuity equation by relating horizontal divergence to vertical motion. Therefore, hydrostatic models are primary designed to study meso-scale processes. The use of this hydrostatic approximation limits the vertical velocity calculation within HIRHAM5, which becomes visible by the convective precipitation biases.

As noted by earlier studies, one limitation in the MSE budget study is the contribution by a residual term of uncertain sign. Consistent with the results of Prasanna and Annamalai (2012), a MSE budget residual exists that is of the same order of magnitude as the moisture advection and in opposite phase with it. Since, the residuals have also been found in reanal-

ysis products Kiranmayi and Maloney (2011) suggested that the residual term appears to be a result of missing or miscalculated MSE sources in the data sets. Interpolations from native model coordinates to standard pressure levels can contribute to large residuals. Likewise, the fact that the vertically integrated vertical advection of MSE arises due to cancellation of large terms in the moisture and temperature equations is expected to introduce a residual term (Prasanna and Annamalai, 2012). Residuals in this study can also result from neglecting horizontal diffusion in the horizontal advection terms in the moisture and MSE equations.
The present research highlights the important role of increased aerosol concentrations over South Asia in suppressing the summer monsoon precipitation. Although a simple approach is applied, the sensitivity experiment can help to explain the physical processes associated with indirect aerosol effects. While, this study takes into account the aerosols function as cloud condensation nuclei, aerosol effects on ice nucleation are not represented in the model experiment. Furthermore, this study does not consider the chemical composition of the aerosol.

8.3 Outlook

Further research is needed in order to address the emerged issues as discussed above. The important role that small-scale processes such as deep convection play in the climate of the tropics and in particular in the monsoon system calls for the use of a non-hydrostatic model. It is therefore desirable to repeat this model study by using a RCM without the hydrostatic limit and with further increased horizontal resolution ($< 25\,\text{km}$). More work is required to find appropriate convection schemes in order to improve the simulation of the summer monsoon precipitation. For a better understanding, further sensitivity studies are needed to investigate the influence of different convection schemes. Moreover, the tuning of uncertain or non-observable parameters related to precipitation formation, convective and soil moisture processes to the tropical monsoon climate should be a major focus of future work.
The large residual terms in the moisture and MSE budget studies need to pay more attention. Therefore, the results have to be validated with other RCM simulations and observationally based data sets. Given the identified mechanisms for monsoon breaks, case studies for selected normal, drought and wet monsoon years will shed light on the role of breaks in influencing the seasonal mean and hence the monsoons interannual variability. Furthermore, it would be interesting to examine reasons for the absence of breaks during some years.
Rosenfeld et al. (2008) emphasised the important function of ice precipitation particles in invigorating convection and rainfall in polluted clouds. Therefore, sensitivity experiments that take into account the aerosol effects on ice nucleation are necessary. However, in order

to fully understand the interactions between aerosols, clouds, precipitation and radiation including the direct, semi-direct and indirect aerosol effects over South Asia it is anticipated to use fully coupled aerosol-climate RCMs. In addition, future research should further address one of the main unresolved issues, the impacts of aerosols on climatic extremes, such as droughts and floods. A comprehensive understanding of the origin of extended break events is essential in order to formulate effective strategies for managing the potential risks inherent to long-lasting dryness (Singh et al., 2014). Finally, predicting monsoon breaks would aid to prevent disasters associated with monsoon intraseasonal rainfall variability.

Bibliography

Albrecht, B. (1989), Aerosols, Cloud Microphysics, and Fractional Cloudiness, Science, 245, 1227–1230.

Alexandru, A., R. de Elia, R. Laprise, L. Separovic, and S. Biner (2009), Sensitivity Study of Regional Climate Model Simulations to Large-Scale Nudging Parameters, Mon. Weather Rev., 137, 1666–1686, doi:10.1175/2008MWR2620.1.

Annamalai, H. (2010), Moist Dynamical Linkage between the Equatorial Indian Ocean and the South Asian Monsoon Trough, J. Atmos. Sci., 67, 589–610, doi:10.1175/2009JAS2991.1.

Annamalai, H., and J. M. Slingo (2001), Active/break cycles: diagnosis of the Intraseasonal variability of the Asian Summer Monsoon, Clim. Dynam., 18, 85–102, doi:10.1007/s003820100161.

Annamalai, H., and K. R. Sperber (2005), Regional Heat Sources and the Active and Break Phases of Boreal Summer Intraseasonal (30-50 Day) Variability, J. Atmos. Sci., 62, 2726–2748, doi:10.1175/JAS3504.1.

Ashfaq, M., Y. Shi, W. w. Tung, R. J. Trapp, X. Gao, J. S. Pal, and N. S. Diffenbaugh (2009), Suppression of south asian summer monsoon precipitation in the 21st century, Geophys. Res. Lett., 36, L01704, doi:10.1029/2008GL036500.

Berrisford, P., et al. (2009), The ERA-Interim Archive, ERA Report Series 1 Version 2.0, European Centre for Medium-Range Weather Forecasts, Reading, UK.

Betts, A. K., and M. J. Miller (1986), A new convective adjustment scheme. Part II: Single column tests using GATE wave, BOMEX, ATEX and artic air-mass data sets, Q. J. R. Meteorol. Soc., 112, 693–709, doi:10.1002/qj.49711247308.

Bhat, G. S. (2006), The Indian drought of 2002 - a sub-seasonal phenomenon?, Q. J. R. Meteorol. Soc., 132, 2583–2602, doi:10.1256/qj.05.13.

Bhawar, R. L., and P. R. C. Rahul (2013), Aerosol-Cloud-Interaction Variability Induced by Atmospheric Brown Clouds during the 2009 Indian summer Monsoon Drought, Aerosol Air Qual. Res., 13, 1384–1391, doi:10.4209/aaqr.2012.11.0329.

Bollasina, M. A., Y. Ming, and V. Ramaswamy (2013), Earlier onset of the Indian monsoon in the late twentieth century: The role of anthropogenic aerosols, Geophys. Res. Lett., 40, 3715–3720, doi:10.1002/grl.50719.

Boucher, O., et al. (2013), Clouds and Aerosols, in Climate Change 2013: The Physical Science Basis. Contribution of Working Group I to the Fifth Assessment Report of the Intergovernmental Panel on Climate Change, edited by T. F. Stocker, D. Qin, G.-K. Plattner, M. Tignor, S. K. Allen, J. Boschung, A. Nauels, Y. Xia, V. Bex, and P. M. Midgley, Cambridge University Press, Cambridge, UK and New York, NY, USA.

Christensen, J. H., O. B. Christensen, P. Lopez, E. van Mejigaard, and M. Botzet (1996), The HIRHAM4 Regional Atmospheric Climate Model, Sci. Rep. 96-4, Danish Meteorological Institute, Copenhagen, DK.

Christensen, O. B., M. Drews, J. H. Christensen, K. Dethloff, K. Ketelsen, I. Hebestadt, and A. Rinke (2007), The HIRHAM Regional Climate Model Version 5 (ß), Tech. Rep. 06-17, Danish Meteorological Institute, Copenhagen, DK.

Davies, H. C. (1976), A lateral boundary formulation for multi-level prediction models, Q. J. R. Meteorol. Soc., 102, 405–418, doi:10.1002/qj.49710243210.

Davies, H. C., and R. E. Turner (1977), Updating prediction models by dynamical relaxation: an examination of the technique, Q. J. R. Meteorol. Soc., 103, 225–245, doi:10.1002/qj.49710343602.

Dee, D. P., et al. (2011), The ERA-Interim reanalysis: configuration and performance of the data assimilation system, Q. J. R. Meteorol. Soc., 137, 553–597, doi:10.1002/qj.828.

Ding, Y., and D. R. Sikka (2006), Synoptic systems and weather, in The Asian Monsoon, edited by B. Wang, pp. 131–201, Springer Praxis Books, Berlin, Heidelberg, DE, doi:10.1007/3-540-37722-0_4.

Dobler, A., and B. Ahrens (2010), Analysis of the Indian summer monsoon system in the regional climate model COSMO-CLM, J. Geophys. Res., 115, D16101, doi:10.1029/2009JD013497.

Dunning, C. M., A. G. Turner, and D. J. Brayshaw (2015), The impact of monsoon intraseasonal variability on renewable power generation in India, Environ. Res. Lett., 10(6), doi:10.1088/1748-9326/10/6/064002.

Dümenil, L., and E. Todini (1992), A rainfall-runoff scheme for use in the Hamburg climate model, in Advances in Theoretical Hydrology - A Tribute to James Dooge, edited by J. P. O'Kane, Elsevier, Amsterdam, NL.

Ebert, E. E., and J. A. Curry (1992), A Parameterization of Ice Cloud Optical Properties for Climate Models, J. Geophys. Res., 97, D4.

Foster, D. S. (1958), Thunderstorm gusts compared with computed downdraft speeds, Mon. Weather Rev., 37, 91–94.

Fouquart, Y., and B. Bonnel (1980), Computations of solar heating of the earth's atmosphere: A new parameterization, Beitr. Phys. Atmos., 53, 35–62.

Fritsch, J. M., and C. G. Chapell (1980), Numerical Prediction of Convectively Driven Mesoscale Pressure Systems. Part I: Convective Parameterization, J. Atmos. Sci., 37, 1722–1733.

Gadgil, S. (2003), The Indian Monsoon and Its Variability, Ann. Rev. Earth Planet. Sci., 31, 429–467, doi:10.1146/annurev.earth.31.100901.141251.

Gadgil, S., and G. Asha (1992), Intraseasonal Variation of the Summer Monsoon I: Observational Aspects, J. Meteorol. Soc. Japan, 70(1B), 517–527.

Gadgil, S., and K. R. Kumar (2006), The Asian monsoon - agriculture and economy, in The Asian Monsoon, edited by B. Wang, pp. 651–683, Springer Praxis Books, Berlin, Heidelberg, DE, doi:10.1007/3-540-37722-0_18.

Gill, A. E. (1980), Some simple solutions for heat-induced tropical circulation, Q. J. R. Meteorol. Soc., 106, 447–462.

Giorgetta, M. A., et al. (2013), The atmospheric general circulation model ECHAM6, Reports on Earth System Science 135, Max-Planck-Institut für Meteorologie, Hamburg, DE.

Giorgi, F., et al. (2001), Regional Climate Information - Evaluation and Projections, in Climate Change 2001: The Scientific Basis. Contribution of Working Group I to the Third Assessment Report of the Intergovernmental Panel on Climate Change, edited by J. T. Houghton, Y. Ding, D. J. Griggs, M. Noguer, P. J. van der Linden, X. Dai, K. Maskell, and C. A. Johnson, p. 881, Cambridge University Press, Cambridge, UK and New York, NY, USA.

Gollvik, S. (1999), On the effects of horizontal diffusion, resolution and orography on precipitation forecasting in a limited area model, Meteorol. Appl., 6, 49–58.

Goswami, B. N. (2012), South Asian monsoon, in Intraseasonal Variability in the Atmosphere-Ocean Climate System, edited by W. K. M. Lau and D. E. Waliser, pp. 21–72, Springer Praxis Books, Berlin, Heidelberg, DE, Second Edition.

Hagemann, S. (2002), An Improved Land Surface Parameter Dataset for Global and Regional Climate Models, Report 336, Max-Planck-Institut für Meteorologie, Hamburg, DE.

Heymsfield, A. J., and G. M. McFarquhar (2001), Microphysics of INDOEX clean and polluted trade cumulus clouds, J. Geophys. Res., 106(D22), 28,653–28,673, doi:10.1029/2000JD900776.

Holton, J. R. (Ed.) (2004), An Introduction to Dynamic Meteorology, Elsevier Academic Press, Burlington, MA, USA and San Diego, CA, USA and London, UK, Fourth Edition.

Hoskins, B., and B. Wang (2006), Large-scale atmospheric dynamics, in The Asian Monsoon, edited by B. Wang, pp. 357–415, Springer Praxis Books, Berlin, Heidelberg, DE, doi:10.1007/3-540-37722-0_9.

Huffman, G. J., D. T. Bolvin, E. J. Nelkin, D. B. Wolff, R. F. Adler, G. Gu, Y. Hong, K. P. Bowman, and E. F. Stocker (2007), The TRMM Multisatellite Precipitation Analysis (TMPA): Quasi-Global, Multiyear, Combined-Sensor Precipitation Estimates at Fine Scales, J. Hydrometeorol., 8, 38–55, doi:10.1175/JHM560.1.

Janjić, Z. I. (2000), NOTES AND CORRESPONDENCE, Comments on 'Development and Evaluation of a Convection Scheme for Use in Climate Models', J. Atmos. Sci., 57, 3686.

Jiang, X., T. Li, and B. Wang (2004), Structures and Mechanisms of the Northward Propagating Boreal Summer Intraseasonal Oscillation, J. Climate, 17, 1022–1039.

Johnson, D. W. (1993), Parametrisation of the cloud topped boundary layer: Aircraft measurements, in ECMWF Workshop Proc. 'Parametrization of the cloud topped boundary layer', pp. 77–117, European Centre for Medium-Range Weather Forecasts, Reading, UK.

Kain, J. S., and J. M. Fritsch (1993), A One-Dimensional Entraining/Detraining Plume Model and Its Application in Convective Parameterization, J. Atmos. Sci., 47, 2784–2802.

Kaufman, Y. J., D. Tanré, and O. Boucher (2002), A satellite view of aerosols in the climate system, Nature, 419, 215–223, doi:10.1038/nature01091.

Kemball-Cook, S. R., and B. C. Weare (2001), The Onset of Convection in the Madden-Julian Oscillation, J. Climate, 14, 780–793.

Kiran, V. R., M. Rajeevan, S. V. B. Rao, and N. P. Rao (2009), Analysis of variations of cloud and aerosol properties associated with active and break spells of Indian summer monsoon using MODIS data, Geophys. Res. Lett., 36, L09706, doi:10.1029/2008GL037135.

Kiranmayi, L., and E. D. Maloney (2011), Intraseasonal moist static energy budget in reanalysis data, J. Geophys. Res., 116, D21117, doi:10.1029/2011JD016031.

Klaus, D. (2014), Validierung und Verbesserung der arktischen Wolkenparametrisierung im regionalen Atmosphärenmodell HIRHAM5, Doctoral Thesis, Univ. of Potsdam, Potsdam, DE.

Koepke, P., M. Hess, I. Schult, and E. Shettle (1997), Global Aerosol Data Set, Report 243, Max-Planck-Institut für Meteorologie, Hamburg, DE.

Køltzow, M. (1992), The effect of a new snow and sea ice albedo scheme on regional climate model simulation, J. Geophys. Res., 112, D07110, doi:10.1029/2006JD007693.

Koren, I., J. V. Martins, L. A. Remer, and H. Afargan (2008), Smoke Invigoration Versus Inhibition of Clouds over the Amazon, Science, 321, 946–949, doi:10.1126/science.1159185.

Krishnamurthy, V., and J. Shukla (2007), Intraseasonal and Seasonally Persisting Patterns of Indian Monsoon Rainfall, J. Climate, 20, 3–20, doi:10.1175/JCLI3981.1.

Krishnamurti, T. N., A. Thomas, A. Simon, and V. Kumar (2010), Desert Air Incursions, an Overlooked Aspect, for the Dry Spells of the Indian Summer Monsoon, J. Atmos. Sci., 67, 3423–3441, doi:10.1175/2010JAS3440.1.

Krishnan, R., C. Zhang, and M. Sugi (2000), Dynamics of Breaks in the Indian Summer Monsoon, J. Atmos. Sci., 57, 1354–1372.

Lau, K.-M., and K.-M. Kim (2006), Observational relationships between aerosol and Asian monsoon rainfall, and circulation, Geophys. Res. Lett., 33, L21810, doi:10.1029/2006GL027546.

Lau, K.-M., M. K. Kim, and K.-M. Kim (2006), Asian summer monsoon anomalies induced by aerosol direct forcing: the role of the Tibetan Plateau, Clim. Dynam., 26, 855–864, doi:10.1007/s00382-006-0114-z.

Liu, X., X. Xie, Z.-Y. Yin, C. Liu, and A. Gettelman (2011), A modeling study of the effects of aerosols on clouds and precipitation over East Asia, Theor. Appl. Climatol., 106, 343–354, doi:10.1007/s00704-011-0436-6.

Lohmann, U., and J. Feichter (2005), Global indirect aerosol effects: a review, Atmos. Chem. Phys., 5, 715–737, doi:10.5194/acp-5-715-2005.

Lohmann, U., and E. Roeckner (1996), Design and performance of a new cloud microphysics scheme developed for the ECHAM general circulation model, Clim. Dyn., 12, 557–572.

Lucas-Picher, P., J. H. Christensen, F. Saeed, P. Kumar, S. Asharaf, B. Ahrens, A. J. Wiltshire, D. Jacob, and S. Hagemann (2011), Can Regional Climate Models Represent the Indian Monsoon?, J. Hydrometeorol., 12, 849–868, doi:10.1175/2011JHM1327.1.

Maloney, E. D. (2009), The Moist Static Energy Budget of a Composite Tropical Intraseasonal Oscillation in a Climate Model, J. Climate, 22, 711–729, doi:10.1175/2008JCLI2542.1.

Manoj, M. G., P. C. S. Devara, P. D. Sahai, and B. N. Goswami (2011), Absorbing aerosols facilitate transition of Indian mosnoon breaks to active spells, Clim. Dynam., 37, 2181–2198, doi:10.1007/s00382-010-0971-3.

Manoj, M. G., P. C. S. Devara, S. Joseph, and A. K. Sahai (2012), Aerosol indirect effect during the aberrant India Summer Monsoon breaks of 2009, Atmos. Environ., 60, 153–163.

Marbaix, P., H. Gallée, O. Brasseur, and J.-P. van Ypersele (2003), Lateral Boundary Conditions in Regional Climate Models: A Detailed Study of the Relaxation Procedure, Mon. Weather Rev., 131, 461–479.

Mauritsen, T. (2012), Tuning the climate of a global model, J. Adv. Model. Earth Syst., 4, M00A01, doi:10.1029/2012MS000154.

May, W. (2002), Simulated changes of the Indian summer monsoon under enhanced greenhouse gas conditions in a global time-slice experiment, Geophys. Res. Lett., 29(7,1118), doi:10.1029/2001GL013808.

May, W. (2003), The Indian Summer Monsoon and its Sensitivity to the Mean SSTs: Simulations with the ECHAM4 AGCM at T106 Horizontal Resolution, J. Meteorol. Soc. Japan, 81(1), 57–83.

McDonald, A. (1995), The HIRLAM two time level, three dimensional semi-Lagrangian, semi-implicit, limited area, grid point model of the primitive equations, Tech. Rep. 17, Swedish Meteorological and Hydrological Institute, Norrköping, SE.

Menon, S., J. Hansen, L. Nazarenko, and Y. Luo (2002), Climate Effects of Black Carbon Aerosols in China and India, Science, 297, 2250–2253, doi:10.1126/science.1075159.

Mlawer, E. J., S. J. Taubman, P. D. Brown, M. J. Iacono, and S. A. Clough (1997), Radiative transfer for inhomogeneous atmospheres: RRTM, a validated correlated-k model for the longwave, J. Geophys. Res., 102, D14.

Moss, S. J., P. N. Francis, and D. G. Johnson (1996), Calculation and parameterization of the effective radius of ice particles using aircraft data, Proc. 12th Int. Conf. on Clouds and Precipitation, 1255-1258, Int. Commission on Clouds and Precipitation and Int. Assoc. of Meteorology and Atmospheric Science, Zürich, CH.

Mukhopadhyay, P., S. Taraphdar, B. N. Goswami, and K. Krishnakumar (2010), Indian Summer Monsoon Precipitation Climatology in a High-Resolution Regional Climate Model: Impacts of Convective Parameterization on Systematic Biases, Weather Forecast., 25, 369–387, doi:10.1175/2009WAF2222320.1.

Nakajima, T., A. Higurashi, K. Kawamoto, and J. E. Penner (2001), A possible correlation between satellite-derived cloud and aerosol microphysical parameters, Geophys. Res. Lett., 28(7), 1171–1174.

Nigam, S., and M. Bollasina (2010), "Elevated heat pump" hypothesis for the aerosol-monsoon hydroclimate link: "Grounded" in observations?, J. Geophys. Res., 115, D16201, doi:10.1029/2009JD013800.

Nordeng, T. E. (1994), Extended versions of the convective parametrization scheme at ECMWF and their impact on the mean and transient activity of the model in the tropics, Tech. Memo. 206, European Centre for Medium-Range Weather Forecasts, Reading, UK.

Pal, J. S., and E. A. B. Eltahir (2001), Pathways Relating Soil Moisture Conditions to Future Summer Rainfall within a Model of the Land-Atmosphere System, J. Climate, 14, 1227–1242.

Parthasarathy, B., K. R. Kumar, and D. R. Kothawale (1992), Indian summer monsoon rainfall indices: 1871-1990, Meteorol. Mag., 121(1441), 174–186.

Parthasarathy, B., A. A. Munot, and D. R. Kothawale (1994), All-India Monthly and Seasonal Rainfall Series: 1871-1993, Theor. Appl. Climatol., 49(4), 217–224.

Petty, G. W. (Ed.) (2006), A First Course in Atmospheric Radiation, Sundog Publishing, Madison, WI, USA, Second Edition.

Polanski, S., A. Rinke, and K. Dethloff (2010), Validation of the HIRHAM-Simulated Indian Summer Monsoon Circulation, Adv. Meteorol., 2010, Article ID 415632, doi:10.1155/2010/415632.

Prasanna, V., and H. Annamalai (2012), Moist Dynamics of Extended Monsoon Breaks over South Asia, J. Climate, 25, 3810–3831, doi:10.1175/JCLI-D-11-00459.1.

Raghavan, K. (1973), Break-Monsoon Over India, Mon. Weather Rev., 101(1), 33–43.

Raman, C. R. V., and Y. P. Rao (1981), Blocking highs over Asia and monsoon droughts over India, Nature, 289, 271–273, doi:10.1038/289271a0.

Ramanathan, V., P. J. Crutzen, J. T. Kiehl, and D. Rosenfeld (2001), Aerosols, Climate, and the Hydrological Cycle, Science, 294(5549), 2119–2124, doi:10.1126/science.1064034.

Ramanathan, V., et al. (2005), Atmospheric brown clouds: Impacts on South Asian climate and hydrological cycle, Proc. Nat. Acad. Sci. USA, 102(15), 5326–5333, doi:10.1073/pnas.0500656102.

Ramaswamy, C. (1962), Breaks in the Indian summer monsoon as a phenomenon of interaction between the easterly and the sub-tropical westerly jet streams, Tellus, 14, 337–349.

Rao, K. G., M. Desbois, R. Roca, and K. Nakamura (2004), Upper tropospheric drying and the "transition to break" in the Indian summer monsoon during 1999, Geophys. Res. Lett., 31, L03206, doi:10.1029/2003GL018269.

Rinke, A., K. Dethloff, J. H. Christensen, M. Botzet, and B. Machenhauer (1997), Simulation and validation of Arctic radiation and clouds in a regional climate model, J. Geophys. Res., 102, D25.

Rockel, B., and B. Geyer (2008), The performance of the regional climate model CLM in different climate regions, based on the example of precipitation, Meteorol. Z., 17(4), 487–498.

Rockel, B., E. Raschke, and B. Weyres (1991), A parameterization of broad band radiative transfer properties of water, ice, and mixed phase clouds, Beitr. Phys. Atmos., 64, 1–12.

Rodwell, M. J., and B. J. Hoskins (1996), Monsoons and the dynamics of deserts, Q. J. R. Meteorol. Soc., 122, 1385–1404.

Roeckner, E., et al. (1992), Simulation of the present-day climate with the ECHAM model: Impact of model physics and resolution, Tech. Rep. 93, Max-Planck-Institut für Meteorologie, Hamburg, DE.

Roeckner, E., et al. (2003), The atmospheric general circulation model ECHAM5 - Part I, Tech. Rep. 349, Max-Planck-Institut für Meteorologie, Hamburg, DE.

Roesch, A. C. (2000), Assessment of the Land Surface Scheme in Climate Models with Focus on Surface Albedo and Snow Cover, Zürcher Klima-Schriften 78, Eidgenössische Technische Hochschule Zürich, Zürich, CH.

Rosenfeld, D. (2007), Aerosol-Cloud Interactions Control of Earth Radiation and Latent Heat Release Budgets, Space Sci. Rev., 23, 149–157, doi:10.1007/978-0-387-48341-2_12.

Rosenfeld, D., U. Lohmann, G. B. Raga, C. D. O'Dowd, M. Kulmala, S. Fuzzi, A. Reissell, and M. O. Andreae (2008), Flood or Drought: How Do Aerosols Affect Precipitation?, Science, 321(5894), 1309–1313, doi:10.1126/science.1160606.

Rummukainen, M. (2010), State-of-the-art with regional climate models, WIREs Clim. Change, 1, 83–96, doi:10.1002/wcc.8.

Saeed, F., S. Hagemann, and D. Jacob (2009), Impact of irrigation on the South Asian summer monsoon, Geophys. Res. Lett., 36, L20711, doi:10.1029/2009GL040625.

Saeed, F., S. Hagemann, and D. Jacob (2012), A framework for the evaluation of the South Asian summer monsoon in a regional climate model applied to REMO, Int. J. Climatol., 32, 430–440, doi:10.1002/joc.2285.

Sass, B. H., N. W. Nielsen, J. U. Jørgensen, B. Amstrup, M. Kmit, and K. S. Mogensen (2002), The operational DMI-HIRLAM system 2002-version, Tech. Rep. 02-05, Danish Meteorological Institute, Copenhagen, DK.

Sikka, D. R., and S. Gadgil (1980), On the Maximum Cloud Zone and the ITCZ over Indian Longitudes during the Southwest Monsoon, Mon. Weather Rev., 108(11), 1840–1853.

Singh, D., M. Tsiang, B. Rajaratnam, and N. S. Diffenbaugh (2014), Observed changes in extreme wet and dry spells during the South Asian summer monsoon season, Nature Clim. Change, 4, 456–461, doi:10.1038/nclimate2208.

Sinha, P., U. C. Mohanty, S. C. Kar, S. K. Dash, and S. Kumari (2012), Sensitivity of the GCM driven summer monsoon simulations to cumulus parameterization schemes in nested RegCM3, Theor. Appl. Climatol., 112, 285–306, doi:10.1007/s00704-012-0728-5.

Sobel, A. H., J. Nilsson, and L. M. Polvani (2001), The Weak Temperature Gradient Approximation and Balanced Tropical Moisture Waves, J. Atmos. Sci., 58, 3650–3665, doi:10.1175/1520-0469(2001)058<3650:TWTGAA>2.0.CO;2.

Srinivas, C. V., D. Hariprasad, D. V. B. Rao, Y. Anjaneyulu, R. Baskaran, and B. Venkatraman (2012), Simulation of the Indian summer monsoon regional climate using advanced WRF model, Int. J. Climatol., 33, 1195–1210, doi:10.1002/joc.3505.

Stachnik, J. P., C. Schumacher, and P. E. Ciesielski (2013), Total Heating Characteristics of the ISCCP Tropical and Subtropical Cloud Regimes, J. Climate, 26, 7097–7116, doi: 10.1175/JCLI-D-12-00673.1.

Su, H., and J. D. Neelin (2002), Teleconnection Mechanismus for Tropical Pacific Descent Anomalies during El Niño, J. Atmos. Sci., 59, 2694–2712.

Sundqvist, H., E. Berge, and J. E. Kristjánsson (1989), Condensation and Cloud Parameterization Studies with a Mesoscale Numerical Weather Prediction Model, Mon. Weather Rev., 117, 1641–1957.

Tanre, D., J.-F. Geleyn, and J. M. Slingo (1984), First results of the introduction of an advanced aerosol-radiation interaction on the ECMWF low resolution global model, in Aerosols and Their Climate Effects, edited by H. E. Gerber and A. Deepak, pp. 133–177, A. Deepak, Hampton, VA, USA.

Tiedtke, M. (1989), A Comprehensive Mass Flux Scheme for Cumulus Parameterization in Large-Scale Models, Mon. Weather Rev., 117, 1779–1800.

Tompkins, A. M. (2002), A Prognostic Parameterization for the Subgrid-Scale Variability of Water Vapor and Clouds in Large-Scale Models and Its Use to Diagnose Cloud Cover, J. Atmos. Sci., 59(12), 1917–1942.

Tompkins, A. M. (2005), The parametrization of cloud cover, Techn. Memo., Moist Processes Lecture Note Series, European Centre for Medium-Range Weather Forecasts, Reading, UK.

Trenberth, K. E., J. W. Hurrell, and D. P. Stepaniak (2006), The Asian monsoon: Gobal perspectives, in The Asian Monsoon, edited by B. Wang, pp. 67–87, Springer Praxis Books, Berlin, Heidelberg, DE, doi:10.1007/3-540-37722-0_2.

TRMM (2015), Tropical Rainfall Measuring Mission, NASA, GODDARD SPACE FLIGHT CENTER, `http://trmm.gsfc.nasa.gov/`, last accessed: 02/07/2015.

Turner, A. G., and H. Annamalai (2012), Climate change and the South Asian summer monsoon, Nature Clim. Change, 2(8), 587–595, doi:10.1038/nclimate1495.

Twomey, S. (1977), The Influence of Pollution on the Shortwave Albedo of Clouds, J. Atmos. Sci., 34, 1149–1152.

Undén, P., et al. (2002), HIRLAM-5 Scientific Documentation, HIRLAM-5 Project, Swedish Meteorological and Hydrological Institute, Norrköping, SE.

Waliser, D. E. (2006), Intraseasonal variability, in The Asian Monsoon, edited by B. Wang, pp. 203–257, Springer Praxis Books, Berlin, Heidelberg, DE, doi:10.1007/3-540-37722-0_5.

Webster, P. J. (1972), Response of the Tropical Atmosphere to Local, Steady Forcing, Mon. Weather Rev., 100(7), 518–541.

Webster, P. J. (2006), The coupled monsoon system, in The Asian Monsoon, edited by B. Wang, pp. 3–66, Springer Praxis Books, Berlin, Heidelberg, DE, doi:10.1007/3-540-37722-0_1.

Yang, S., and W. K.-M. Lau (2006), Interannual variability of the Asian monsoon, in The Asian Monsoon, edited by B. Wang, pp. 259–293, Springer Praxis Books, Berlin, Heidelberg, DE, doi:10.1007/3-540-37722-0_6.

Yasutomi, N., A. Hamada, and A. Yatagai (2011), Development of a Long-term Daily Gridded Temperature Dataset and Its Application to Rain/Snow Discrimination of Daily Precipitation, Glob. Environ. Res., 15, 165–172.

Yatagai, A., K. Kamiguchi, O. Arakawa, A. Hamada, N. Yasutomi, and A. Kitoh (2012), APHRODITE: Constructing a Long-Term Daily Gridded Precipitation Dataset for Asia Based on a Dense Network of Rain Gauges, Bull. Am. Meteorol. Soc., 93, 1401–1415, doi:10.1175/BAMS-D-11-00122.1.

Zubler, E. M. (2011), Representation of aerosol and cloud microphysics in a regional climate model - Implementation, evaluation and long-term simulations, Doctoral Thesis, ETH Zürich, Zürich, CH.

Abbreviations

AIMR	all-India monsoon rainfall
APHRODITE	Asia Precipitation - Highly Resolved Observational Data Integration Towards Evaluation
aprc	convective precipitation
aprl	large-scale precipitation
AWI	Alfred Wegener Institute Helmholtz Centre for Polar and Marine Research
CEJ	cross-equatorial jet
ciwp	cloud ice water path
CLM	Climate Local Model
clwp	cloud liquid water path
COSMO-CLM	Consortium for Small-scale Modelling - Climate Local Model
day 0	day with the maximum amplitude of total precipitation anomalies during the break phase
DJF	December-January-February
DMI	Danish Meteorological Institute
ECHAM	European Centre Hamburg Model
ECHAM4	European Centre Hamburg Model version 4, previous version of ECHAM5
ECHAM5	European Centre Hamburg Model version 5
ECHAM6	European Centre Hamburg Model version 6, current version of ECHAM
ECMWF	European Centre for Medium-Range Weather Forecasts
EJ	easterly jet
ENSO	El Niño/Southern Oscillation
ERA 40	ERA 40 reanalysis, earlier ECMWF reanalysis
ERA Interim	ERA Interim reanalysis, latest ECMWF reanalysis
evap	evaporation

GADS	Global Aerosol Data Set
GCM	global climate model
GPCP	Global Precipitation Climatology Project
HH5-CTRL	HIRHAM5 control run
HH5-CTRL-nN	HIRHAM5 control run - no nudging
HH5-FINAL	final HIRHAM5 sensitivity run with tuned conditions
HH5-POL-nN	HIRHAM5 run with polluted clouds (increased N_l) - no nudging
HH5-S	HIRHAM5 sensitivity run representing the control condition for the sensitivity runs
HH5-S1 - S7	HIRHAM5 sensitivity runs 1-7 with tuned conditions
HIRHAM4	version 4 of the atmospheric regional climate model HIRHAM, previous version of HIRHAM5
HIRHAM5	version 5 of the atmospheric regional climate model HIRHAM
HIRLAM	High Resolution Limited Area Model
HIRLAM7	release 7.0 of HIRLAM
IFS	Integrated Forecast System
IITM	Indian Institute of Tropical Meteorology
IOD	Indian Ocean dipole
ITCZ	intertropical convergence zone
JAXA	Japan Aerospace Exploration Agency
JJAS	summer monsoon season (June-July-August-September)
LFS	level of free sinking
MJO	Madden-Julian oscillation
MRI/JMA	Meteorological Research Institute of the Japan Meteorological Agency
MSE	moist static energy
mslp	mean sea level pressure
NASA	National Aeronautics and Space Administration
NCEP-NCAR	National Center for Environmental Prediction - National Center for Atmospheric Research
net rad0	sum of net shortwave and net longwave radiation at TOA
net rads	sum of net shortwave and net longwave radiation at surface

OLR	outgoing longwave radiation
PDF	probability density function
precip	total precipitation, sum of convective and large-scale precipitation
R	correlation
RCM	regional climate model
RegCM3	Regional Climate Model version 3
REMO	Max Planck Institute Regional Model
RIHN	Research Institute for Humanity and Nature
RRTM	Rapid Radiative Transfer Model
SASM	South Asian summer monsoon
SD	standard deviation
soilm	soil moisture
srad0	net shortwave radiation at TOA
srad0u	upward shortwave radiation at TOA
srads	net shortwave radiation at surface
sradsu	upward shortwave radiation at surface
SST	sea surface temperature
tclcov	total cloud cover
TCZ	tropical convergence zone
TOA	top-of-the atmosphere
trad0	net longwave radiation at TOA
trads	net longwave radiation at surface
tradsu	upward longwave radiation at surface
TRMM	Tropical Rainfall Measuring Mission
WRF	Weather Research and Forecasting
wvp	water vapour path

Variables and symbols

a	total fractional cloud cover area of the cloud ensemble in convective clouds
a_j	fractional cloud cover area of an individual member of the cloud ensemble
a_{z_d}	fractional cloud cover area of an individual member at z_d
α_bg	background albedo
α_can	canopy albedo
α_for	total forest albedo
α_grd	ground albedo
α_sea	surface albedo over ice-free water surfaces (lake/ocean)
α_sfc	grid-cell mean albedo over snow-covered land surfaces
α_sn	snow albedo
α_snc	albedo of the snow-covered part of the canopy
$ampf$	amplification factor
b	buoyancy
$\tilde{b}$	shape parameter in the soil hydrology scheme
C	fractional cloud cover in the stratiform cloud scheme
$CAPE$	convective available potential energy
c_p	specific heat of moist air at constant pressure
c_pd	specific heat of dry air at constant pressure, $c_\mathrm{pd} = 1004\,\mathrm{J\,kg^{-1}\,K^{-1}}$
c_u	net condensation in the updrafts
c_v	interception parameter in the soil hydrology scheme
D	drainage
d	parameter that determines the efficiency of the fast drainage
D_q	operator for moisture, $D_q = \mathbf{v} \cdot \boldsymbol{\nabla} - K_\mathrm{H}\nabla^2$
$D_q q$	horizontal moisture advection
D_T	operator for temperature, $D_T = \mathbf{v} \cdot \boldsymbol{\nabla} - K_\mathrm{H}\nabla^2$
$D_T T$	horizontal temperature advection

D_{u}	detrainment of air out of the updraft for an cloud ensemble in convective clouds
$\tilde{\delta}_{\mathrm{i}}$	optical depth of a cloud layer in for the ice phase
$\tilde{\delta}_{\mathrm{l}}$	optical depth of a cloud layer in for the liquid phase
D^{o}	organised detrainment
δ^{o}	fractional organised detrainment rate
D^{t}	turbulent detrainment
δ^{t}	fractional turbulent detrainment rate
E	latent heat flux
$e_{\mathrm{d}}^{\mathrm{i}}$	sublimation of cloud ice that has been detrained into the environment
$e_{\mathrm{d}}^{\mathrm{l}}$	evaporation of cloud water that has been detrained into the environment
$e_{\mathrm{P}}^{\mathrm{i}}$	sublimation of snow in the unsaturated subcloud layer
$e_{\mathrm{P}}^{\mathrm{l}}$	evaporation of rain in the unsaturated subcloud layer
E_{u}	entrainment of air into the updraft from surroundings for an cloud ensemble in convective clouds
E_{ws}	$E_{\mathrm{ws}}(< 0)$ = evaporation of soil water, $E_{\mathrm{ws}}(> 0)$ = dew deposition
E^{o}	organised entrainment
ε^{o}	fractional organised entrainment rate
E^{t}	turbulent entrainment
ε^{t}	fractional turbulent entrainment rate
$\bar{F}_{\mathrm{i}}^{\mathrm{sed}}$	ice sedimention flux in stratiform clouds
f_{for}	fractional forest area
F_{LW}	net radiative flux in the longwave spectrum
$F_{\mathrm{LW}}^{\downarrow}$	downward longwave radiative flux
$F_{\mathrm{LW}}^{\uparrow}$	upward longwave radiative flux
F_{rad}	total net flux, $F_{\mathrm{rad}} = F_{\mathrm{SW}} + F_{\mathrm{LW}}$
f_{sn}	fractional snow cover
f_{snc}	fractional snow cover of the canopy
F_{SW}	net radiative flux in the shortwave spectrum
$F_{\mathrm{SW}}^{\downarrow}$	downward shortwave radiative flux
$F_{\mathrm{SW}}^{\uparrow}$	upward shortwave radiative flux
f_{ws}	fractional saturated area of a grid cell in the soil hydrology scheme
g	acceleration due to gravity
γ	tunable parameter for calculating the mass flux at LFS

$\tilde{\gamma}$	asymmetry factor
$G(q_\mathrm{t})$	PDF of q_t in the stratiform cloud scheme
H	surface sensible heat flux
h	moist static energy
h_cws	total field capacity of the grid cell
h_ws	soil water
IWP	in-cloud ice water path
k	model level
K_6	diffusion coefficient
k_conv	tunable parameter in the convective cloud scheme
K_H	horizontal diffusion term
K_i	mass abssorption coefficient of ice crystals
K_l	mass abssorption coefficient of cloud droplets
$K(z)$	empirical function in the convective cloud scheme
L	latent heat of condensation, $L = 2.5 \times 10^6\,\mathrm{J\,kg^{-1}}$
l	cloud water content, $l = q_\mathrm{l} + q_\mathrm{i}$
LAI	leaf area index
LWP	in-cloud liquid water path
M	mass of air
m	melting of snow in the convective cloud scheme
M_d	mass-flux of the downdrafts in convective clouds
M_sn	snow melt at the surface
M_snc	excess snow melt in the canopy
M_u	cloud ensemble mass-flux of the updrafts in convective clouds
∇_h	horizontal nabla operator
ngl	number of latitudes referring to the atmospheric grid
N_l	cloud droplet number concentration in the stratiform cloud scheme
nn	spectral resolution of ECHAM5
ω	vertical wind velocity in the p-coordinate system
$\tilde{\omega}$	single scattering albedo

$\omega\partial_p h$	MSE convergence or vertical advection of MSE
$\omega\partial_p q$	moisture convergence
P	precipitation
p	air pressure
p_0	reference pressure of 1000 hPa
$P^{\mathrm{i}}_{\mathrm{conv}}$	flux of snow in convective clouds
$\hat{P}^{\mathrm{i}}_{\mathrm{conv}}$	conversion rate from cloud ice into precipitation (snow) in convective clouds
$P^{\mathrm{l}}_{\mathrm{conv}}$	flux of rain water in convective clouds
$\hat{P}^{\mathrm{l}}_{\mathrm{conv}}$	conversion rate from cloud droplets into precipitation (rain) in convective clouds
p_{sfc}	surface pressure
$P^{\mathrm{i}}_{\mathrm{strat}}$	flux of snow in stratiform clouds
$P^{\mathrm{l}}_{\mathrm{strat}}$	flux of rain water in stratiform clouds
p_{T}	reference air pressure depth of the troposphere
P_{u}	conversion of cloud water to precipitation in the updrafts
Φ	geopotential
ψ	any prognostic model variable, $\psi \in \{u, v, T, q, q_{\mathrm{l}}, q_{\mathrm{i}}, p_{\mathrm{sfc}}\}$
Q	total water input in the soil hydrology scheme
q	specific humidity
Q_{agg}	autoconversion rate from cloud ice to snow (aggregation) in stratiform clouds
Q_{aut}	autoconversion rate from cloud droplets to rain drops in stratiform clouds
Q_{c}	convective heating
Q_{d}	diabatic heating, Q_{d} consists of heating due to radiation, release of latent heat by net condensation and vertical convergence of the vertical eddy transport of sensible heat (see Eqs. 1-2 in Stachnik et al. (2013))
Q_{evr}	evaporation of rain in stratiform clouds
q_{i}	cloud ice content
q_{l}	cloud liquid water content
Q_{mls}	snow melt in stratiform clouds
Q_{q}	moisture sink
Q_{racl}	accretional growth of rain drops through cloud droplets in stratiform clouds
Q_{rad}	diabating heating rate
Q_{saci}	accretion rate of cloud ice by snow in stratiform clouds

Q_{sacl}	accretion rate of supercooled cloud droplets by snow in stratiform clouds
q_{sat}	saturation value of the total atmospheric water content
Q_{sbs}	sublimation of snow in stratiform clouds
Q_{sed}	sedimentation of cloud ice in stratiform clouds
q_{t}	total atmospheric water content, $q_{\mathrm{t}} = q + q_{\mathrm{l}} + q_{\mathrm{i}}$
R	incoming rain in the soil hydrology scheme
r	relative humidity
r_0	subgrid-scale condensation threshold of the grid-cell mean relative humidity
$\bar{r}$	grid-cell mean relative humidity
R_{d}	gas constant for dry air, $R_{\mathrm{d}} = 287.05\,\mathrm{J\,kg^{-1}\,K^{-1}}$
R_{ei}	effective radii of ice crystals
R_{el}	effective radii of cloud droplets
r_{sat}	saturation value of the grid-cell mean relative humidity
R_{sfc}	surface runoff
R_{v}	gas constant for water vapour, $R_{\mathrm{v}} = 461.51\,\mathrm{J\,kg^{-1}\,K^{-1}}$
R_{vl}	mean volume droplet radius in the stratiform cloud scheme
ρ	air density
ρ_{w}	density of water
s	dry static energy
σ_0	minimum value of σ_{z}
σ_{max}	maximum value of σ_{z}
σ_{z}	standard deviation of height in a the grid cell
SVF	sky view factor
T	temperature
t	time
τ	characteristic time in which convection acts to reduce $CAPE$ towrds zero
$\tilde{\tau}$	mass extinction coefficient
Δt	time step
Δt_{rad}	radiation time step
T_{v}	virtual temperature
u	zonal horizontal wind component

v	meridional horizontal wind component
$\mathbf{v} \cdot \boldsymbol{\nabla} q$	horizontal moisture advection (horizontal diffusion neglected)
$\mathbf{v} \cdot \boldsymbol{\nabla} T$	horizontal temperature advection (horizontal diffusion neglected)
w_{base}	vertical wind velocity at cloud base in cumulus convection in the Cartesian coordinate system
w_j	vertical velocity of an individual member of the cloud ensemble in the Cartesian coordinate system
z	vertical coordinate in the Cartesian coordiante system
Z_{B}	height of the cloud base
z_{d}	detrainment level of convective clouds

Acknowledgement

This dissertation was realised at the Alfred Wegener Institute (AWI), Helmholtz Centre for Polar and Marine Research within the German Research Foundation (DFG) Graduate School GRK1364 'Shaping Earth's Surface in a Variable Environment - Interactions between tectonics, climate and biosphere in the African-Asian monsoonal region' of the Institute of Earth and Environmental Science at the University of Potsdam. The simulations have been performed on the supercomputer 'blizzard' at the German Climate Computing Center DKRZ (Deutsches Klimarechenzentrum).

Numerous people supported me during my PhD thesis. This work would not have been possible without them. At this point I would take the opportunity to acknowledge them.

First of all, I would like to thank Prof. Dr. Klaus Dethloff, Prof. Dr. Daniela Jacob and Dr. Hariharasubramanian Annamalai for reviewing my dissertation.

I express sincere gratitude to Prof. Dr. Klaus Dethloff for his always valuable advices, the numerous fruitful discussions and his always motivating support as my academic supervisor. I would like to say thank you for placing your confidence in me and my work.
A special thank goes to Dr. Annette Rinke for her always valuable suggestions and ideas for my PhD project. Thank you for your dedicated and close collaboration and of course for your critical proofreading.
Furthermore, I would like to thank Ines Hebestadt for her help in setting up the HIRHAM5 experiments and Heiko Gericke for his assistance in solving technical problems especially during my research stay at the University of Hawai'i at Mānoa.
All my colleagues deserve many thanks for the open and pleasant working atmosphere at the AWI and in particular within the modelling group. They made sure that I enjoyed the past three years at the institute. Special thank to Wolfgang Dorn, Daniel Klaus, Moritz Mielke and Thomas Orgis for their inspiring and cheerful conservations during lunch and coffee/tea breaks. Thank you Daniel for your willingness to always help in answering questions concerning the model.

Moreover, I wish to thank all my colleagues from my Graduate School. Thanks for the good time and the comradeship during the field schools in the Kenya Rift Valley and the Higher Himalayas. Special thank to Liv Heinecke - you are always like an older sister for me! Thank you that I can ask you for advice and help any time, no matter what sort of question!
I would like to say thank you to Prof. Dr. Manfred Strecker, representative of the Graduate School, for his consent to the financial support for my three-month research stay at the International Pacific Research Center (IPRC) in the School of Ocean and Earth Science and Technology at the University of Hawai'i at Mānoa.
Dr. Christian Wolff was just as important for my work. Without his quick word of advice, it would probably never have occurred to me to go to Hawai'i at the IPRC for a research stay abroad! I need to say a big thank you to you for that and for all your motivating words and personal advices!

My gratitude also goes to Dr. H. Annamalai and other IPRC members for providing and explaining the codes to estimate the budget diagnostics and the great collaboration. My dissertation was benefiting from all the fruitful exchanges and discussions. I would like to say thank you to Dr. H. Annamalai - for your support and trust, you have shown me.

I would like to express my gratitude to all my friends for their friendship and moral support. They made sure I did not get lost on my way. I thank you, Anja, my best friend. You are always a good listener as well as the best office-partner! I can always count on you. Thank you for this!
My parents always supported me and my decisions in every possible way. I am deeply grateful to them.

I dedicate this work to my grandma. I miss you so much!